

## MODELING AND ANALYSIS OF PZT MICROPOWER GENERATOR

Except where reference is made to the work of others, the work described in this dissertation is my own or was done in collaboration with my advisory committee. This dissertation does not include proprietary, restricted or classified information.

---

Jyoti K Ajitsaria

Certificate of Approval:

---

Jeffrey C. Suhling  
Quina Professor  
Mechanical Engineering

---

Song-Yul Choe, Chair  
Associate Professor  
Mechanical Engineering

---

George Flowers  
Professor  
Mechanical Engineering

---

Dong-Joo Kim  
Associate Professor  
Materials Engineering

---

George Flowers  
Dean  
Graduate School

MODELING AND ANALYSIS OF PZT MICROPOWER GENERATOR

Jyoti K. Ajitsaria

A Dissertation

submitted to

the Graduate Faculty of

Auburn University

in Partial Fulfillment of the

Requirements for the

Degree of

Doctor of Philosophy

Auburn University, Alabama  
December 19, 2008

MODELING AND ANALYSIS OF PZT MICROPOWER GENERATOR

Jyoti K. Ajitsaria

Permission is granted to Auburn University to make copies of this dissertation at its discretion, upon the request of individuals or institutions and at their expense.  
The author reserves all publication rights.

---

Signature of Author

---

Date of Graduation

## VITA

Jyoti K Ajitsaria, son of Kalawati Ajitsaria and P. L. Ajitsaria, was born on January 1<sup>st</sup>, 1978 in Nazira, Assam, India. He graduated from DAV Public School in August 1996. He joined the Indian Institute of Technology- Bombay, Mumbai, India in August 1997 and graduated with a Bachelor of Technology in Mechanical Engineering in August 2002 and a Master of Technology in Thermal and Fluid Engineering in August 2002. He entered the doctoral program in Mechanical Engineering at Auburn University in August 2003.

## DISSERTATION ABSTRACT

### MODELING AND ANALYSIS OF PZT MICROPOWER GENERATOR

Jyoti K. Ajitsaria

Doctor of Philosophy, December 19, 2008  
(M. Tech, Indian Institute of Technology, Bombay, 2002)  
(B. Tech, Indian Institute of Technology, Bombay, 2002)

157 Typed Pages

Directed by Song-Yul Choe

The goal of this research is to theoretically and experimentally investigate behaviors of a power harvesting system that was constructed with a bimorph cantilever made of Lead Zirconate Titanate ( $\text{Pb}[\text{Zr}_x\text{Ti}_{1-x}]\text{O}_3$ ) and a tungsten proof mass. The device should be capable of generating power in an environment where vibration frequency is around 100Hz, and the vibration amplitude is greater than  $9.8\text{m/s}^2$ , and within the temperature range from  $-20^\circ\text{C}$  to  $80^\circ\text{C}$ .

The basic materials selected for the device was soft Lead Zirconium Titanate (PZT-5H) because of the accessible large strain, acceptable mechanical strength and high piezoelectric constant. The main factors considered in the research were the resonant frequency, the output power density, power conversion circuitry and the effects of temperature. Consistent with the goal, mathematical models were developed for the device and experimentally compared with the power outputs. Primarily, development of the models aimed at prediction of the power output from the

bimorph PZT cantilever structure. The device used for validation of the models were designed and fabricated by a research group in the Materials Engineering directed by Dr. Dong-Joo Kim.

Three different mathematical models were developed with a focus on power output and efficiency. The first model for the device was approached with lumped electrical components that result in an electrical equivalent circuit. The second model used the energy conservation principal in conjunction with the PZT constitutive equations to estimate the power output. The third model was derived from the principle of couple field analysis that separately models the mechanical and electrical components of the generator and then coupled together with electro-mechanical coupling based on PZT constitutive equations.

Based on the comparison of the simulation and experimental data, it was found that the coupled field model better predicts the power output and efficiency of the device as compared with the other two models. For this reason, the coupled field model was used for further analysis of effect of temperature on the power generation and efficiency of the device. Power generation experiments were then conducted to assess the accuracy of the model for prediction of the effect of temperature on power output from the device. The mathematical models developed were implemented in Matlab/Simulink and compared with experimental data to assess performance of the model. Analysis also included AC/DC power conversion using a bridge rectifier circuit, DC/DC converter and a load tester. The voltage and power results show that the results are reasonably close to the experimental data when the natural frequencies match, which is expected. The experimental results and analysis also reveals that the increase or decrease in temperature

has an effect on both the resonant frequency and the power output. The resonant frequency of the bimorph PZT cantilever and power output decreases with an increase in temperature which matches quite well with the simulation results from the coupled field model.

Style manual or journal used	<u>Sensors and Actuators A</u>
Computer software used	<u>Microsoft Office XP, Origin 7.5, Matlab 7.0.4, Ansys 11</u>



## ACKNOWLEDGEMENTS

I would like to express my sincere gratitude to Dr. Song-Yul Choe for his expert guidance, support and persistent encouragement throughout my study period. It is a privilege to work under Dr. Choe with his extensive knowledge and genuine concern for his students. I would like to emphasize that his influence on me was not only in acquiring scientific knowledge but also as a person.

I received utmost support from my committee members Dr. Jeffrey Suhling, Dr. George Flowers, and Dr. Dong-Joo Kim and thank them whole heartedly.

Special thanks to Dongna Shen, Jung-hyun Park, Jung-Gi Lee, Jennie Barber Phil Ozmun, Justin Porter, Kaysar Rahim and Jordan Roberts. I would specifically like to thank my lab mates with whom I have worked has made my time in graduate school a very enjoyable one. I would like to thank my friends Dr. Ramji Lakshmanan, Prakriti Choudhary and Dr. Rajesh Guntupalli, for their constant motivation and valuable discussions.

I would like to thank my parents and brothers for their constant emotional support and encouragement during the course of my studies. I would like to dedicate this dissertation to my parents for supporting me and being patient with me through the ups and downs of the life. Without their support and help this work would not have been possible.

## TABLE OF CONTENTS

LIST OF FIGURES .....	xiii
LIST OF TABLES .....	xvii
1 Introduction.....	1
1.1 Comparison of Energy Scavenging Technologies.....	4
1.1.1 Solar Energy.....	5
1.1.2 Vibrations.....	6
1.1.3 Acoustic Noise .....	6
1.1.4 Temperature Variations .....	6
1.1.5 Passive Human Power.....	7
1.1.6 Active Human Power .....	8
1.1.7 Summary of Power Scavenging Sources .....	8
1.1.8 Conclusions Regarding Power Scavenging Sources.....	10
1.2 Overview of Vibration-to-Electricity Conversion Research.....	10
2 Piezoelectricity.....	16
2.1 Piezoelectric Effect .....	18
2.2 Axis Nomenclature .....	21
2.3 Coupling.....	22
2.4 Poling .....	23
2.5 33-type Stacked Piezoelectric Device.....	24

2.6	31-type Piezoelectric Device .....	25
3	Modeling and Simulation.....	28
3.1	Modeling techniques.....	29
3.2	Electrical equivalent model.....	30
3.3	Conservation of energy principle.....	36
3.4	Coupled field model.....	42
3.4.1	Electrical Energy Terms .....	44
3.4.2	Electro-Mechanical Coupling.....	45
3.5	Modeling of Temperature Effect .....	48
3.5.1	Temperature effect on PZT material properties.....	48
3.5.2	Temperature effect on Impedance .....	52
3.5.3	Temperature effect on resonant frequency .....	54
3.5.4	Temperature effect on power generation .....	58
4	Experimental Setup.....	60
4.1	Setup for Room Temperature Measurements .....	60
4.2	Setup for Temperature Varying Measurements.....	62
5	Power conversion circuit design.....	65
5.1	Load requirement .....	67
5.2	Circuit Scheme.....	68
5.3	Load Tester .....	69
5.3.1	Circuit Design .....	69
6	Results and Discussion .....	71
6.1	Results for Room Temperature Measurements.....	71

6.1.1	Ansys modeling .....	73
6.1.2	Open Circuit Results .....	79
6.1.3	Resistive Load without a rectifier .....	80
6.1.4	Resistive load with a rectifier .....	83
6.1.5	Coupled-field model results .....	88
6.2	Temperature effect on Impedance .....	95
6.3	Temperature effect on resonant frequency .....	97
6.4	Results with Power Conversion Circuit.....	107
6.4.1	I-V curve at 1-g.....	107
6.4.2	I-V curve at 3-g.....	108
6.4.3	PZT with the load tester .....	112
7	Conclusion and Discussion.....	114
	References.....	118
	Nomenclature.....	125
	Appendix.....	127

## LIST OF FIGURES

Figure 1: Power density versus lifetime for batteries, solar cells, and vibration generators. [6].....	9
Figure 2: Atomic structure of PZT [48].....	18
Figure 3: Mono vs. Poly Crystals .....	19
Figure 4: Axis nomenclature.....	22
Figure 5: Poling process: (a) Before poling (b) During poling (c) After poling.....	23
Figure 6: PZT bender configuration .....	27
Figure 7: Basic piezoelectric modes .....	27
Figure 8: A two layer PZT bender mounted as cantilever beam [6].....	29
Figure 9: A schematic diagram of a PZT cantilever beam [2].....	30
Figure 10: Circuit representation of a PZT beam [8].....	30
Figure 11: Sensor structure and equivalent SDOF model .....	41
Figure 12: Lumped mechanical model for PZT generator.....	43
Figure 13: Lumped electrical model for PZT generator.....	44
Figure 14: Interaction between the electrical, mechanical and thermal processes [48]...	49
Figure 15: Influence of temperature on the dielectric constant .....	50
Figure 16: Influence of temperature on the piezoelectric strain constant, $d_{31}$ [23].....	51
Figure 17: Temperature effect on the electrical impedance of a PZT .....	54
Figure 18: Shift in natural frequency of the PZT cantilever with temperature.....	58

Figure 19: Bimorph PZT bender.....	61
Figure 20: Schematic and picture of experimental setup.....	61
Figure 21: Experimental setup for impedance measurement.....	63
Figure 22: Schematic of the experiment on temperature effects .....	64
Figure 23: Principle of power conversion.....	65
Figure 24: Circuit Diagram for the Part I.....	67
Figure 25: Load requirement .....	67
Figure 26: Load with ideal switch .....	68
Figure 27: Circuit scheme.....	68
Figure 28: Load tester circuit layout.....	69
Figure 29: Load tester .....	70
Figure 30: Power Conversion Circuit with Load Tester.....	70
Figure 31: FFT analysis of experimental results for frequency response.....	72
Figure 32: First mode of resonance from Ansys.....	74
Figure 33: Second mode of resonance from Ansys .....	75
Figure 34: Third mode of resonance from Ansys .....	76
Figure 35: Fourth mode of resonance from Ansys .....	77
Figure 36: Fifth mode of resonance from Ansys .....	78
Figure 37: Experimental results for the open circuit AC voltage and input acceleration	79
Figure 38: Comparison of amplitude of the open circuit AC voltage for three models with experimental results .....	80
Figure 39: Experimental result for the output voltage with a 4 k $\Omega$ resistive load.....	81
Figure 40: Simulation results for the output voltage with a 4k $\Omega$ resistive load .....	82

Figure 41: I-V characteristics of the PZT bender without rectifier circuit .....	83
Figure 42: DC voltage at a 400 k $\Omega$ resistive load.....	84
Figure 43: AC voltage and current, and DC voltage at a 40k $\Omega$ resistive load with a rectifier.....	85
Figure 44: I-V characteristics of the PZT bender with rectifier.....	86
Figure 45: Comparison and evaluation of AC and DC I-V characteristics .....	87
Figure 46: Comparison of experimental vs. simulation results for frequency vs. voltage output. ....	89
Figure 47: Comparison of experimental vs. simulation results for voltage vs. load resistance.....	90
Figure 48: Comparison of experimental vs. simulation I-V characteristics .....	91
Figure 49: Equivalent circuit for system with rectifier and load resistance .....	92
Figure 50: Comparison of experimental vs. simulation DC I-V characteristics.....	93
Figure 51: Equivalent circuit for system with rectifier, capacitor and load resistance....	94
Figure 52: Comparison of experimental vs. simulation DC I-V characteristics.....	95
Figure 53: Temperature effect on the electrical impedance of a PZT .....	97
Figure 54: Shift in natural frequency of the PZT cantilever with temperature.....	98
Figure 55: Time response of the PZT cantilever for different temperature.....	99
Figure 56: Shift in natural frequency of the PZT cantilever with temperature.....	100
Figure 57: Output voltage vs. load resistance for PZT cantilever at different temperatures .....	101
Figure 58: Output active power vs. load resistance for PZT cantilever at different temperatures.....	102

Figure 59: Output active power vs. load resistance for PZT cantilever at different temperatures.....	103
Figure 60: I-V curve for PZT cantilever.....	105
Figure 61: Comparison I-V curve for PZT cantilever at 10°C.....	106
Figure 62: Comparison of I-V curve for PZT cantilever at 0°C.....	107
Figure 63: I-V curve with power conversion circuit at 1-g.....	108
Figure 64: I-V curve with power conversion circuit at 3-g.....	109
Figure 65: AC input voltage.....	110
Figure 66: DC/DC input voltage (Bridge output).....	111
Figure 67: DC/DC output voltage.....	112
Figure 68: DC/DC output wave with PZT.....	113



## LIST OF TABLES

Table 1: Comparison of energy scavenging and energy storage methods.....	5
Table 2: Summary of current PZT energy harvesting devices .....	15
Table 3: The first mode of the resonance frequency for the PZT bender .....	73
Table 4: The first 5 mode of the resonance frequency for the PZT bender .....	74
Table 5: DC/DC output with PZT for different Capacitor.....	113

# 1 Introduction

The past few years have seen an increasing interest in the development of wireless sensor networks, potentially to be used for a wide variety of applications. Integration of the power harvesting device into sensor suites will be maintenance-free in comparison with the use of battery that commonly requires a periodic replacement. In addition, there are many applications where sensors are physically embedded in an environment and are not accessible for a replacement. Moreover, the physical properties to be measured in the environment vary either relatively slow or does not need to be continuously processed for a hierarchical system. Consequently, these sensor systems can be effectively operated by intermittent transmission of data gathered and the associated power consumption can be reduced. A few possible applications include: monitoring temperature, light, and the location of persons in commercial buildings to control the environment in a more energy efficient manner, sensing harmful chemical agents in high traffic areas, monitoring fatigue crack formation on aircraft, monitoring pressure in automobile tires, etc. Indeed, many experts foresee that very low power embedded electronic devices will become a ubiquitous part of our environment, performing functions in applications ranging from entertainment to factory automation [1-5].

Methods of scavenging ambient power for use by low power wireless electronic devices has been explored in an effort to make the wireless nodes and resulting wireless sensor networks indefinitely self-contained. After a broad survey of potential energy

scavenging methods, the conversion of ambient vibrations to electricity utilizing the indirect piezoelectric effect was chosen as a method for further research.

One method of power harvesting is the use of piezoelectric materials (PZT), which form transducers that are able to interchange between electrical energy and mechanical strain or force. The ability of piezoelectric materials to convert mechanical energy into electrical energy can provide a medium to transfer ambient motion (usually vibration) into electrical energy that may be stored and utilized by electronic devices such as sensors and wireless nodes. The energy density achievable with piezoelectric devices is potentially greater than that possible with electrostatic or electromagnetic devices [6]. The use of indirect piezoelectric effect to convert mechanical to electrical work in power supply devices has been investigated by many authors. Umeda, et al [7] were among the pioneers to study the PZT generator and transformation of the mechanical impact energy into electrical energy in the PZT material. Hausler and Stein [8] proposed a power supply, based on the piezoelectric polymer PVDF, that could be surgically implanted in an animal to convert mechanical work done by an animal during breathing into electrical power. Priya [9] investigated harvesting electrical power from the wind by mounting piezoelectric polymers in windmills. Kymisis et al. [10] developed a harvesting energy from ambulatory motion by placing piezoelectric patches in the heels and soles of boots. Vibrating structures such as composite piezoelectric cantilever beams have been analyzed for their potential to generate electric power from environmental vibrations by Kasyap et al. [11]. Ramsay and Clark [12] considered effects of transverse force on the PZT generator in addition to the force applied in the poling direction. Gonzalez et al [13] analyzed the prospect of the PZT based energy conversion, and suggested several issues

to raise the electrical output power of the existing prototypes to the level being theoretically obtained. Smits and Chio [14] studied the electromechanical characteristics of a heterogeneous piezoelectric bender subject to various electrical and mechanical boundary conditions based on internal energy conservation. Other authors such as Huang et al. [15] and DeVoe et al. [16] did the displacement and tip-deflection analysis along the beam and made a comparison with the experimental results. However, both proposals were limited to the actuator mode.

Hwang and Park [17] introduced a new model based on static responses of a piezoelectric bimorph beam in a piezoelectric plate element. Roundy et al. [6,18,19] presented an electrical equivalent circuit model for the PZT bender for low vibration condition (1-10  $\text{m/s}^2$ ). Other authors, Lu et al. [20], improved the electrical model by adding an electro-mechanical coupling that represents dynamic behavior of the beam vibrating under a single degree of freedom. Eggborn [21] developed the analytical models to predict the power harvesting from a cantilever beam and a plate using Bernoulli-beam theory and made a comparison with the experimental result. Kim [22] analyzed the unimorph and bimorph diaphragm structure for the power generation using energy generation and piezoelectric constitutive equations. However, this study was limited to only diaphragm structures that were optimized through numerical analysis and FEM simulation at higher acceleration conditions. Shen et al. [23] investigated the parameters influencing the output energy of a piezoelectric bimorph cantilever beam with a proof mass, where the resonant frequency and robustness of a cantilever structure were considered for enhancing power conversion efficiency and implementing devices at high acceleration conditions.

Very recently a group of researchers has published material on optimal power circuitry design for piezoelectric generators [24, 25]. The focus of this research has been on the optimal design of the power conditioning electronics for a piezoelectric generator driven by vibrations. No effort is made to optimize the design of the piezoelectric generator itself or to design for a particular vibrations source.

Vibration-to-electricity conversion offers the potential for wireless sensor nodes to be self-sustaining in many environments. Vibrations occur in many environments including: large commercial buildings, automobiles, aircraft, ships, trains, and industrial environments. Given the wide range of potential applications for vibration based power generation, and given the fact that vibration-to-electricity converters have been investigated very little, the thorough investigation and development of such converters are merited. Many issues such as parametric study of the device design and the effect of change in temperature on the power generation characteristics of the bimorph piezoelectric power has not been addressed. Also, the implementation of rectifier circuit, DC/DC converter with resistive and capacitive loads is also missing.

## 1.1 Comparison of Energy Scavenging Technologies

A broad survey of potential energy scavenging methods has been undertaken by the author. The results of this survey are shown in Table 1. The table also includes batteries and other energy storage technologies for comparison. The table contains pure power scavenging sources and thus the amount of power available is not a function of the lifetime of the device. The values in the table are derived from a combination of published studies, experiments performed by the author, theory, and information that is commonly available in data sheets and textbooks. The source of information for each

technique is given in the third column. While this comparison is by no means exhaustive, it does provide a broad cross section of potential methods to scavenge energy and energy storage systems. Other potential sources were also considered but deemed to be outside of the application space under consideration or to be unacceptable for some other reason. A brief explanation and evaluation of each source listed in Table 1 follows.

Table 1: Comparison of energy scavenging and energy storage methods.

<b>Power Sources</b>	<b>Power density</b>	<b>Source of information</b>
Solar (solar panel)	19 to 56 W/m <sup>2</sup>	Commonly available
Vibrations	200 $\mu$ W/cm <sup>3</sup>	Roundy [6]
Temperature gradient	315 $\mu$ W/cm <sup>3</sup> from 5°C	Thermolife
Batteries (non rechargeable)	45 $\mu$ W/cm <sup>3</sup>	Commonly available
Batteries (rechargeable)	7 $\mu$ W/cm <sup>3</sup>	Commonly available

### 1.1.1 Solar Energy

Solar energy is abundant outdoors during the daytime. In direct sunlight, the power solar radiation density on the surface of earth is roughly 100 mW/cm<sup>3</sup>. Silicon solar cells are a mature technology with efficiencies of single crystal silicon cells ranging from 12% to 25%. Thin film polycrystalline, and amorphous silicon solar cells are also commercially available and cost less than single crystal silicon, but also have lower efficiency. If the target application is outdoors and needs to operate primarily during the daytime, solar cells offer an excellent and technologically mature solution but for indoor applications for all throughout the day, solar panel does not offer good solution. Available solar power indoors, however, is drastically lower than that available outdoors.

### **1.1.2 Vibrations**

A combination of theory and experiment shows that about  $200 \mu\text{W}/\text{cm}^3$  could be generated from vibrations that might be found in certain building environments. Vibrations were measured on many surfaces inside buildings, and the resulting spectra used to calculate the amount of power that could be generated. A more detailed explanation of this process will be granted in the following chapters. However, without discussing the details at this point, it does appear that conversion of vibrations to electricity can be sufficient for the target application in certain indoor environments. Some research has been done on scavenging power from vibrations; however, it tends to be very focused on a single application or technology. Therefore, a broader look at the issue is warranted [26-30].

### **1.1.3 Acoustic Noise**

There is far too little power available from acoustic noise to be of use in the scenario being investigated, except for very rare environments with extremely high noise levels. This source has been included in the table however because it often comes up in discussions.

### **1.1.4 Temperature Variations**

Naturally occurring temperature variations can also provide a means by which energy can be scavenged from the environment. Thermolife have demonstrated a thermoelectric micro-device capable of converting  $350 \mu\text{W}/\text{cm}^3$  from a  $5 \text{ }^\circ\text{C}$  temperature gradient. While this is promising and, with the improvement of thermoelectrics, could eventually result in more than  $350 \mu\text{W}/\text{cm}^3$ , situations in which there is a static  $5 \text{ }^\circ\text{C}$

temperature difference within 1 cm<sup>3</sup> are very rare. Alternatively, the natural temperature variation over a 24 hour period might be used to generate electricity. It can be shown with fairly simple calculations, assuming an average variation of 7 °C, that an enclosed volume containing an ideal gas could generate an average of 10 μW/cm<sup>3</sup>. This, however, assumes no losses in the conversion of the power to electricity. In fact some commercially available clocks, such as the Atmos clock, operate on a similar principle. The Atmos clock includes a sealed volume of fluid that undergoes a phase change right around 21 °C. As the liquid turns to gas during a normal day's temperature variation, the pressure increases actuating a spring that winds the clock. While this is very interesting, the level of power output is still substantially lower than other possible methods.

### **1.1.5 Passive Human Power**

A significant amount of work has been done on the possibility of scavenging power off the human body for use by wearable electronic devices [32-33]. The conclusion of studies undertaken at MIT suggests that the most energy rich and most easily exploitable source occurs at the foot during heel strike and in the bending of the ball of the foot. This research has led to the development of the piezoelectric shoe inserts referred to in the table. The power density available from the shoe inserts meets the constraints of the current project. However, wearable computing and communication devices are not the focus of this project. Furthermore, the problem of how to get the energy from a person's foot to other places on the body has not been satisfactorily solved. For an RFID tag or other wireless device worn on the shoe, the piezoelectric shoe inserts offer a good solution. However, the application space for such devices is extremely limited, and as mentioned, not very applicable to wireless sensor networks.



### **1.1.6 Active Human Power**

The type of human powered systems investigated at MIT could be referred to as passive human powered systems in that the power is scavenged during common activities rather than requiring the user to perform a specific activity to generate power. Human powered systems of this second type, which require the user to perform a specific power generating motion, are common and may be referred to separately as active human powered systems. Examples include standard flashlights that are powered by squeezing a lever and the Freeplay wind-up radios [34]. Active human powered devices, however, are not very applicable for wireless sensor applications.

### **1.1.7 Summary of Power Scavenging Sources**

Based on this survey, it was decided that solar energy and vibrations offered the most attractive energy scavenging solutions. Both solutions meet the power density requirement in environments that are of interest for wireless sensor networks. The question that must then be asked is: is it preferable to use a high energy density battery that would last the lifetime of the device, or to implement an energy scavenging solution? Figure 1 shows average power available from various battery chemistries (both rechargeable and non-rechargeable) versus lifetime of the device being powered.

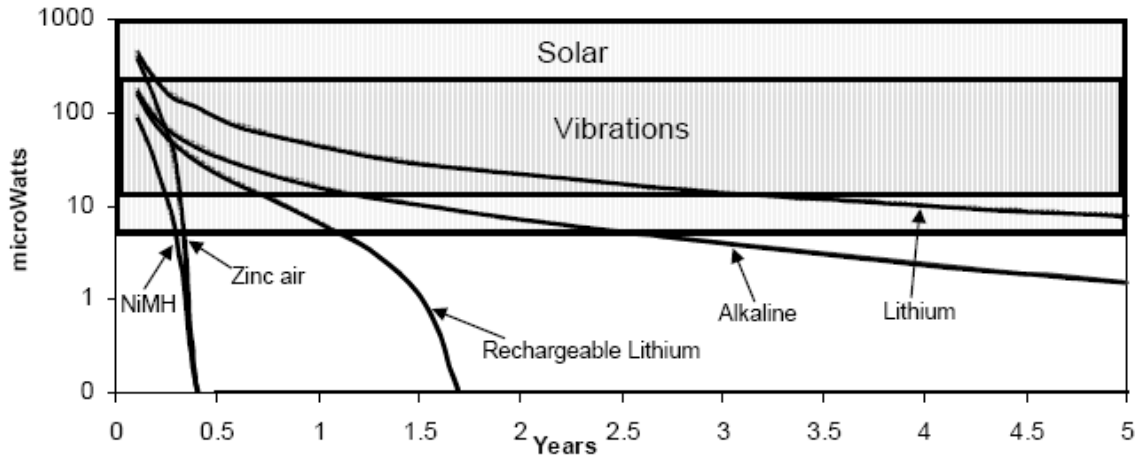


Figure 1: Power density versus lifetime for batteries, solar cells, and vibration generators.

[6]

The shaded boxes in the figure indicate the range of solar (lightly shaded) and vibration (darkly shaded) power available. Solar and vibration power output are not a function of lifetime. The reason that both solar and vibrations are shown as a box in the graph is that different environmental conditions will result in different power levels. The bottom of the box for solar power indicates the amount of power per square centimeter available in normal office lighting. The top of this box roughly indicates the power available outdoors. Likewise, the area covered by the box for vibrations covers the range of vibration sources under consideration in this study. Some of the battery traces, lithium rechargeable and zinc-air for example, exhibit an inflection point. The reason is that both battery drain and leakage are considered. For longer lifetimes, leakage becomes more dominant for some battery chemistries. The location of the inflection roughly indicates when leakage is becoming the dominant factor in reducing the amount of energy stored in the battery.

The graph indicates that if the desired lifetime of the device is in the range of 1 year or less, battery technology can provide enough energy for the wireless sensor nodes under consideration (100  $\mu$ W average power dissipation). However, if longer lifetimes are needed, as will usually be the case, then other options should be pursued. Also, it seems that for lifetimes of 5 years or more, a battery cannot provide the same level of power that solar cells or vibrations can provide even under poor circumstances. Therefore, battery technology will not meet the constraints of the project, and will not likely meet the constraints of very many wireless sensor node applications.

### **1.1.8 Conclusions Regarding Power Scavenging Sources**

Both solar power and vibration based energy scavenging look promising as methods to scavenge power from the environment. In many cases, perhaps most cases, they are not overlapping solutions because if solar energy is present, it is likely that vibrations are not, and vice versa. Solar cells are a mature technology, and one that has been profitably implemented many times in the past. So, the main focus of the research and development effort has been vibration based power generators. It was, therefore, decided to pursue vibration based solutions for the sensor nodes under development.

## **1.2 Overview of Vibration-to-Electricity Conversion Research**

Vibration-to-electricity conversion offers the potential for wireless sensor nodes to be self-sustaining in many environments. Low level vibrations occur in many environments including: large commercial buildings, automobiles, aircraft, ships, trains, and industrial environments. Given the wide range of potential applications for vibration based power generation, and given the fact that vibration-to-electricity converters have

been investigated very little, the thorough investigation and development of such converters are merited.

A few groups have previously devoted research effort toward the development of vibration-to-electricity converters. Yates, Williams, and Shearwood [26-29] have modeled and developed an electromagnetic micro-generator. The generator has a footprint of roughly 4mm X 4mm and generated a maximum of 0.3  $\mu\text{W}$  from a vibration source of displacement magnitude 500 nm at 4.4 kHz. Their chief contribution, in addition to the development of the electromagnetic generator, was the development of a generic second order linear model for power conversion. It turns out that this model fits electromagnetic conversion very well, and they showed close agreement between the model and experimental results. The electromagnetic generator was only 1mm thick, and thus the power density of the system was about 10 - 15  $\mu\text{W}/\text{cm}^3$ . Interestingly, the authors do not report the output voltage and current of their device, but only the output power. This author's calculations show that the output voltage of the 0.3  $\mu\text{W}$  generator would have been 8 mV which presents a serious problem. Because the power source is an AC power source, in order to be of use by electronics it must first be rectified. In order to rectify an AC voltage source, the voltage must be larger than the forward drop of a diode, which is about 0.5 volts. So, in order to be of use, this power source would need a large linear transformer to convert the AC voltage up by at least a factor of 100 and preferably a factor of 500 to 1000, which is clearly impractical. A second issue is that the vibrations used to drive the device are of magnitude 500 nm, or 380  $\text{m}/\text{s}^2$ , at 4.4 kHz. It is exceedingly difficult to find vibrations of this magnitude and frequency in many environments. These vibrations are far more energy rich than those measured in common

building environments, which will be discussed at length in Chapter 2. Finally, there was no attempt in that research at either a qualitative or quantitative comparison of different methods of converting vibrations to electricity. Nevertheless the work of Yates, Williams, and Shearwood is significant in that it represents the first effort to develop micro or meso scale devices that convert vibrations to electricity (meso scale here refers to objects between the macro scale and micro scale, typically objects from a centimeter down to a few millimeters).

A second group has more recently developed an electromagnetic converter and an electrostatic converter. Several publications detail their work Amirtharajah 1999, Amirtharajah & Chandrakasan 1998, Meninger et al 1999, Amirtharajah et al 2000, Meninger et al 2001 [30-34]. The electromagnetic converter was quite large and designed for vibrations generated by a person walking. (i.e. the person would carry the object in his/her pocket or somewhere else on the body). The device was therefore designed for a vibration magnitude of about 2 cm at about 2 Hz. (Note that these are not steady state vibrations.) Their simulations showed a maximum of 400  $\mu\text{W}$  from this source under idealized circumstances (no mechanical damping or losses). While they report the measured output voltage for the device, they do not report the output power. The maximum measured output voltage was reported as 180 mV, necessitating a 10 to 1 transformer in order to rectify the voltage. The device size was 4cm X 4cm X 10cm, and if it is assumed that 400  $\mu\text{W}$  of power really could be generated, then the power density of the device driven by a human walking would be 2.5  $\mu\text{W}/\text{cm}^3$ . Incidentally, they estimated the same power generation from a steady state vibration source driven by machine components (rotating machinery). The electrostatic converter designed by this

same group was designed for a MEMS process using a Silicon on Insulator (SOI). The generator is a standard MEMS comb drive (Tang, Nguyen and Howe, 1989) except that it is used as a generator instead of an actuator. There seems to have been little effort to explore other design topologies. At least, to this author's knowledge, Chandrakasan and colleagues [30-34] have not been published such an effort. Secondly, there seems to be little recognition of the mechanical dynamics of the system in the design. The authors assume that the generator device will undergo a predetermined level of displacement, but do not show that this level of displacement is possible given a reasonably input vibration source and the dynamics of the system. In fact, this author's own calculations show that for a reasonable input vibration, and the mass of their system, the level of displacement assumed is not practical. Published simulation results for their system predict a power output of  $8.6 \mu\text{W}$  for a device that is  $1.5 \text{ cm} \times 0.5 \text{ cm} \times 1 \text{ mm}$  from a vibration source at  $2.52 \text{ kHz}$  (amplitude not specified). However, no actual test results have been published to date.

Amirtharajah et al [30-34] of researchers has also developed power electronics especially suited for electrostatic vibration to electricity converters for extremely low power systems. Additionally, they have developed a low power DSP (Digital Signal Processor) for sensor applications. These are both very significant achievements and contributions. In fact, perhaps it should be pointed out that this group is comprised primarily of circuit designers, and the bulk of the material published about their project reports on the circuit design and implementation, not on the design and implementation of the power converter itself. The research presented in this thesis makes no effort to

improve upon or expand their research in this area. Rather the goal of this work is to explore the design and implementation of the power converter mechanism in great detail. Very recently a group of researchers has published material on optimal power circuitry design for piezoelectric generators (Ottman et al 2003, Ottman et al 2002). The focus of this research has been on the optimal design of the power conditioning electronics for a piezoelectric generator driven by vibrations. No effort is made to optimize the design of the piezoelectric generator itself or to design for a particular vibrations source. The maximum power output reported is 18 mW. The footprint area of the piezoelectric converter is 19 cm<sup>2</sup>. The height of the device is not given. Assuming a height of about 5 mm give a power density of 1.86 mW/cm<sup>3</sup>. The frequency of the driving vibrations is reported as 53.8 Hz, but the magnitude is not reported. The significant contribution of the research is a clear understanding of the issues surrounding the design of the power circuitry specifically optimized for a piezoelectric vibration to electricity converter. Again, the research presented in this dissertation makes no effort to improve on the power electronics design of Ottman et al, but rather to explore the design and implementation of the power converter itself.

Table 2: Summary of current PZT energy harvesting devices

Author	Device	Characteristics		Modeling
		Power	Frequency and acceleration	
Williams and Yates [26] Shearwood and Yates [27] Williams et. al [28-29]	Electromagnetic micro-generator	10-15 $\mu\text{watt}/\text{cm}^3$	4.4 KHz, 380 $\text{m}/\text{s}^2$	Generic 2 <sup>nd</sup> order linear model
Amirtharajah 1999 [30], Amirtharajah & Chandrakasan 1998 [31], Meninger et al 1999 [32], Amirtharajah et al 2000 [33], Meninger et al 2001[34]	Electromagnetic converter	2.5 $\mu\text{W}/\text{cm}^3$	2 Hz	N/A
Kasyap et. al [11]	PZT patch	N/R	N/R	Lumped element modeling
Priya [35]	PZT windmill	7.5 mW	65 Hz	Beam theory
Roundy et. Al [6,18-19]	PZT cantilever	70 $\mu\text{watt}/\text{cm}^3$	120 Hz, 2.5 $\text{m}/\text{s}^2$	Electrical equivalent model
White et. al [36] Jones et. al. [37-38]	PZT cantilever	2 $\mu\text{watt}$	80.1 Hz,	FEA model
Umeda et. al [7]	PZT plate	N/R	N/A	Electrical equivalent model
Tanaka et. al [39]	PZT cantilever	180 $\mu\text{watt}$	50 Hz, 10 $\mu\text{m}$	N/A
Mohammadi et. al [40]	PZT plate	120 mW	N/R	N/A
Ayers et. al [41]	PZT plate	N/R	1 KN, 4Hz	Equivalent circuit model
Platt et. al [42]	PZT stack	1.1 mW	440 N, < 20 Hz	Equivalent circuit model
Li et. al. [43-44]	MEMS electromagnetic	40 $\mu\text{watt}$	20 Hz, 200 $\mu\text{m}$	N/R
Ferrari et. al. [45]	PZT cantilever	0.25 $\mu\text{watt}$	41 Hz, 9 $\text{m}/\text{s}^2$	N/A
Shu et. al. [46-47]	PZT cantilever	N/R	N/R	Conversion efficiency



## 2 Piezoelectricity

In 1880 Pierre and Jacques Curie, during their experimental work on crystallography, showed that some crystalline materials, such as Rochelle salt, generate electric charges when subjected to mechanical stresses, known as the direct piezoelectric effect. The inverse effect, i.e., that an applied electric field induces a mechanical deformation, was mathematically predicted by Lippman in 1881 from basic thermodynamic principles and successively verified experimentally by Curie brothers.

Piezoelectricity is a result of the material properties at the microscopic level. Piezoelectric ceramics are crystalline materials whose basic cell, below a given temperature (Curie temperature), has an asymmetric distribution of charge giving a permanent polarization. A macroscopic block of crystalline material is made up of an assembly of grains and domains. Each domain has a direction prevalent polarization. However, in normal conditions, the domains are randomly oriented and the overall polarization of the block is statistically null. If a strong electric field (2000V/m) is applied for a sufficiently long time, the domains tend to statistically orient in the direction of the electric field and a net polarization is induced. The polarization remains when the polarizing field is removed. The obtained material block is polarized piezoelectric ceramic. The coupling between deformation and electric field is due to the geometric effects related to domain reorientation caused by an applied electric field.

The piezoelectric effect is a property that exists in many materials. The name is made up of two parts; piezo, which is derived from the Greek word for pressure, and electric from electricity. The rough translation is, therefore, pressure - electric effect. In a piezoelectric material, the application of a force or stress results in the development of a charge in the material. This is known as the direct piezoelectric effect. Conversely, the application of a charge to the same material will result in a change in mechanical dimensions or strain. This is known as the indirect piezoelectric effect. Several ceramic materials have been described as exhibiting a piezoelectric effect. These include lead-zirconate-titanate (PZT), lead-titanate ( $\text{PbTiO}_2$ ), lead-zirconate ( $\text{PbZrO}_3$ ), and barium-titanate ( $\text{BaTiO}_3$ ). These ceramics are not actually piezoelectric but rather exhibit a polarized electrostrictive effect. A material must be formed as a single crystal to be truly piezoelectric. Ceramic is a multi crystalline structure made up of large numbers of randomly orientated crystal grains. The random orientation of the grains results in a net cancelation of the effect. The ceramic must be polarized to align a majority of the individual grain effects. The term piezoelectric has become interchangeable with polarized electrostrictive effect in most literature.

Piezoelectric materials have been widely used for energy conversion device, for instance, single crystal quartz, ceramic PZT, screen printed thick PZT film, chemical solution deposited (CSD) or sol-gel derived PZT, non-ferroelectric ZnO and AlN thick or thin films, polymer PVDF (Polyvinylidene Difluoride), etc., nevertheless the majority of piezoelectric thin films is PZT because of the high piezoelectric constant and coupling coefficient at the morphotropic phase boundary (MPB). The atomic structure of PZT is shown in Figure 2. Commercially, ceramic PZT is usually not used in its pure form, but

doped acceptor or donor atoms to create vacancies and facilitate domain wall motion. Acceptor doping generates hard PZT such as PZT-5A, while donor doping generates soft PZT such as PZT-5H. In general, hard PZT domain wall is pinned by impurities thereby decreasing the losses, but at the expense of piezoelectric constant reduction. Soft PZT has higher piezoelectric constant, but larger losses due to internal friction.

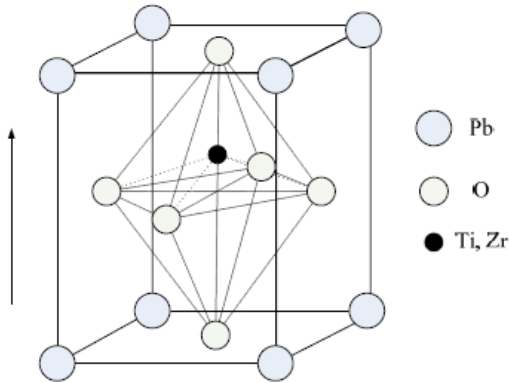


Figure 2: Atomic structure of PZT [48]

## 2.1 Piezoelectric Effect

A piezoelectric substance is one that produces an electric charge when a mechanical stress is applied (the substance is squeezed or stretched). Conversely, a mechanical deformation (the substance shrinks or expands) is produced when an electric field is applied. This effect is formed in crystals that have no center of symmetry. To explain this, we have to look at the individual molecules that make up the crystal. Each molecule has a polarization, one end is more negatively charged and the other end is positively charged, and is called a dipole. This is a result of the atoms that make up the molecule and the way the molecules are shaped. The polar axis is an imaginary line that runs through the center of both charges on the molecule. In a monocrystal the polar axes

of all of the dipoles lie in one direction. The crystal is said to be symmetrical because if you were to cut the crystal at any point, the resultant polar axes of the two pieces would lie in the same direction as the original. In a polycrystal, there are different regions within the material that have a different polar axis. It is asymmetrical because there is no point at which the crystal could be cut that would leave the two remaining pieces with the same resultant polar axis illustrates this concept. The difference between the monocrystal and polycrystal structure is illustrated in Figure 3.

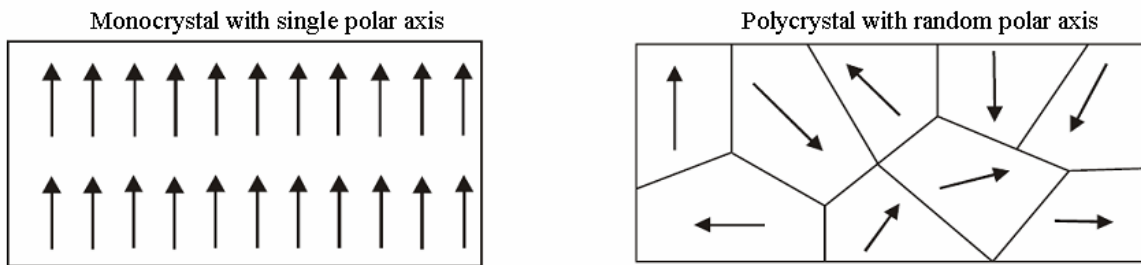


Figure 3: Mono vs. Poly Crystals

It is best to start with an understanding of common dielectric materials in order to understand the piezoelectric effect. The defining equations for high permittivity dielectrics are:

$$C = \frac{K\epsilon_r A}{t} = \frac{\epsilon_o \epsilon_r A}{t} = \frac{\epsilon A}{t} \quad (1)$$

And

$$Q = CV = \frac{\epsilon AV}{t} \quad (2)$$

Where,

C = capacitance

A = capacitor plate area

$\epsilon_r$  = relative dielectric constant

$\epsilon_0$  = dielectric constant of air =  $8.85 \times 10^{-12}$  faradays / meter

$\epsilon$  = dielectric constant

V = voltage

t = thickness or plate separation

Q = charge

In addition, we can define electric displacement, D, as charge density or the ratio of charge to the area of the capacitor:

$$D = \frac{Q}{A} = \frac{\epsilon V}{t} \quad (3)$$

and further define the electric field as:

$$H = \frac{V}{t} \quad \text{or} \quad D = \epsilon H \quad (4)$$

These equations are true for all isotropic dielectrics. Piezoelectric ceramic materials are isotropic in the unpolarized state, but they become anisotropic in the poled state. In anisotropic materials, both the electric field and electric displacement must be represented as vectors with three dimensions in a fashion similar to the mechanical force vector. This is a direct result of the dependency of the ratio of dielectric displacement, D, to electric field, H, upon the orientation of the capacitor plate to the crystal (or poled ceramic) axes. This means that the general equation for electric displacement can be written as a state variable equation:

$$D_i = \varepsilon_{ij} E_j \quad (5)$$

The electric displacement is always parallel to the electric field, thus each electric displacement vector,  $D_i$ , is equal to the sum of the field vector,  $E_j$ , multiplied by its corresponding dielectric constant,  $\varepsilon_{ij}$ :

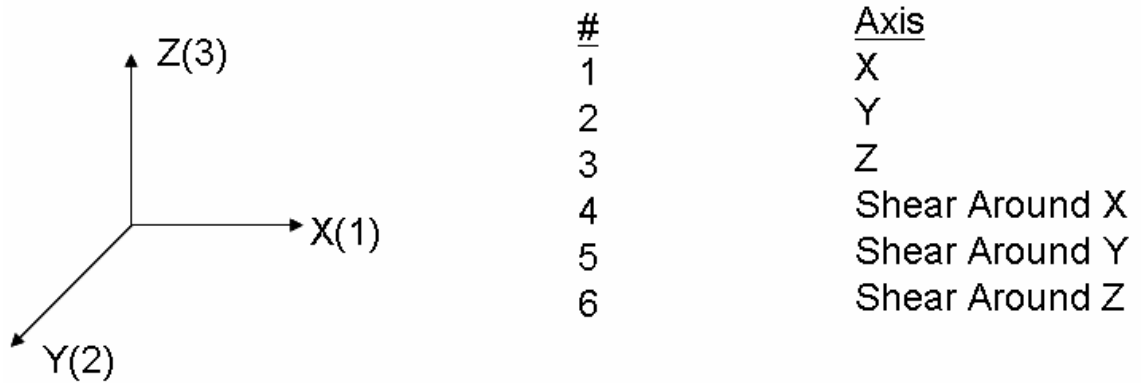
$$\begin{aligned} D_1 &= \varepsilon_{11} E_1 + \varepsilon_{12} E_2 + \varepsilon_{13} E_3 \\ D_2 &= \varepsilon_{21} E_1 + \varepsilon_{22} E_2 + \varepsilon_{23} E_3 \\ D_3 &= \varepsilon_{31} E_1 + \varepsilon_{32} E_2 + \varepsilon_{33} E_3 \end{aligned} \quad (6)$$

Fortunately, the majority of the dielectric constants for piezoelectric ceramics (as opposed to single crystal piezoelectric materials) are zero. The only non-zero terms are:

$$\varepsilon_{11} = \varepsilon_{22}, \varepsilon_{33}$$

## 2.2 Axis Nomenclature

The piezoelectric effect, as stated previously, relates mechanical effects to electrical effects. These effects, as shown above, are highly dependent upon their orientation to the poled axis. It is, therefore, essential to maintain a constant axis numbering scheme. The axis nomenclature followed is shown in Figure 4.



For electromechanical constants:  
 $d_{ab}$ , a = electrical direction; b = mechanical direction

Figure 4: Axis nomenclature

### 2.3 Coupling

Coupling is a key constant used to evaluate the "quality" of an electro-mechanical material. This constant represents the efficiency of energy conversion from electrical to mechanical or mechanical to electrical.

$$K_2 = \frac{\text{Mechanical Energy Converted to Electrical Charge}}{\text{Mechanical Energy Input}} \quad (7)$$

Or

$$K_2 = \frac{\text{Electrical Energy Converted Mechanical Displacement}}{\text{Electrical Energy Input}} \quad (8)$$

In this chapter, the review of different forms of piezoelectric generators configuration is done. They are presented here to provide a working foundation for the mathematical modeling in the next chapter highlighting important features that distinguish each design. While there are many piezoelectric materials from which to

choose for a piezoelectric generator, we plan on using lead zirconate titanate (PZT). So from this point onwards, the word PZT and piezoelectric may be used interchangeably, although, it is understood that except when referring to specific PZT material constants, other piezoelectric materials could be assumed to be used.

## 2.4 Poling

Piezoelectric material, which is non-conductive in nature, does not have free electrons, and therefore electrons cannot pass freely through the material. Piezoelectric material is made up of crystals that have many “fixed” electrons. These fixed electrons can move slightly as the crystals deform by an external force. This slight movement of electrons alters the equilibrium status in the adjacent conductive materials and creates electric force. This force will push and pull the electrons in the electrodes attached to the piezoelectric crystal as shown in the Figure 5.

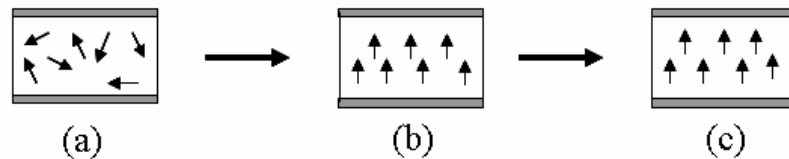


Figure 5: Poling process: (a) Before poling (b) During poling (c) After poling

Piezoelectric ceramic materials, as stated earlier, are not piezoelectric until the random ferroelectric domains are aligned. This alignment is accomplished through a process known as "poling". Poling consists of inducing a D.C. voltage across the material. The ferroelectric domains align to the induced field resulting in a net piezoelectric effect. It should be noted that not all the domains become exactly aligned. Some of the domains only partially align and some do not align at all. The number of domains that align depends upon the poling voltage, temperature, and the time the voltage is held on the



material. During poling the material permanently increases in dimension between the poling electrodes and decreases in dimensions parallel to the electrodes. The material can be depolarized by reversing the poling voltage, increasing the temperature beyond the materials Currie point, or by inducing a large mechanical stress.

Voltage applied to the electrodes at the same polarity as the original poling voltage results in a further increase in dimension between the electrodes and decreases the dimensions parallel to the electrodes. Applying a voltage to the electrodes in an opposite direction decreases the dimension between the electrodes and increases the dimensions parallel to the electrodes.

Applying a compressive force in the direction of poling (perpendicular to the poling electrodes) or a tensile force parallel to the poling direction results in a voltage generation on the electrodes which has the same polarity as the original poling voltage. A tensile force applied perpendicular to the electrodes or a compressive force applied parallel to the electrodes results in a voltage of opposite polarity.

Removing the poling electrodes and applying a field perpendicular to the poling direction on a new set of electrodes will result in mechanical shear. Physically shearing the ceramic will produce a voltage on the new electrodes.

## 2.5 33-type Stacked Piezoelectric Device

Generally piezoelectric devices cannot create large deformations. It is almost impossible to detect the deformation with naked eye. The small micro-scale deformation with very high electric field requirement and the material's brittle characteristics prevent popular use of the device material for strain generation. To overcome this disadvantage of piezoelectric devices, stacked piezoelectric device was introduced. The stacked device

can produce same strain with a low electric field. A piezoelectric stack actuator is made of large number of these piezoelectric plates that are glued together and wired in parallel. The device actuation direction is in the 33-direction (force and poling directions are same). So a better performance can be obtained from the actuator depending on the number of the piezoelectric layers. For this reason, piezoelectric stack actuator is the most common force-generating device. The disadvantages of the stacked piezoelectric devices are 1) lateral force must be avoided and 2) relatively large volume.

For the piezoelectric stack as a power generator, the stacked piezoelectric can convert only longitudinal direction compressive force to electric energy as shown in figure. A stack piezoelectric generator can generate charge only when pressed along the longitudinal direction. If a compressive prestress is applied to the stack to prevent fracture in both piezoelectric and glued layer, then the applied force can be either tensile or compressive. A stack piezoelectric cannot generate electric energy with bending lateral force. In addition, small sized stacked devices are hard to fabricate. For the power generation purpose, magneto-electric generators perform better than same sized stack piezoelectric generator.

## 2.6 31-type Piezoelectric Device

Another common piezoelectric actuator/generator is the cantilever beam. Cantilever benders can generate significant deflection compared to the longitudinal direction cantilever actuator, and can be found in many applications such as microvalves etc. For the energy harvesting purpose, cantilever benders can be good generators because it is easier to convert force into higher strain as compared to the 33-type stack configuration. Multilayer cantilever beams are common mechanical bending elements and are widely

used. The mechanism of cantilever bender is simple. One layer is generally in tension and the other layer is in compression. They are usually called unimorph or bimorph cantilever depending on the number of layers in the bender element. Bimorph cantilever piezoelectric generator contains two piezoelectric layer bonded to a non-piezoelectric material in the middle and unimorph cantilever contains one piezoelectric layer and one non-piezoelectric layer. One example of a unimorph cantilever is a thermostat. Thermostats are made of two materials with different thermal expansion coefficients. Since one side of the cantilever is more sensitive to temperature change, a unimorph cantilever will bend when temperature changes. In other words, one side expands or contracts more with temperature changes. In the piezoelectric unimorph cantilever beam, the piezoelectric layer expands or contracts. When the unimorph cantilever beam undergoes bending, electric fields are generated between the electrodes of the piezoelectric layer.

Piezoelectric benders are often used to create actuators with large displacement capabilities. The bender works in a mode which is very similar to the action of a bimetallic spring. Two separate bars or wafers of piezoelectric material are metallized and poled in the thickness expansion mode. They are then assembled in a + -+ - stack and mechanically bonded. In some cases, a thin membrane is placed between the two wafers. The outer electrodes are connected together and a field is applied between the inner and outer electrodes. The result is that for one wafer the field is in the same direction as the poling voltage while the other is opposite to the poling direction, this means that one wafer is increasing in thickness and decreasing in length while the other wafer is

decreasing in thickness and increasing in length, resulting in a bending moment. The PZT bender configuration and the PZT bending modes are shown in Figure 6 and Figure 7.

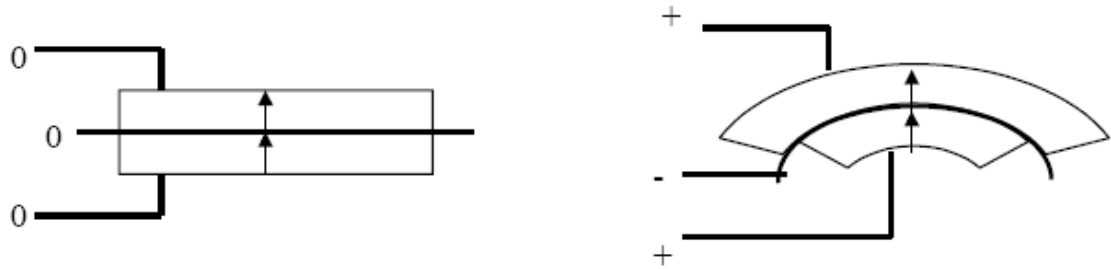


Figure 6: PZT bender configuration

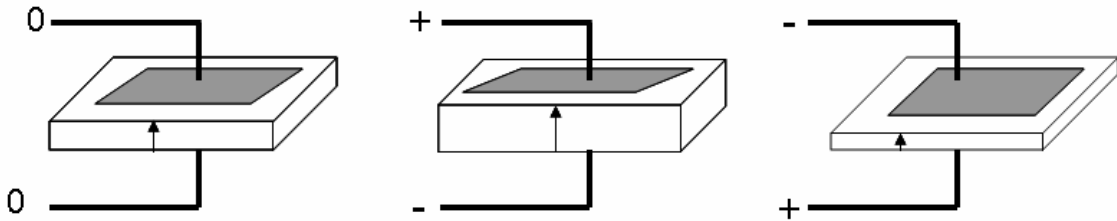


Figure 7: Basic piezoelectric modes

General unimorph and bimorph cantilevers are made of thin bulk piezoelectric patches. The poling direction of the bulk patch is perpendicular to the surface as shown in figure, thus the characteristics for the general cantilever beam are the 31-types. The 31-type configuration has the poling direction perpendicular to the stress direction and electrodes cover the whole top and bottom surface of the piezoelectric layer.

### 3 Modeling and Simulation

Among the several energy conversion materials, piezoelectric materials are widely used for smart structures, normally classified into two different types based on the energy conversion direction. The first one is the actuator type, in which the piezoelectric element undergoes a dimension change when an electric field is applied. The electric energy is converted into mechanical energy based on the indirect piezoelectric effect. The second type is called the sensor type, in which an electric charge is produced when a mechanical stress is applied. The PZT-generator is based on the mechanical-to-electrical energy conversion based on the indirect piezoelectric effect.

Major research in the piezoceramic materials till date has been related to actuations. A new and up-coming research is power harvesting using piezoelectric materials as generator. A study for power harvesting from Piezoelectric ceramics (PZT) date back to 1984, when a group of researchers implanted polyvinylidene fluoride (PVDF) patch onto the rib cage of a mongrel dog to harvest energy (Hausler [8]). Other research followed, and many have been successful in harvesting several microwatts to milliwatts of usable power.

Objectives of this effort is to develop an analytical model of the generator that facilitates estimation of the amount of power possibly being harvested at a given vibration level. Ultimately, it should provide designers with an explicit way to improve its performance. Additionally, the model can be used for the parametric studies of the

device conditioned in fabrication and design and for environmental effect such as temperature.

A two layer bender (bimorph) cantilever beam with a proof mass, as shown in Figure 8 was constructed for the power harvesting device. The bender consists for three layers with top and bottom PZT layer and a metal shim as the middle layer has been chosen for two reasons. Firstly, the bending element has been chosen as the basis for a generator rather than a stack because of the lower resonance frequencies between 60 Hz and 200 Hz and higher strains attainable. Finally, for a given force input, the cantilever configuration results in the highest average strain, and the power output is closely related to the average strain developed in the bender.

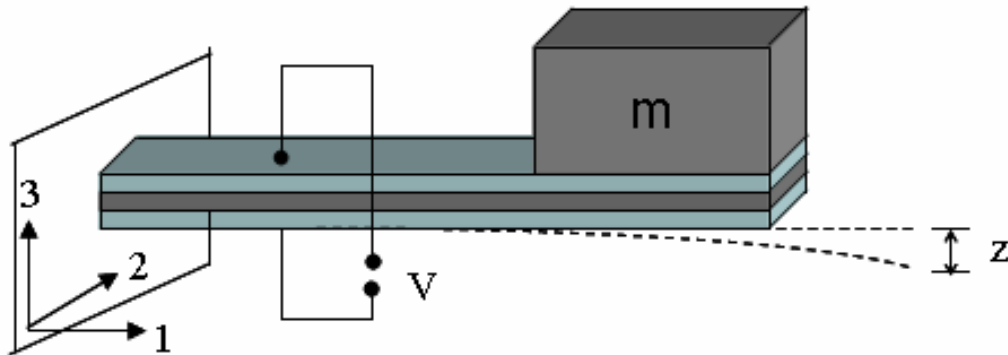


Figure 8: A two layer PZT bender mounted as cantilever beam [6]

### 3.1 Modeling techniques

The main objective for the research effort is to find a more precise and predictive model of power harvesting that ultimately facilitates parametric studies on the PZT bender to further optimize the power harvesting process and environmental effect such as temperature. The PZT generator will be modeled using 2 different techniques to evaluate

voltage and power produced from vibrational energy. The previous model published in the literature specifically targets the PZT bender in the actuator mode for a unimorph structure. In this research, the models developed have been extended to a bimorph PZT bender in sensor mode for power generation and implemented in Matlab/Simulink. These models are then compared with the experimental results to assess the accuracy of the various models.

### 3.2 Electrical equivalent model

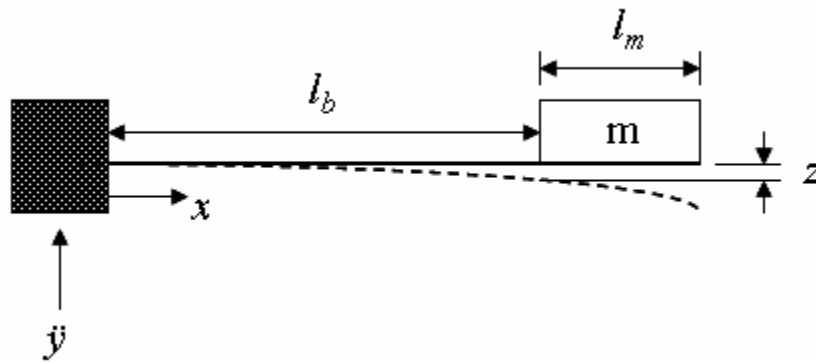


Figure 9: A schematic diagram of a PZT cantilever beam [2]

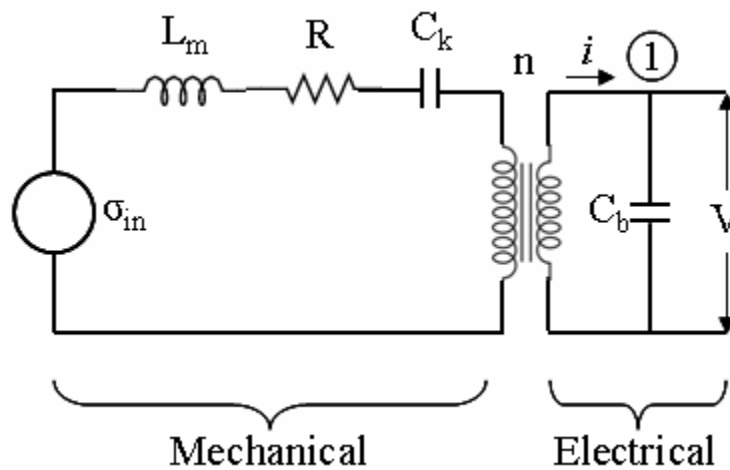


Figure 10: Circuit representation of a PZT beam [8]

The moment of inertia (I) for a beam structure composed with three layers is described as follows:

$$I = \left[ \frac{wt_p^3}{12} + wt_{sh}b^2 \right] + \frac{\eta_s wt_{sh}^3}{12} \quad (9)$$

where  $\eta_s$  is the ratio of elasticity of PZT and brass,  $w$  is the width of the beam,  $t_p$  and  $t_{sh}$  are the thickness of PZT and brass layer,  $b$  is the center-to-center distance between the brass layer and PZT layer.

The equivalent input stress of the bender,  $\sigma_{in}$ , is proportional to the input force  $F_{in}$  exerted by the proof mass as a direct result of the input vibration  $\ddot{y}$ . Therefore,

$$\begin{aligned} \sigma_{in} &= k_1 F_{in} \\ \sigma_m &= k_1 F_m \end{aligned} \quad (10)$$

where  $k_1$  is a geometric constant relating the average stress in the piezoelectric material to force exerted by the mass on the end of the beam.

The term  $m(\ddot{y} + \ddot{z})$  is a sum of the input forces,  $F_{in}$ , and the inertial force  $F_m$ .

$$F = F_{in} + F_m = m(\ddot{y} + \ddot{z}) \quad (11)$$

The moment and the average stress in the beam are given as follows;

$$M(x) = m(\ddot{y} + \ddot{z}) \left( l_b + \frac{1}{2} l_m - x \right) \quad (12)$$

$$\sigma = \frac{1}{l_e} \int_0^{l_e} \frac{M(x)b}{I} dx \quad (13)$$

Where,

$\sigma$  is the average stress in the beam.



$x$  is the distance from the base of the beam.

$M(x)$  is the moment in the beam as a function of the distance ( $x$ ) from its base.

$l_m$  is the length of the mass.

$l_e$  is the effective length of the beam.

$\ddot{y}$  is the input vibration in terms of acceleration.

$z$  is the vertical displacement of the beam at the point where the mass attaches with respect to the base of the beam.

Integrating equation (13)

$$\sigma = F \frac{b(2l_b + l_m - l_e)}{2I} \quad (14)$$

The constant  $k_l$  is then given by

$$k_l = \frac{b(2l_b + l_m - l_e)}{2I} \quad (15)$$

The following equation was used to derive the tip deflection of the beam to average strain in the piezoelectric material

$$\frac{d^2z}{dx^2} = \frac{M(x)}{E_p I} \quad (16)$$

Where  $E_p$  is the Young's modulus of elasticity of PZT.

Integrating equation (15) to obtain an expression for the deflection,  $z$  (at  $x=l_b$ ), yields

$$z = \frac{m \left( \ddot{y} + \ddot{z} \right) l_b^2}{2E_p I} \left( \frac{2}{3} l_b + \frac{1}{2} l_m \right) \quad (17)$$

On substituting  $\sigma = E_p \varepsilon$  and  $F = m(\ddot{y} + \ddot{z})$  into equation (13) and rearranging

$$m\left(\ddot{y} + \ddot{z}\right) = \frac{2E_p I}{b(2l_b + l_m - l_e)} \varepsilon \quad (18)$$

Substituting back equation (17) in equation (16)

$$z = \varepsilon \frac{l_b^2 \left(2l_b + \frac{3}{2}l_m\right)}{3b(2l_b + l_m - l_e)} \quad (19)$$

Let  $k_2$  be defined as the relationship between  $z$  and  $\varepsilon$ , and  $z = k_2\varepsilon$ .

$$k_2 = \frac{l_b^2 \left(2l_b + \frac{3}{2}l_m\right)}{3b(2l_b + l_m - l_e)} \quad (20)$$

As with purely electrical circuits, the system equations are then determined using Kirchhoff's voltage law (KVL) and Kirchhoff's current law (KCL). Taking the sum of 'voltages' around the mechanical side of the circuit yields the expression in equation (20). Summing the currents at node 1 in Figure 10 yields the expression in equation (21).

$$\sigma_{in} = L_m \ddot{\varepsilon} + R_b \dot{\varepsilon} + \frac{\varepsilon}{E_{sh}} + nV \quad (21)$$

$$i = C\dot{V} \quad (22)$$

The equivalent inductor,  $L_m$ , represents the mass or inertia of the generator. The equivalent resistor,  $R_b$ , represents mechanical damping. The equivalent capacitor, represents the mechanical stiffness, relating stress to strain is simply the compliance constant or the inverse of the elasticity,  $E_p$ .  $\sigma_{in}$  is an equivalent stress generator that represents the stress developed as a result of the input vibrations.  $n$  represents the

equivalent turns ratio of the transformer.  $C$  is the capacitance of the piezoelectric bender.  $V$  is the voltage across the piezoelectric device.

In order for these expressions to be transformed into a usable system model, equivalent expressions for  $\sigma_{in}$ ,  $L_m$ ,  $R_b$ ,  $C$ ,  $n$ , and  $i$  need to be determined.

The inductor,  $L_m$ , represents the effect of mass or the inertial term. Since  $\sigma_m = k_1 k_2 m$ , therefore

$$L_m = k_1 k_2 m \quad (23)$$

The damping force can be expressed as a function of velocity

$$F_{bm} = b_m \ddot{z} \quad (24)$$

The equivalent resistance  $R$  relates to stress ( $\sigma$ ) to strain rate ( $\dot{\varepsilon}$ )

$$\begin{aligned} \frac{\sigma_{bm}}{k_1} &= b_m k_2 \dot{\varepsilon} \\ R &= k_1 k_2 b \end{aligned} \quad (25)$$

Also the electric field in the piezoelectric material is related to the voltage across the PZT bender by following equations

$$H = \frac{V}{2t_p} \quad (26)$$

The piezoelectric constitutive relationship between voltage ( $V$ ) and stress ( $\sigma$ ) is given by

$$\begin{aligned} \sigma &= -d_{31} E_p H \\ \sigma &= nV \end{aligned} \quad (27)$$

where  $n = \frac{-d_{31} c_p}{n_p t_c}$

The constitutive relationships are shown as follows.

$$\begin{aligned}\varepsilon &= \frac{\sigma}{Y} + dH \\ D &= \varepsilon H + d\sigma\end{aligned}\quad (28)$$

The current,  $i$ , as shown in figure 10 represents the current generated as a result of the mechanical stress evaluated at zero electric field. Applying this condition (zero electric field) to equation (27) and substituting strain for stress yields

$$D = d_{31} E_p \varepsilon \quad (29)$$

The electrical displacement  $D$  is the charge density across a dielectric element, which is related to the current for the bender device;

$$i = w l_e \dot{D} \quad (30)$$

Substituting equation (28) into (29) yields

$$i = w l_e d_{31} E_p \dot{\varepsilon} \quad (31)$$

On the other hand, the capacitance of the PZT bender is given by

$$C = \frac{\varepsilon_0 w l_e}{2 t_p} \quad (32)$$

As a result, the following equation is obtained, which includes variables of  $\varepsilon$ ,  $\dot{\varepsilon}$ , and  $V$ ;

$$\begin{aligned}\ddot{\varepsilon} &= \frac{-E_p}{k_1 k_2 m} \varepsilon - \frac{b_m}{k_1 m} \dot{\varepsilon} + \frac{E_p}{k_1 k_2 m} \frac{d_{31}}{n_p t_p} V + \frac{\ddot{y}}{k_2} \\ \dot{V} &= \frac{n_p t_p d_{31} E_p}{\varepsilon_0} \ddot{\varepsilon}\end{aligned}\quad (33)$$

### 3.3 Conservation of energy principle

The method is based on the principle that the total energy of the PZT bender produced is equal to the sum of the mechanical energy applied to the beam, where electric field induced strains are considered.

The bimorph cantilever beam designed consists of two piezoelectric outer layers bonded on a metal shim layer. The beam is symmetrically constructed along the cross section, and thus the neutral surface lies on the middle surface of the beam. However, the polarities of two piezoelectric layers are in opposite directions to each other to increase the voltage generated. Thus, the upper and lower piezoelectric layer's electric fields are opposite to each other. As a result, the upper PZT layer is considered to have a negative electric field, while the lower one is positive.

Accordingly, the mechanical strains of the upper PZT layer can be expressed by the constitutive equations. The established constitutive equations for a linear piezoelectric material in reduced matrix form are

$$\begin{aligned}\{\varepsilon\} &= [s^E]\{\sigma\} + [d]^T \{H\} \\ \{D\} &= [d]\{\sigma\} + [v^T]\{H\}\end{aligned}\quad (34)$$

Where  $\{\varepsilon\}$  is the six-dimensional strain vector,  $\{\sigma\}$  is the vector of stresses,  $\{D\}$  is the three dimensional electric displacement vector,  $\{H\}$  is the electric field vector,  $[s^E]$  is the six by six compliance matrix evaluated at constant electric field,  $[d]$  is the three by six matrix of piezoelectric strain coefficients, and  $[v^T]$  is the three by three dielectric constant matrix evaluated at constant stress.

A two layer bending element mounted as a cantilever beam as shown in the Figure 2 is assumed. As is the generally the case for bending elements, the material is

poled along the 3 axis and electrodes are placed on the surfaces perpendicular to the 3 axis. Driving vibrations are assumed to exist only along the 3 axis. The piezoelectric material will experience a one dimensional state of stress along the 1 axis. Under this stress state, the piezoelectric constitutive equations reduce to the expression below.

$$\begin{aligned}\varepsilon_1 &= s_{11}^E \sigma_1 - d_{31} H_3 \\ D_3 &= -d_{31} \sigma_1 + \nu_{33}^T H_3\end{aligned}\quad (35)$$

where

$\varepsilon_1 \rightarrow$  Strain

$\sigma_1 \rightarrow$  Stress

$d_{31} \rightarrow$  Piezoelectric constant

$s_{11}^E \rightarrow$  Elastic compliance constant for constant electric Field

$H_3 \rightarrow$  Electric field strength

$\nu_{33}^T \rightarrow$  Permittivity constant, dielectric constant at constant stress

$D_3 \rightarrow$  Electric charge density

Likewise, the lower PZT layer is described by the equation below

$$\begin{aligned}\varepsilon_1 &= s_{11}^E \sigma_1 + d_{31} H_3 \\ D_3 &= d_{31} \sigma_1 + \nu_{33}^T H_3\end{aligned}\quad (36)$$

In fact, the material of the middle layer is a non piezoelectric layer and thus the stress-strain relation is simply given by equation

$$\varepsilon_1 = \frac{\sigma_1}{E_{sh}} \quad (37)$$

Where,  $E_{sh}$  is the Young's modulus.

Generally, the energy stored in a PZT layer is the sum of the mechanical energy and the electric field induced energy.

$$\text{Energy} = \frac{1}{2} * \text{Strain} * \text{Stress} + \frac{1}{2} * \text{Charge} * \text{Electric field} \quad (38)$$

On the other hand, the moment at an arbitrary coordinate  $x$  along a cantilever beam with a given length  $l$  can be expressed by

$$M(x_1) = F_o * (l - x_1) = \int \sigma(\varepsilon(x_1, z), H_3) z dz \quad (39)$$

Where  $F_o$  is the applied forcing function term. The total moment  $M$  in the beam is as follows;

$$M = \int_{\frac{t_{sh}}{2}}^{\frac{t_{sh}+t_p}{2}} \frac{1}{S_{11}^E} (-\rho z + d_{31} H_3) W z dz + \int_{-\frac{t_{sh}}{2}}^{\frac{t_{sh}}{2}} -\frac{1}{S_m} W \rho z^2 dz + \int_{-\frac{t_{sh}}{2}}^{\frac{t_{sh}}{2}} \frac{1}{S_{11}^E} (-\rho z - d_{31} H_3) W z dz \quad (40)$$

The equation above is rearranged to obtain the curvature  $\rho$  as a function of the force ( $F_o$ ) and the electric field ( $H_3$ );

$$\rho = -\frac{12s_m s_{11}^E (l-x)}{XW} F_o + \frac{12d_{31} s_m t_p (t_{sh} + t_p)}{X} H_3 \quad (41)$$

$$X = 12s_m t_p^2 t_{sh} + 8s_m t_p^3 + 6s_m t_p t_{sh}^2 + s_{11}^E t_{sh}^3$$

Hence, a general form of the curvature of the beam is given with a function of force and electric field.

$$\rho(x, F_o, H_3) = f_1(x, F_o) + f_2(x, H_3) \quad (42)$$

The total energy of the beam is given as

$$U = \int_0^L \int_0^w \left( \int_{\frac{t_{sh}}{2}}^{\frac{t_{sh}+t_p}{2}} dU_u dz + \int_{-\frac{t_{sh}}{2}}^{\frac{t_{sh}}{2}} dU_m dz + \int_{-\frac{t_{sh}}{2}}^{\frac{t_{sh}}{2}} dU_l dz \right) dy dx \quad (43)$$

$$U = \frac{2s_{11}^E s_m l^3}{Xw} F_o^2 - \frac{6d_{31} s_m t_p (t_{sh} + t_p) l^2}{X} F_o H_3 + v_{ss}^T w l t_p \left( 1 + \frac{(6s_m t_p (t_{sh} + t_p)^2 - X)}{X} K_{31}^2 \right) H_3^2 \quad (44)$$

On the other hand, the electric field is given by

$$\text{Electric Field (H)} = \frac{\text{Voltage across electrode(V)}}{\text{PZT thickness between electrode}} \quad (45)$$

$$H_3 = V / t = V / (2t_p)$$

The total electrical energy is equal to a product of the charge and the voltage. Thus, the charge generated in the beam is obtained by a partial derivative of the total energy with respect to the voltage.

$$Q_{Gen} = \frac{\partial U_{total}}{\partial V} = -3 \frac{d_{31} s_m (t_{sh} + t_p) l^2}{X} F_o + \frac{v_{33}^T w l}{2t_p} \left( 1 + \frac{(6s_m t_p (t_{sh} + t_p)^2 - X)}{X} K_{31}^2 \right) V \quad (46)$$

The charge obtained from the equation above is in terms of the applied force and the electric field boundary condition. If the applied voltage is zero, the second term becomes a zero and the charge is only a function of the force imposed.

$$Q_{Gen} = -3 \frac{d_{31} s_m (t_{sh} + t_p) L^2}{X} F_o \quad (47)$$

The capacitance of the piezoelectric material is described as the relation between the voltage and charge on the piezoelectric material. The second term in our generated charge expression shows the relation between the charge and the voltage, hence the capacitance C of the beam can be found, where no force is applied.



$$C = \frac{\nu_{33}^T w l}{2t_p} \left( 1 + \frac{(6s_m t_p (t_{sh} + t_p)^2 - X)}{X} K_{31}^2 \right) \quad (48)$$

Thus, the voltage generated is found as a function of the applied force;

$$V_{Gen} = \frac{Q_{Gen}}{C} = - \frac{6d_{31} s_m t_p (t_{sh} + t_p) l}{\nu_{33}^T w X \left( 1 + \left( \frac{6s_m t_p (t_{sh} + t_p)^2}{X} - 1 \right) K_{31}^2 \right)} F_o \quad (49)$$

Likewise, the total electric energy generated from force  $F_o$  can be expressed as follows:

$$U_{Gen} = Q_{Gen} V_{Gen} = \frac{18d_{31}^2 s_m^2 t_p (t_{sh} + t_p)^2 l^3}{\nu_{33}^T w X^2 \left( 1 + \left( \frac{6s_m t_p (t_{sh} + t_p)^2}{X} - 1 \right) K_{31}^2 \right)} F_o^2 \quad (50)$$

The schematic structure of a sensor is shown in Fig 5, where a mass ( $M_{end}$ ) is attached to the free end of the bimorph PZT cantilever beam that is fixed to a vibrating base. Both of piezoelectric bending composite beam and  $M_{end}$  are assumed to be rigid bodies and no elastic coupling. Then, the structure can be modeled with a single degree of freedom (SDOF) system, which solely consists of a proof mass  $M$ , a spring with stiffness  $K$ , a damper with damping coefficient  $C$  and a vibrating base. The resulting equivalent model is shown in Figure 11. Hence,  $y(t)$  is the motion of vibrating base, and  $z(t)$  is the relative motion between the vibrating base and the proof mass  $M$  that is assumed to be a point mass with equivalent vertical force at the free end of the sensor. Thus, the mass can be expressed by a following equation [26];

$$m = \frac{33}{140} M_{beam} + M_{end} \quad (51)$$

where  $M_{beam}$  is the mass of the beam and  $M_{end}$  is the end mass and  $m$  is the equivalent mass.

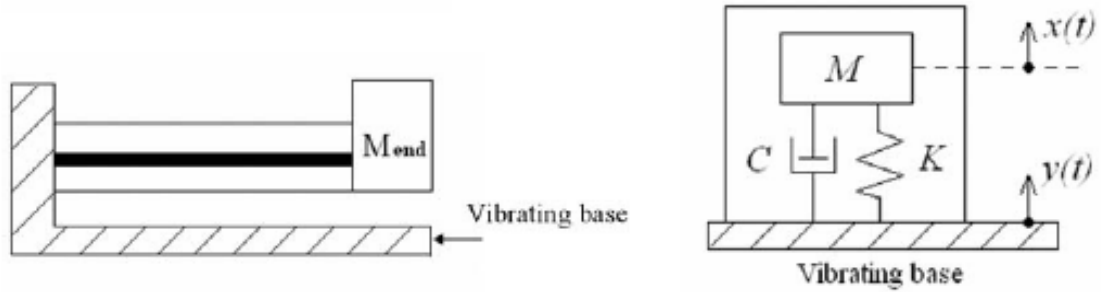


Figure 11: Sensor structure and equivalent SDOF model

The equivalent spring constant is given by [26]

$$K = \frac{AwE_{sh}E_p}{4l^3} \quad (52)$$

$$A = 2(3t_{sh}^2t_p + 6t_{sh}t_p^2 + 4t_p^3) / E_{sh} + t_{sh}^3 / E_p$$

where,

$t_{sh}$  = thickness of shim layer

$t_p$  = thickness of PZT layer

$E_{sh}$  = Young's modulus of metal layer

$E_p$  = Young's modulus of PZT layer

$l$  = length of the cantilever beam

$w$  = width of the cantilever beam

According to the Newton's second law, the mechanical model is derived as follows:

$$M \ddot{z} + C \dot{z} + Kz = -M \ddot{y} \quad (53)$$

A transfer function between the input acceleration and the output displacement can be

obtained in the Laplace plane with initial conditions  $z(0) = \dot{z} = 0$ , where  $\omega_n = \sqrt{\frac{K}{M}}$ ,

$\zeta$  = damping ratio .

$$\left| \frac{Z(s)}{\ddot{Y}(s)} \right| = \frac{1}{s^2 + (2\zeta\omega_n)s + \omega_n^2} \quad (54)$$

So, the response of the force  $F_o$  at the beam is obtained after  $Z(t)$  and  $\ddot{Z}(t)$  is solved from the equation.

$$F_o(t) = M_{end} \times \ddot{Z}(t) \quad (55)$$

### 3.4 Coupled field model

One can formulate a general model for the conversion of the kinetic energy of a vibrating mass to electrical power based on linear system theory without specifying the mechanism by which the conversion takes place. A lumped parameter model is used to describe the PZT generator. Figure 12 shows the mechanical model of the system. The equivalent mass,  $m$ , and spring stiffness,  $k$ , is determined using a Raleigh-Ritz method with a shape function generated using standard beam theory with a constant acceleration load. The mechanical damping coefficient can be approximated using half amplitude method.  $F_e$  is the lumped electrical force generated by electrically induced strains in the piezoelectric layers.

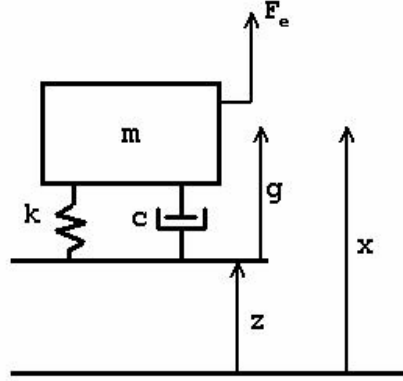


Figure 12: Lumped mechanical model for PZT generator.

The equation of motion for the generator is essentially that of an accelerometer with an additional force term.

$$\ddot{g} + \frac{c}{m} \dot{g} + \frac{k}{m} g = \frac{F_e}{m} - \ddot{z} \quad (56)$$

The input energy into the system is determined by the force and velocity at the base of the structure. The input force is determined by summing the forces on the system.

$$F_{in} = F_e - c \dot{g} - kg \quad (57)$$

By integrating the force-velocity product the input energy can be evaluated:

$$U_{in}(t) = \int_t F_{in}(\tau) \dot{z}(\tau) d\tau \quad (58)$$

Other energy terms associated with the mechanical system are the energy dissipated by the damper [26]:

$$U_{damp}(t) = \int_t c \dot{g}(\tau)^2 d\tau \quad (59)$$

The energy in the spring:

$$U_k(t) = \frac{1}{2}kg(t)^2 \quad (60)$$

The energy in the mass:

$$U_m(t) = \frac{1}{2}m\dot{x}(t)^2 \quad (61)$$

The last energy term in the mechanical system is the energy transferred to the electrical domain of the generator:

$$U_{me}(t) = \int_t F_e(\tau)g(\tau)d\tau \quad (62)$$

While the net flow of energy is from the mechanical to the electrical domain, there can be time intervals where this term is negative.

### 3.4.1 Electrical Energy Terms

The lumped electrical model for the PZT generator is shown in Figure 13.

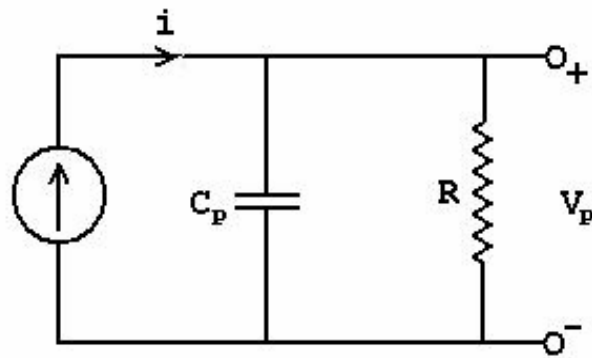


Figure 13: Lumped electrical model for PZT generator.

This model is more natural than a voltage source model in estimating the voltage-load relationship in cases of an open or shorted load. The voltage dynamic for the electrical subsystem is given:

$$\dot{V}_p + \frac{V_p}{RC_p} = \frac{i}{C_p} \quad (63)$$

The input energy into the electrical circuit is given by the current-voltage relationship:

$$U_{Ein}(t) = \int_t i(\tau)V_p(\tau)d\tau \quad (64)$$

The energy flowing into the electrical circuit is dissipated at the load resistance, stored in the capacitor, or dissipated as heat. The energy in the capacitor is:

$$U_{cap}(t) = \frac{1}{2}C_p V_p(t)^2 \quad (65)$$

where  $C_p$  is the complex valued capacitance that incorporates the loss tangent in order to account for dielectric losses that are dissipated as heat. The output energy of the system is:

$$U_{out}(t) = \int_t \frac{V_p(\tau)^2}{R} d\tau \quad (66)$$

### 3.4.2 Electro-Mechanical Coupling

In order to determine how the electrical and mechanical subsystems are coupled, the displacement-voltage relationship needs to be determined. This can be accomplished by looking at the moment distribution across a section of the beam [47].

$$M = \sum_i \int_{A_i} E_i \left( \frac{y}{R} + d_{31_i} \mathbf{H}_i \right) dA_i \quad (67)$$

Where  $i$  denote the sections of the beam,  $y$  is the distance from the beams neutral axis,  $E$  is Young's Modulus,  $R$  is the radius of curvature at the given cross section,  $d_{31}$  is the piezoelectric constant, and  $\mathbf{H}$  is the electric field. In the device being analyzed the beam has 3 layers, a mechanical layer sandwiched between two piezoelectric layers with opposite poling. Rewriting the first equation:

$$M = w \int_{-\frac{t_{sh}}{2}}^{\frac{t_{sh}}{2}} y E_{sh} \frac{y}{R} dy + 2w \int_{\frac{t_{sh}}{2}}^{\frac{t_{sh}}{2} + t_p} y E_p \left( \frac{y}{R} + d_{31} \mathbf{H} \right) dy \quad (68)$$

Where  $w$  is the width of the beam,  $t$  is the layer thickness (subscripts denoting (p)iezoelectric and (sh)im layers), and the electric field for the series poling is  $\mathbf{H} = -V_p / 2t_p$ . In accordance with typical linear beam theory the radius of curvature is roughly:

$$R = \left( \frac{\partial^2 g}{\partial^2 s} \right)^{-1} \quad (69)$$

where  $g(s)$  is the beam deflection function over the length coordinate of the beam,  $s$ . For consistency it should be noted that  $g(l) = g$  the gap given in the mechanical model,  $l$  being the length of the cantilever. The moment equation for the beam assuming a simple tip load is:

$$M(s) = F(l - s) \quad (70)$$

Combining the previous three equations and integrating two times with respect to  $s$ , the tip load,  $F$ , can be evaluated:

$$F(g) = \frac{gwE_{sh}t_{sh}^3}{4l^3} + \frac{gwE_p}{l^3} \left[ \frac{3}{2}t_{sh}^2t_p^2 + 3t_{sh}t_p^2 + \frac{1}{2}t_p^3 \right] + \frac{3wE_p d_{31} \mathbf{H}}{2l} [t_{sh}t_p + t_p^2] \quad (71)$$

The terms including  $g$  are equivalent to the spring force,  $kg$ , from standard beam theory already accounted for in the mechanical model.  $F_e$  is the remaining term.

$$F_e(t) = \frac{-3wE_p d_{31} V_p(t)}{4l} [t_{sh} + t_p] \quad (72)$$

Finally the input current to the electrical circuit can be determined using energy conversion between the two domains.

$$\int_t i(\tau) V_p(\tau) d\tau = - \int_t F_e(\tau) g(\tau) \dot{\tau} d\tau \quad (73)$$

Solving for  $i$ :

$$i(t) = \frac{-3wE_p d_{31}}{4l} [t_{sh} + t_p] \dot{g}(t) \quad (74)$$

Using the ideas developed above a state-space model of the PZT generator can be developed. The state-space model is given:

$$\begin{bmatrix} \dot{x}_1 \\ \dot{x}_2 \\ \dot{x}_3 \end{bmatrix} = \begin{bmatrix} 0 & 1 & 0 \\ -k/m & -c/m & \alpha_p/m \\ 0 & -\alpha_p/C_p & 1/RC_p \end{bmatrix} \begin{bmatrix} x_1 \\ x_2 \\ x_3 \end{bmatrix} + \begin{bmatrix} 0 \\ -a \\ 0 \end{bmatrix} \ddot{z} \quad (75)$$

where the states are the displacement, velocity, and voltage respectively. The mass, spring constant, damping coefficient, load resistance, and piezoelectric capacitance are the same as discussed previously. The acceleration,  $a$ , is the input amplitude in  $m/s^2$ . The piezoelectric capacitance,  $C_p$ , and the coupling constant,  $\alpha_p$ , depend on the poling of the PZT layers.

For poling in the same direction, the wiring is done in parallel:

$$\alpha_p = \frac{3wE_p d_{31}}{2l} [t_m + t_p] \quad (76)$$



$$C_p = \frac{2\varepsilon A}{t_p} [1 - j \tan \delta] \quad (77)$$

### 3.5 Modeling of Temperature Effect

#### 3.5.1 Temperature effect on PZT material properties

Since piezoelectricity constitutes relation between electrical and mechanical processes, and the related phenomenon pyroelectricity is due to thermal-electrical coupling, the general set of electrical, mechanical and thermal processes depicted in Figure 14. The intensive variables electric field  $E$ , stress  $\sigma$ , and temperature  $T$  are represented at vertices of the outer triangle whereas the corresponding conjugate extensive variables polarization  $P$ , strain  $\varepsilon$ , and change in entropy  $S$  are represented on the inner triangle.

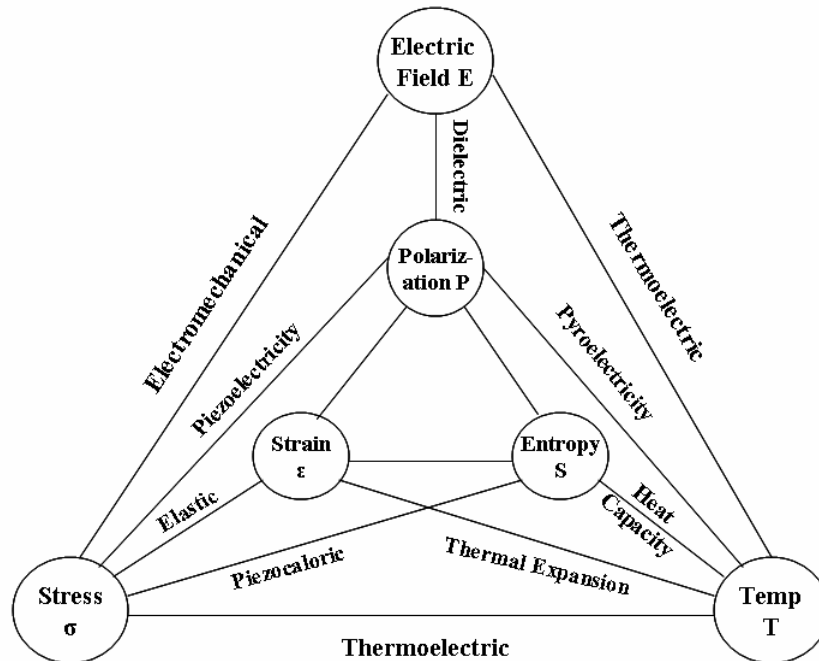


Figure 14: Interaction between the electrical, mechanical and thermal processes [48].

There are many methods for formulating non-linear temperature dependent relations for ferroelectric compounds. One method is to assume the function is an infinite series in the independent variables. Polynomial formulation can be described as phenomenological in nature, where constants are chosen to match observed physical behavior. This approach was used in formulation the temperature dependence properties of the PZT material. The experimental data [50] for dielectric constant and piezoelectric charge coefficient were plotted in Microsoft excel software and a fourth order curve fitting was done to get the correlation between the material properties of the PZT and temperature.

The constants given in the equation above are obtained from the experimental data given in the reference [50], where the variation of the relative dielectric constant, the piezoelectric strain constant,  $d_{31}$ , and the resistivity of PZT-5H material are provided as function of temperature. The data can be interpolated by different functions, which are graphically depicted in Figure 15, and Figure 16.

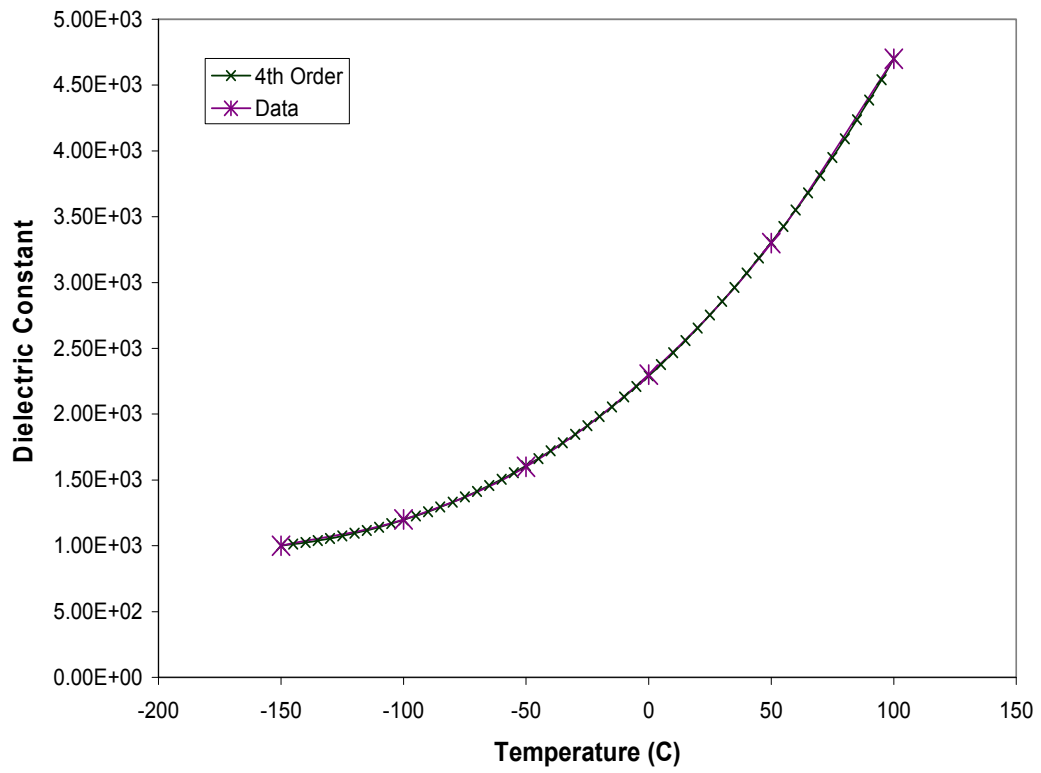


Figure 15: Influence of temperature on the dielectric constant

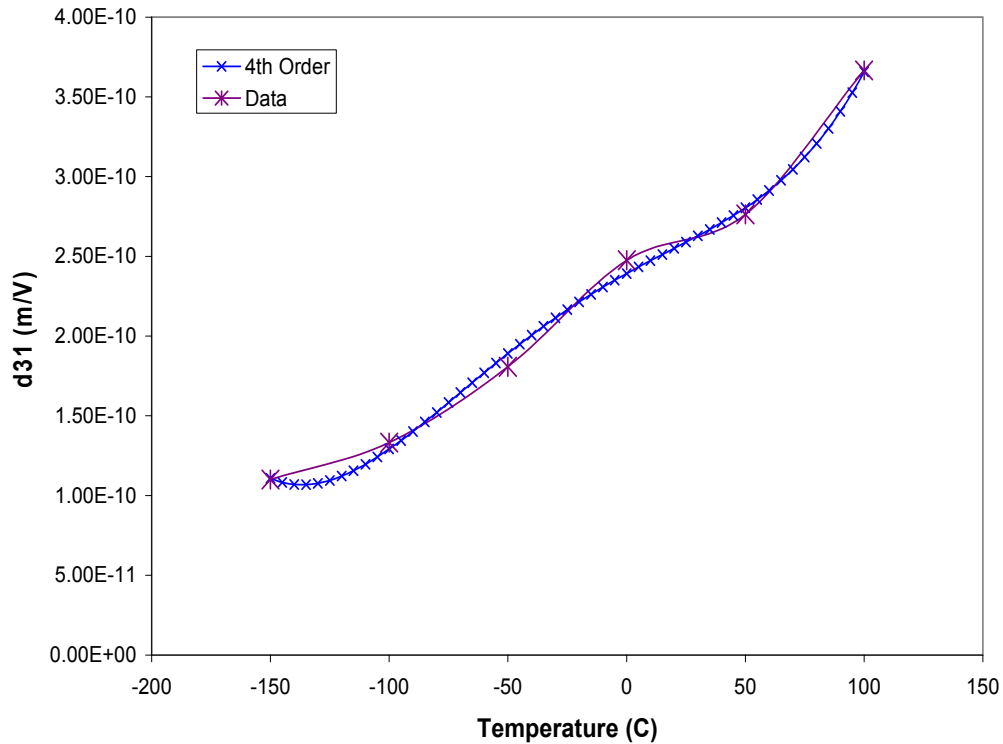


Figure 16: Influence of temperature on the piezoelectric strain constant,  $d_{31}$  [23]

When temperature rises, both the dielectric and the piezoelectric strain constant of the material 5H tend to significantly increase. In addition, the Young's modulus of the PZT is known to being slightly dependent on the change in temperature. The dielectric constant among the temperature dependent constants exhibits the most significant effect on the electric impedance of PZT. Most of the previous work is concerned with very large magnitudes of temperature variations at extremely high temperatures. Changes in temperature have distinct effects on the dynamic properties of structures, which is dependent on boundary conditions, temperature distribution and structure materials. However, the exact nature of these relationships on effect on power generation has not been investigated by any researcher as gathered from previously published papers. The

correlation for temperature dependence of dielectric constant and charge coefficient can be found from the data plotted in Figure 15 and Figure 16.

For charge coefficient,  $d_{31}$ :

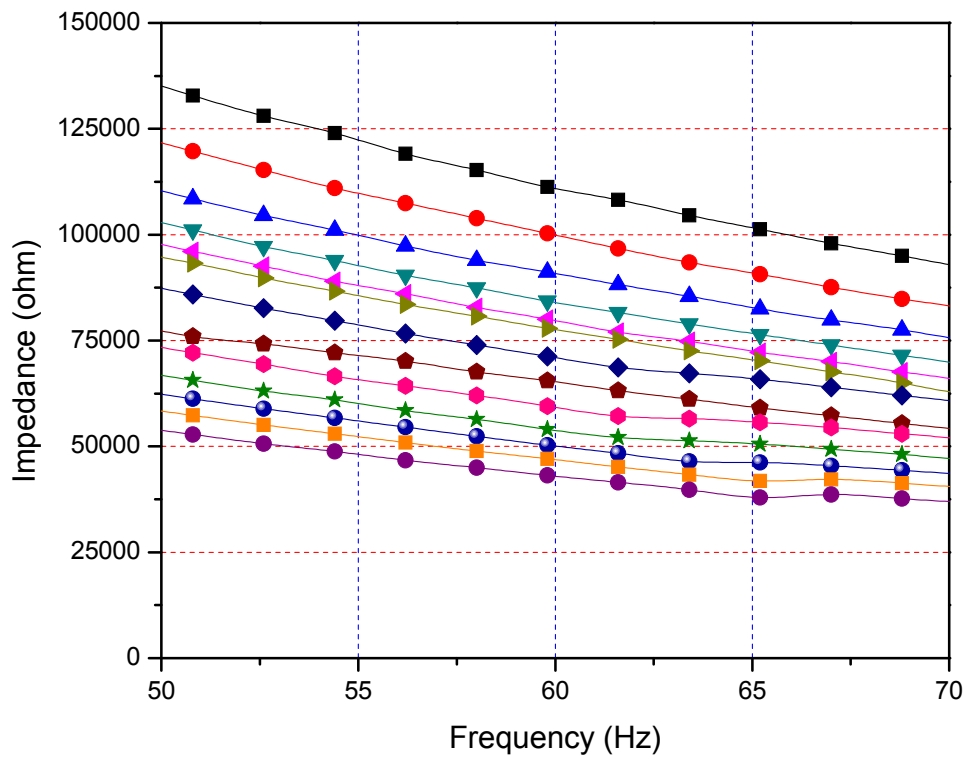
$$d_{31} = (2.39e-10) + (8.24e-13) * T - (2.67e-15) * T^2 + (3.59e-17) * T^3 \quad (78)$$

For dielectric constant,  $\epsilon_0$ :

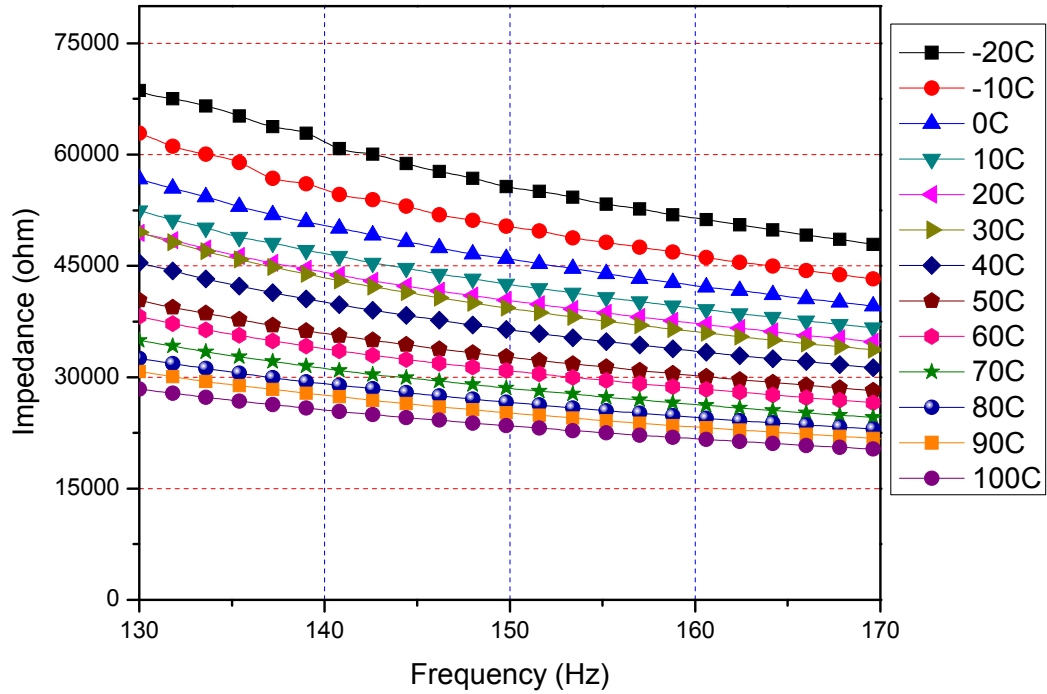
$$\epsilon_0 = (2293.1 + 16.775 * T + 0.0656 * T^2) * (8.854e-12) \quad (79)$$

### 3.5.2 Temperature effect on Impedance

The experiments were performed to measure temperature effects on variation of impedance of the PZT beam to determine the effect on resonant frequency. The measured impedance is graphically presented in Figure 17 at different frequencies. When the temperature rises, the magnitude of the impedance decreases. This baseline shift is due to the temperature dependency of piezoelectric constants as mentioned before. There were no structural resonances of the free PZT existed in these frequency ranges.



a) Lower frequency range



b) Higher frequency range

Figure 17: Temperature effect on the electrical impedance of a PZT

In the previous section, it is shown that piezoelectric materials such as PZT (5H) have strong temperature dependency, which causes significant variation of the electrical impedance with temperature change.

### 3.5.3 Temperature effect on resonant frequency

In this section, temperature effects on the resonant frequency of a PZT bimorph cantilever are investigated. The structural studies on the temperature effects are conveyed under an assumption that the PZT beam is a simple bimorph PZT cantilever with clamped-free boundary condition. The shifts in resonant frequencies will be discussed in

this section. The Young's modulus can be considered as functions of temperature based on its rates of change around reference temperature.

$$E_p(T) = E_p - \frac{(20 - T)}{160} * \frac{E_p}{4} \quad (80)$$

$$E_{sh}(T) = E_{sh} - \frac{(20 - T)}{160} * \frac{E_{sh} * 104}{110} \quad (81)$$

where  $E(T)$  is the Young's modulus at the measuring temperature,  $E$  is the Young's modulus at the reference temperature,  $p$  and  $sh$  subscripts stands for piezoelectric and shim layer,  $T$  is the measuring temperature,  $T_o$  is the reference temperature. It is also shown experimentally that the coefficient of linear thermal expansion is approximately constant over the small temperature range [23]. Therefore, the structural dimensions can be written as functions of temperature,

$$w = w_o (1 + \alpha \Delta T) \quad (82)$$

$$l = l_o (1 + \alpha \Delta T) \quad (83)$$

$$t = t_o (1 + \alpha \Delta T) \quad (84)$$

where  $w$  is the width of the beam,  $w_o$  is the reference width of the beam,  $l$  is the length of the beam,  $l_o$  is the reference length of the beam,  $t$  is the thickness of the beam,  $t_o$  is the reference thickness of the beam, and  $\alpha$  is the mean coefficient of linear thermal expansion.

Due to the thermal expansion, the beam density per unit volume also varies with temperature. Since the mass of the beam remains the same regardless of temperature and the beam is assumed isotropic, we can write



$$\rho = \frac{M}{V} = \frac{M}{w_o l_o t_o (1 + \alpha \Delta T)^3} = \frac{M}{V_o (1 + \alpha \Delta T)^3} = \frac{\rho_o}{(1 + \alpha \Delta T)^3} \quad (85)$$

where  $M$  is the mass of the beam,  $\rho$  is the mass density of the beam,  $\rho_o$  is the mass density of the beam at the reference temperature,  $V$  is the volume of the beam, and  $V_o$  is the volume of the beam at the reference temperature.

The natural frequencies of the clamped-free beam in bending have well-known solutions for the first several modes, which is:

$$f_r = \frac{\beta_r^2}{2\pi} \sqrt{\frac{EI}{\rho AL^4}} \quad (86)$$

where  $f_r$  is the natural frequency in Hz of the  $r$ th bending mode,  $\beta_r$  is the weight for the  $r$ th bending mode,  $I$  is the area moment of inertia of the beam, and  $A$  is the area of the cross section of the beam. For a beam with a constant rectangular cross section, the moment of inertia is given by  $I = \frac{wt^3}{12}$  and area of cross section is  $A=wt$ .

Then, the equation above can be rewritten to account for the temperature dependency of the material properties by incorporating equations for dependence of structural dimension as follows:

$$f_r = \frac{(\beta_r l)^2 t_p}{4\pi^2} \sqrt{\frac{(E_o + \beta \Delta T)(1 + \alpha \Delta T)}{3\rho_o}} \quad (87)$$

$$\frac{f_r}{f_{r_o}} = \sqrt{\frac{(E_o + \beta \Delta T)(1 + \alpha \Delta T)}{E_o}} \quad (88)$$

Figure 18 shows experimental data for the shift in natural frequency of the PZT cantilever as a function of temperature. The result indicates that an increase in temperature leads to a decrease in resonant frequencies, which is due to the Young's modulus effect. On the other hand, the thermal expansion increases the resonant frequencies of beam, too, although the effect is relatively small.

It is observed that an increase in temperature leads to shifting of resonant frequencies and fluctuations in peak response magnitude. The shifting of the peak frequencies indicates a variation in the structural stiffness, caused by changes in the material and structural dimensional properties. Likewise, variations in the peak response magnitude suggest a damping related phenomenon. Hence, it can be said that a combination of both structural stiffness and damping variations are involved in temperature change.

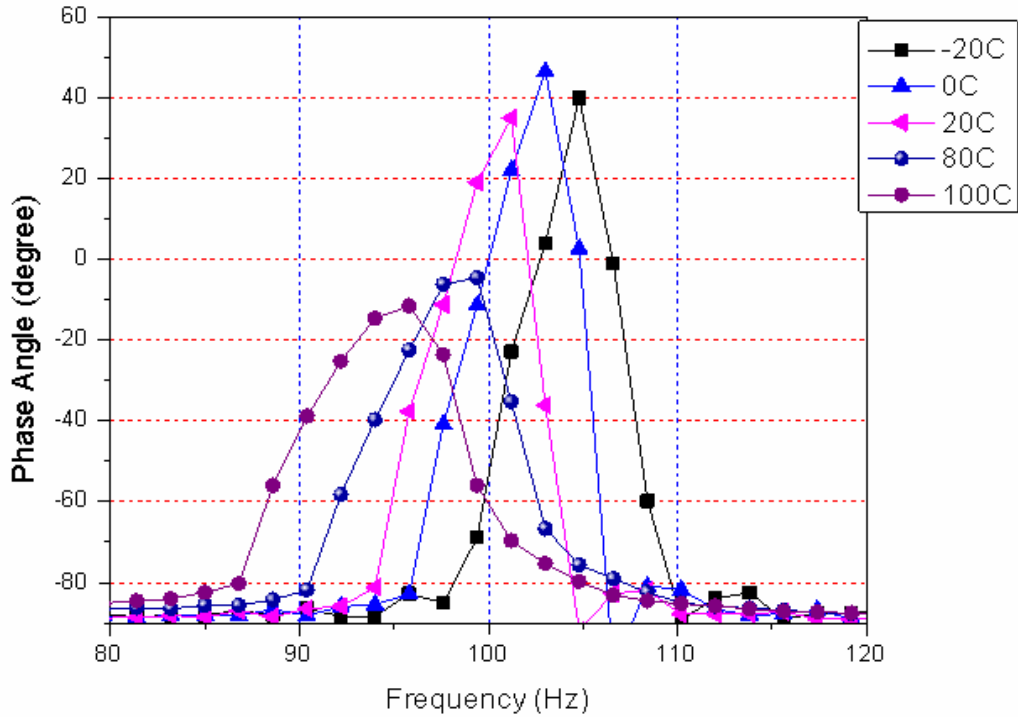


Figure 18: Shift in natural frequency of the PZT cantilever with temperature

Figure 18 shows the phase angle of the bimorph PZT cantilever beam. A real part, an imaginary part and a magnitude are demonstrated. All these plots indicate that the change in temperature leads to a horizontal shift and the peak frequencies. This verifies that the electrical impedance of PZT constitutes a unique signature of the dynamic behavior of the structure.

### 3.5.4 Temperature effect on power generation

A generalized model for the effect of change in temperature on power generation is formulated based on the couple field model developed in the earlier section of this chapter. The methodology adopted for the formulation is replacing the temperature dependent variable in the previous formulation with the corresponding temperature

dependent polynomial functions. The temperature dependent variables in the formulation are:

- Length,  $l$
- Width,  $w$
- Thickness,  $t$
- Young's modulus of PZT,  $E_p$
- Young's modulus of brass,  $E_{sh}$
- Dielectric permittivity of PZT  $\epsilon_o$
- Piezoelectric charge coefficient,  $d_{31}$ .

Conversion of the kinetic energy of a vibrating mass to electrical power based on linear system theory without specifying the mechanism by which the conversion takes place. A lumped parameter model is used to describe the PZT generator.

## 4 Experimental Setup

### 4.1 Setup for Room Temperature Measurements

The bimorph PZT bender with an attached proof mass made from Tungsten was constructed as shown in Figure 19. The bender was composed of a brass center shim sandwiched by two layer of PZT-5H. The thickness of the brass plate and the PZT is 0.134mm and 0.132mm, respectively. The length of the bender is 25mm and width is 3.2 mm. The dimensions of proof mass are length 3.03mm, width 2.95mm and height 2.9 mm and the mass is 0.502 grams. In order to investigate parameters of the prototype structure, a test setup was built to excite the bender with a predetermined resonant frequency using a shaker connected via a function generator through amplifier. The system described here is designed to utilize the z-axis vibration as the only vibration source for the device. The characterization of the fabricated cantilever device, the voltage generated was evaluated by connecting a resistor. Figure 20 illustrate the schematic of experimental setup and a photo for a real setup.

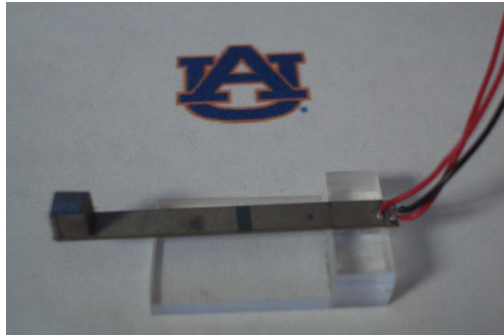


Figure 19: Bimorph PZT bender.

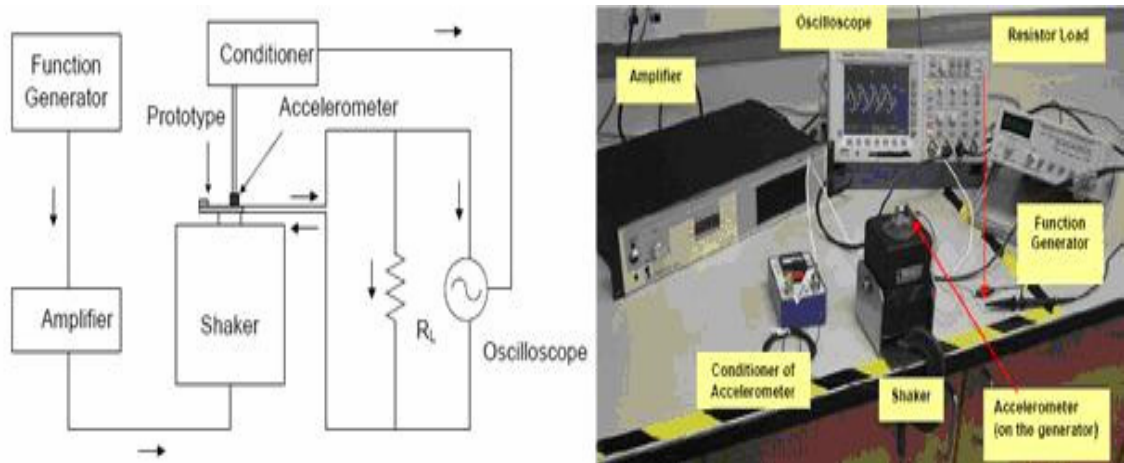


Figure 20: Schematic and picture of experimental setup.

The beam was excited by a sinusoidal input and the steady state voltage was measured across several different resistors. The accuracy of the model was compared

against experimental results to demonstrate the ability of the model to accurately predict the amount of power produced by the PZT generator when subjected to transverse vibration. To ensure the model and experimental tests were subjected to the same excitation force an accelerometer was used to calculate the amplitude of the sinusoidal acceleration applied to the beam.

## 4.2 Setup for Temperature Varying Measurements

Figure 21 is a schematic of the experimental setup. The beam was put into a temperature controlled oven and the measurements were also taken in the temperature range of from -20 °C to 70 °C in steps of 10 °C. The beam was excited by using a Labworks ET-132-203 shaker connected through a function generator and a Labworks PA119 amplifier. A Labworks miniature accelerometer (model 8636C10) and a Labworks charge amplifier were used to measure acceleration responses of the beam by using a LeCroy WaveRunner 6000A series oscilloscope.

The experiments were performed in two steps, first, the effect of temperature on the resonant frequency of the PZT beam was investigated and next, the experiments were performed at the resonant frequency determined from the first step to study the effect of change in temperature on the output voltage and power at the resonant frequency. For the first part of the experiment, for determination of resonant frequency, the experiment was performed at the temperature range of -20 °C to 70 °C in steps of 10 °C by varying the frequency of vibration from 60 to 130 Hz. The measurements were taken at the given frequency range and at the given temperature. Once it's done, the temperature was increased in step of 10 °C and next set of measurements was taken. The process was repeated 3 times to check the repeatability of the data. The experiments were performed

to measure temperature effects on variation of impedance of the PZT beam to determine the effect on resonant frequency. The experimental setup is depicted in Figure 21. Accuracy of the measurements is accomplished by considering three separate ranges of frequencies that includes the resonant frequency and the lower and higher than the resonant frequency. Magnitude and phase angle were measured and recorded at each temperature step. The experiment was conducted on a PZT (5H) bimorph cantilever specimen (25 mm x 3.2 mm x 0.25 mm) inside an oven equipped with a temperature controller. Using the controller, the temperature in the oven was set from -20°C to 70°C in steps of 10°C and the electrical impedance is measured by the Hewlett-Packard electrical impedance analyzer (model HP4294A). At each step of temperature, the impedance was measured after the temperature had reached a steady state.

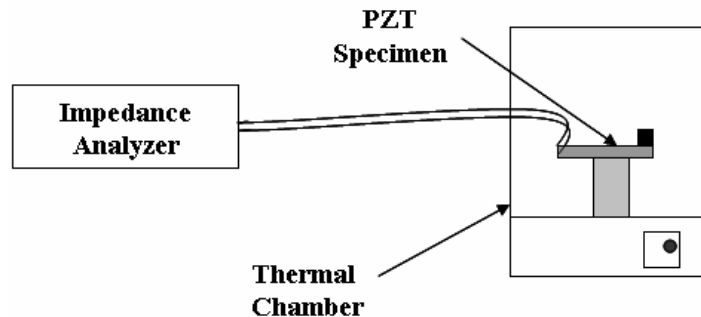


Figure 21: Experimental setup for impedance measurement

For the second step of measurements for open circuit voltage and with resistive load, the output from the PZT device is connected to the resistive load varying from 1K $\Omega$  to 3M $\Omega$ . The magnetic shaker was set to vibrate at the resonant frequency as measured from the first step with amplitude of vibration set a 1g. The output of the device is directly connected to the oscilloscope for the open circuit voltage measurements. After



the open circuit voltage measurements, to measure the power and voltage for different resistive loads, the output from the PZT device was connected to the oscilloscope through a resistor box and the resistive load is varied from  $1\text{K}\Omega$  to  $3\text{M}\Omega$  to characterize the I-V characteristics of the PZT device. The experimental setup for it is shown in Figure 22.

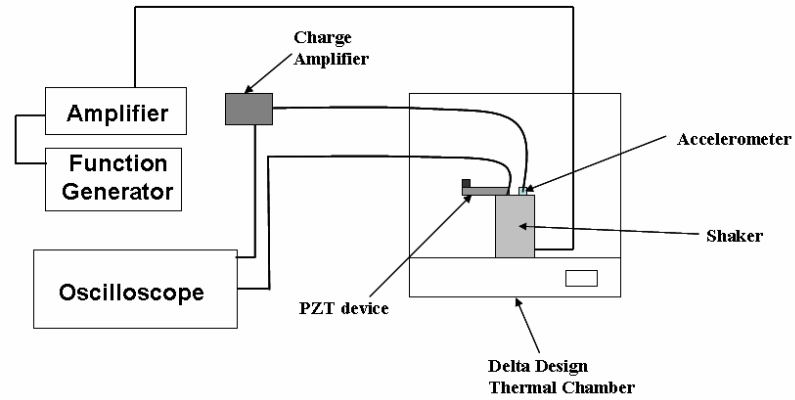


Figure 22: Schematic of the experiment on temperature effects

## 5 Power conversion circuit design

The PZT bender produces an alternating current, whose amplitude varies according to the amplitude of the acceleration and the frequency of vibration. On the other hand, electronic loads connected at the output require a DC voltage with relatively low amplitude. Thus, two steps of a power conversion are inevitable. The AC/DC rectifier in the first stage (Part I) converts the varying AC output voltage delivered by the PZT bender into a DC output. The DC/DC converter in the second stage (Part II) serves as a step-down of the primary DC voltage to a required output voltage. The principle of the power conversion is depicted in the Figure 23.

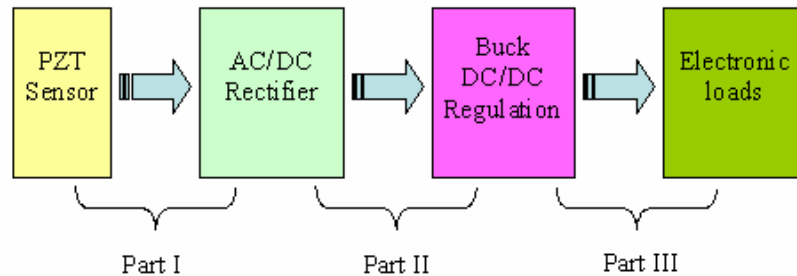


Figure 23: Principle of power conversion

A circuit scheme for the part I is shown in Figure 24, which is an uncontrolled rectifier consisting of diodes in a bridge configuration. Since we need the maximum power from PZT, uncontrolled rectifier is preferred in this design. The magnitude and frequency of input voltage for the rectifier varies in a wide range dependent upon the

acceleration imposed to the bender. Therefore, a DC/DC converter is required to get stable DC output. However, the DC voltage generally includes voltage ripples that fluctuates a twice higher than the frequency of the AC input voltage. The ripples can be further reduced when a capacitor is connected in parallel to loads. However, the voltage at capacitor can exceed a limit given by input voltage of the following DC/DC converter. Fortunately, the DC/DC presents a continuous load that is applied to the DC voltage. Countermeasure will be the use of an additional Zener diode that clamps potential over-voltage at the input of the DC/DC converter that can be generated by the PZT bender.

Under consideration of the voltage generation of the PZT bender, and the load profile requirement that the output voltage should be 3.3V, the converted AC voltage should be stepped down (Buck) converter as the part II represents. Generally, the ratio of the converting voltage between the input and output is less than 3, so the proper selection of the topology should be taken into account for an optimal design of the circuit. In addition, efficiency is one of important criteria. If the efficiency is low, the power can be only consumed by operating the DC/DC circuit and no power can be transformed to the actual load.

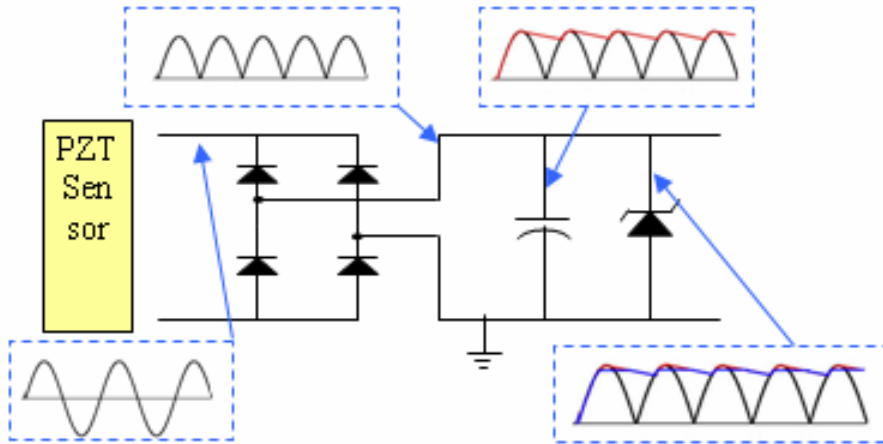


Figure 24: Circuit Diagram for the Part I

One possible choice for the DC/DC converter is MAX640 manufactured by Maxim Integrated Products. According to the data sheet provided by the manufacturer, the efficiency can reach up to 95% under no load condition.

### 5.1 Load requirement

The wireless transmitter requires a discontinuous power, which is depicted in Figure 25. The load draws 12mA during 200ms over a five seconds period and the output voltage should not drop lower than 2.4 to ensure its functionality. Therefore, the output capacitor has to be carefully selected to satisfy the requirements.

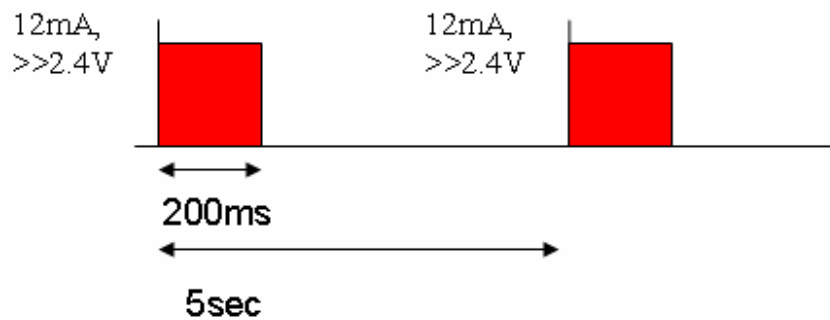


Figure 25: Load requirement

A more detailed circuit block diagram is shown in the Figure 26, where the load is assumed to be connected in series with a switch that periodically turns on and off the load.

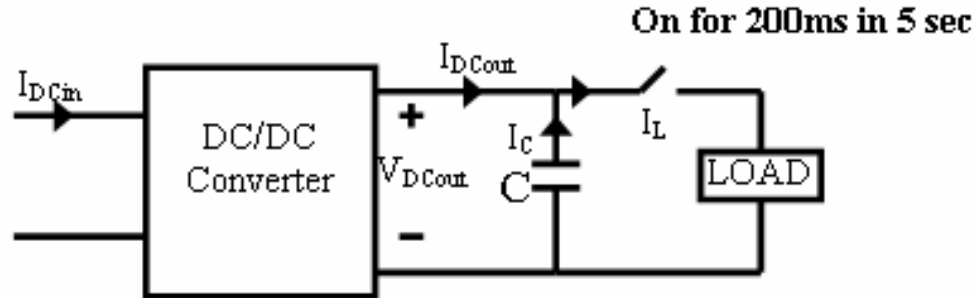


Figure 26: Load with ideal switch

## 5.2 Circuit Scheme

As discussed previously, two steps of power conversion are implemented by two integrated circuits. The bridge rectifier BGX50 converts the AC power generated by the PZT into the DC power, and then the MAX640 does the DC voltage into a DC voltage required. The schematic diagram of the circuit is shown in Figure 27.

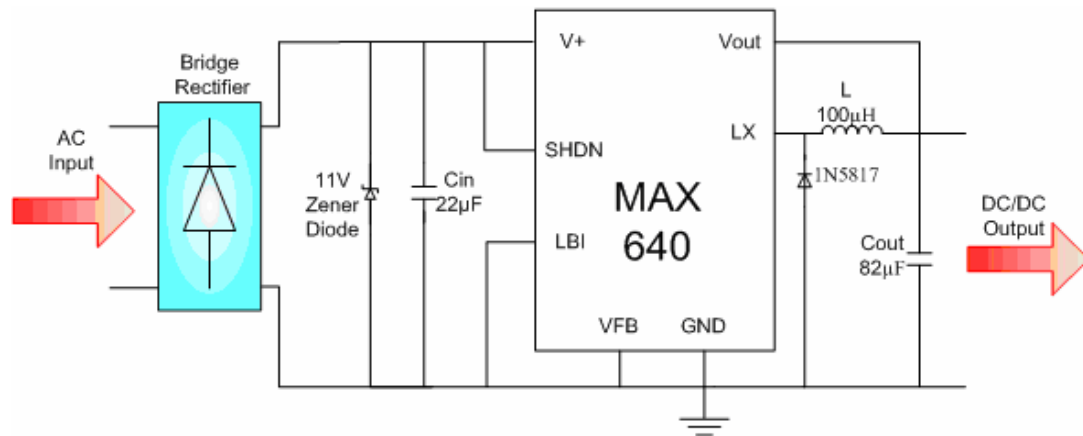


Figure 27: Circuit scheme

## 5.3 Load Tester

### 5.3.1 Circuit Design

To ensure the power conversion circuit can work with the real load supplying power for a wireless circuit, a load tester is designed to emulate the load behavior. The tester is based on a 555 timer that serves to produce a short pulse in a specified time interval and an N-Channel MOSFET that turns on a load. Since the duty circle of the 555 timer has to be greater than 50%, an extra logic inverter is connected at the output of the 555 timer. The detailed circuit is shown in Figure 28.

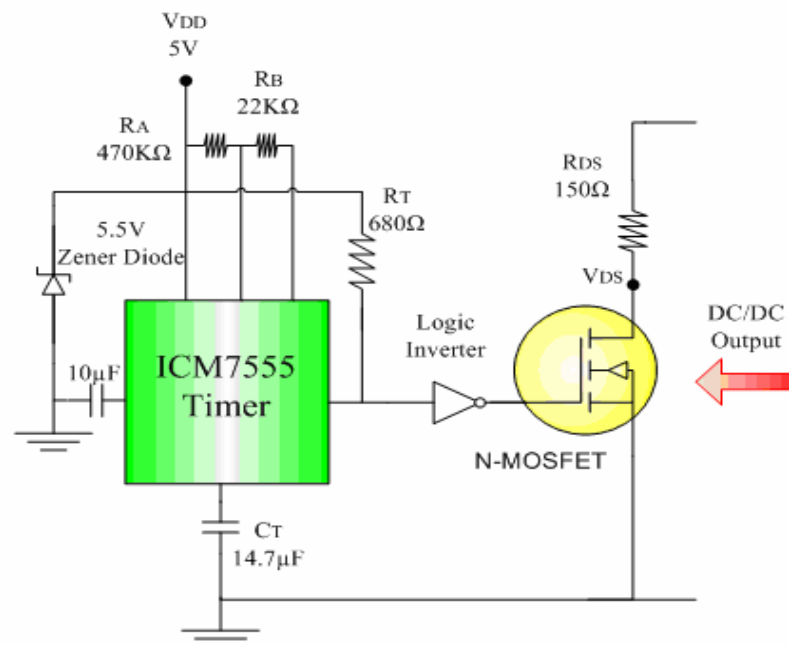


Figure 28: Load tester circuit layout

The device constructed on a printed circuit board is shown in Figure 29.

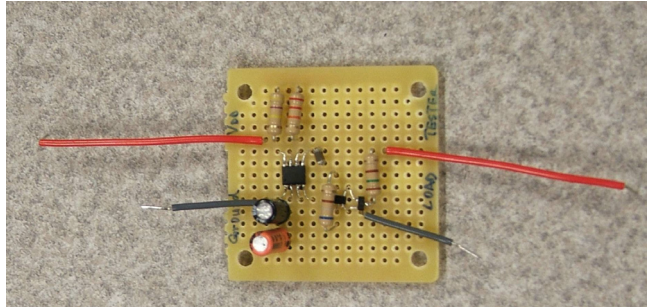


Figure 29: Load tester

The load tester is now connected with the power conversion circuit as a load, as shown in Figure 30. The output of the function generator is set to a 16V (peak-to-peak) sinusoidal wave with a frequency of 100Hz.

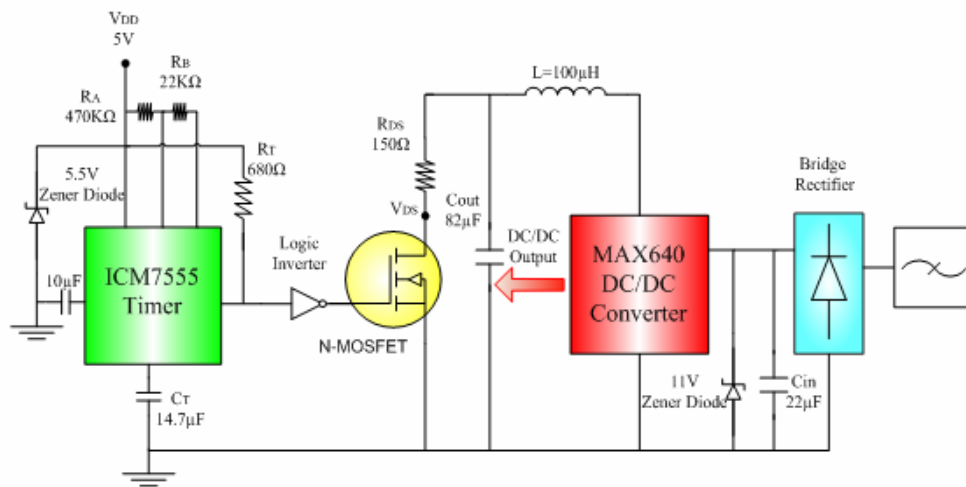


Figure 30: Power Conversion Circuit with Load Tester

## 6 Results and Discussion

### 6.1 Results for Room Temperature Measurements

The cantilever designed is excited by a shaker connected to a function generator via an amplifier. Three cases have been studied with an open circuit, a resistive load without and with a rectifier with a capacitor.

Figure 31 shows a Fast Fourier Transform (FFT) analysis for the PZT bender, where the exciting frequency is changed. The first mode of the resonance frequency appears at 97.6 Hz and the second mode of the resonance frequency is captured at 650 Hz. However, the amplitude for the second mode is negligible as compared to the fundamental mode. As a result, this frequency hardly contributes the energy harvesting or damages the structure of the beam.



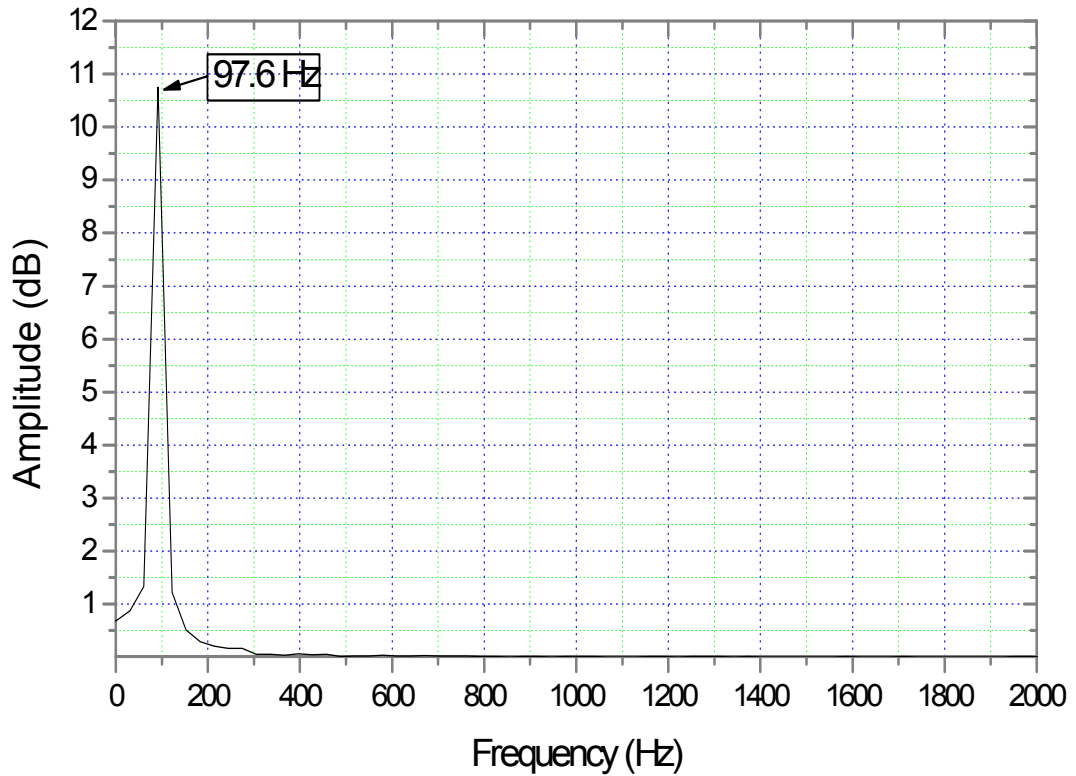


Figure 31: FFT analysis of experimental results for frequency response

**Table 3** shows the first mode of the resonance frequency for experiments, Ansys and three analytical models. The comparison reveals that there is slight mismatch between the experimental and the simulated frequency for electrical equivalent circuit model (model 1) and model based on conservation of energy principle (model 2), but shows a good match between the couple field model (model 3) and experiments and Ansys simulation.

Table 3: The first mode of the resonance frequency for the PZT bender

Model	Resonance frequency (Hz)
Experimental	95
Ansys	93.27
Model 1	85.9
Model 2	86.9
Model 3	94

### 6.1.1 Ansys modeling

The device structure was modeled in Ansys with solid modeling. The solid model was created in Ansys first using the batch file input method. This method is preferred because it is easier to model different device geometry. The device was modeled as 3 layer structure with a proof mass. 3D elastic beam element was chosen for the PZT and brass material and solid45 element was used for the proof mass. The meshing was done with tet mesh option in Ansys for the PZT, brass and the proof mass for easy meshing. The boundary conditions applied to the clamped end of the structure by applying zero displacement for all DOF at the nodes. Modal analysis type was selected to determine the resonance frequencies for the first five modes for the structure. The Subspace Method was used to extract modes for all DOF's. It is more exact as compared to the reduced order method but, it also takes longer to compute. The resonance frequencies for the first 5 modes are tabulated in Table 4.

Table 4: The first 5 mode of the resonance frequency for the PZT bender

Mode	Frequency
First	93.272
Second	612.89
Third	1055.6
Fourth	1598.2
Fifth	2947.4

Figure 32 -Figure 36 below shows the first five modes from Ansys simulation.

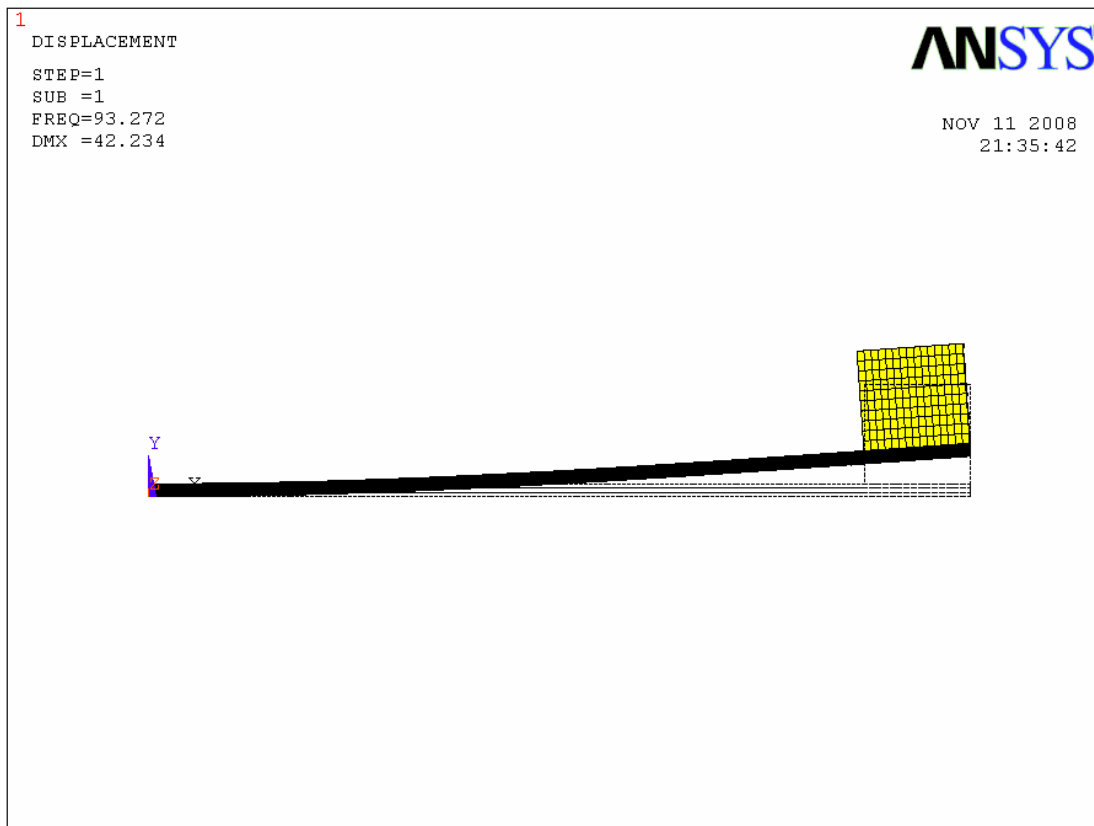


Figure 32: First mode of resonance from Ansys

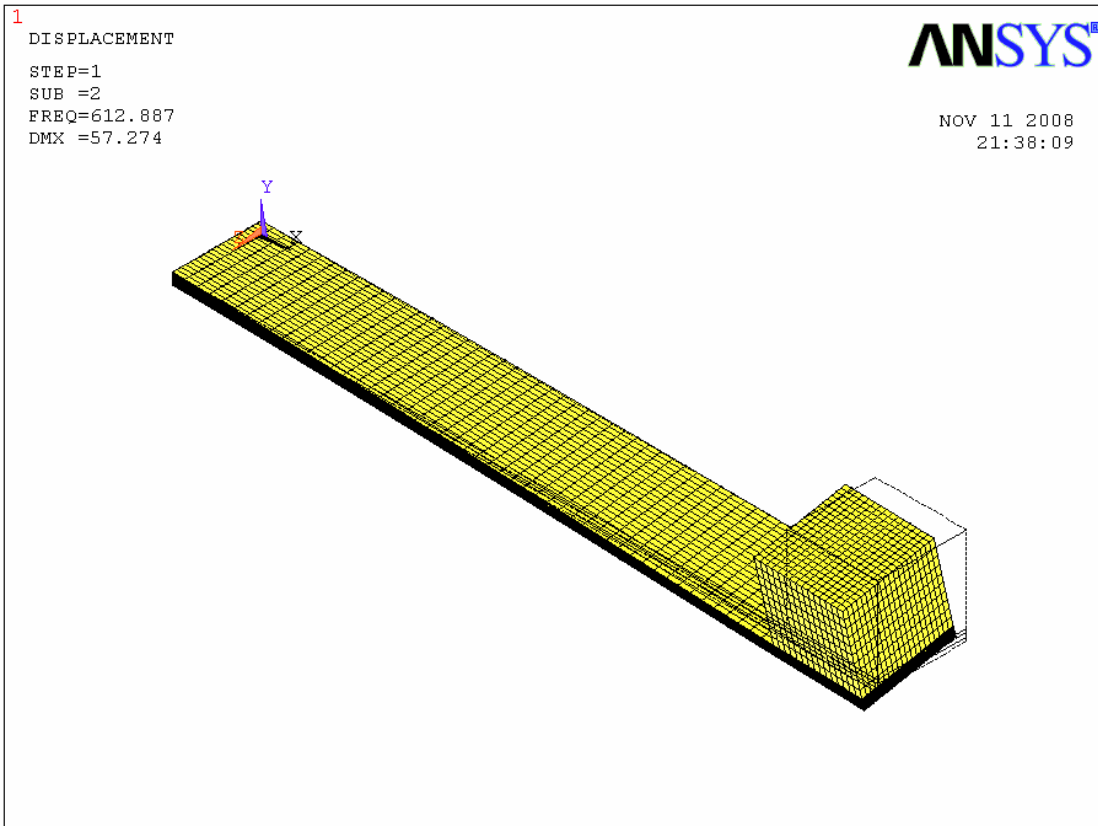


Figure 33: Second mode of resonance from Ansys

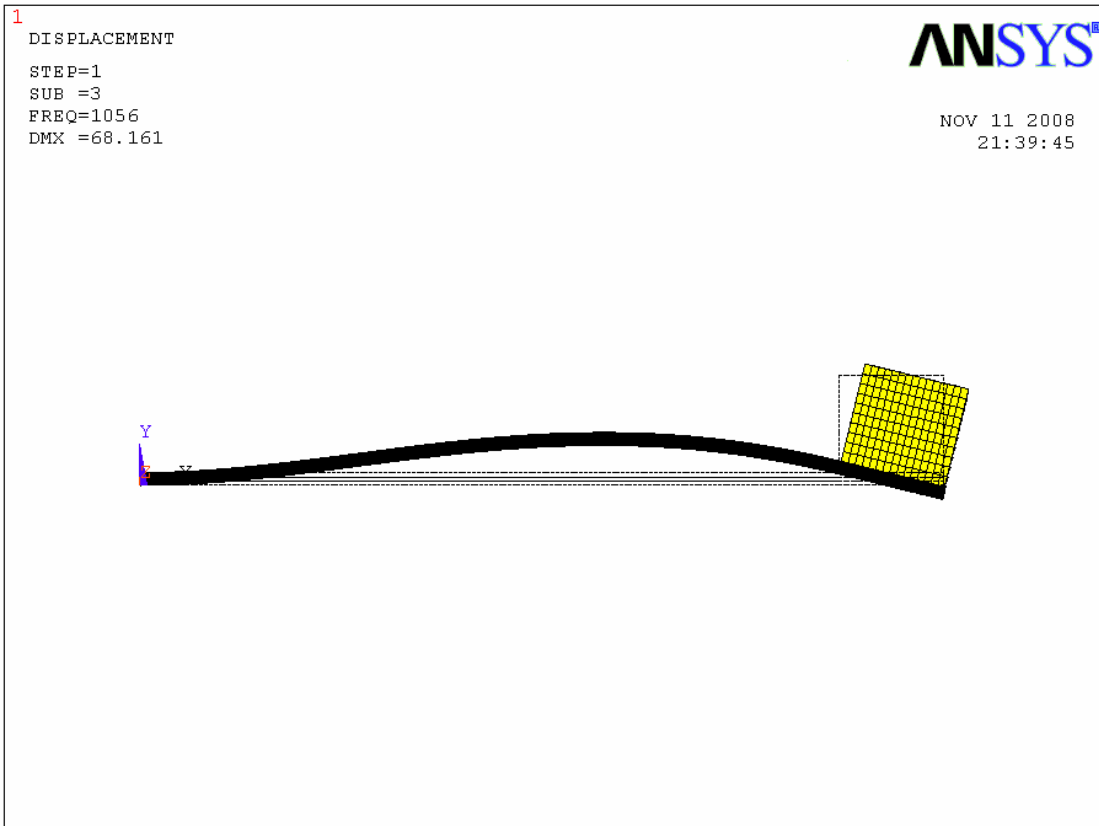


Figure 34: Third mode of resonance from Ansys

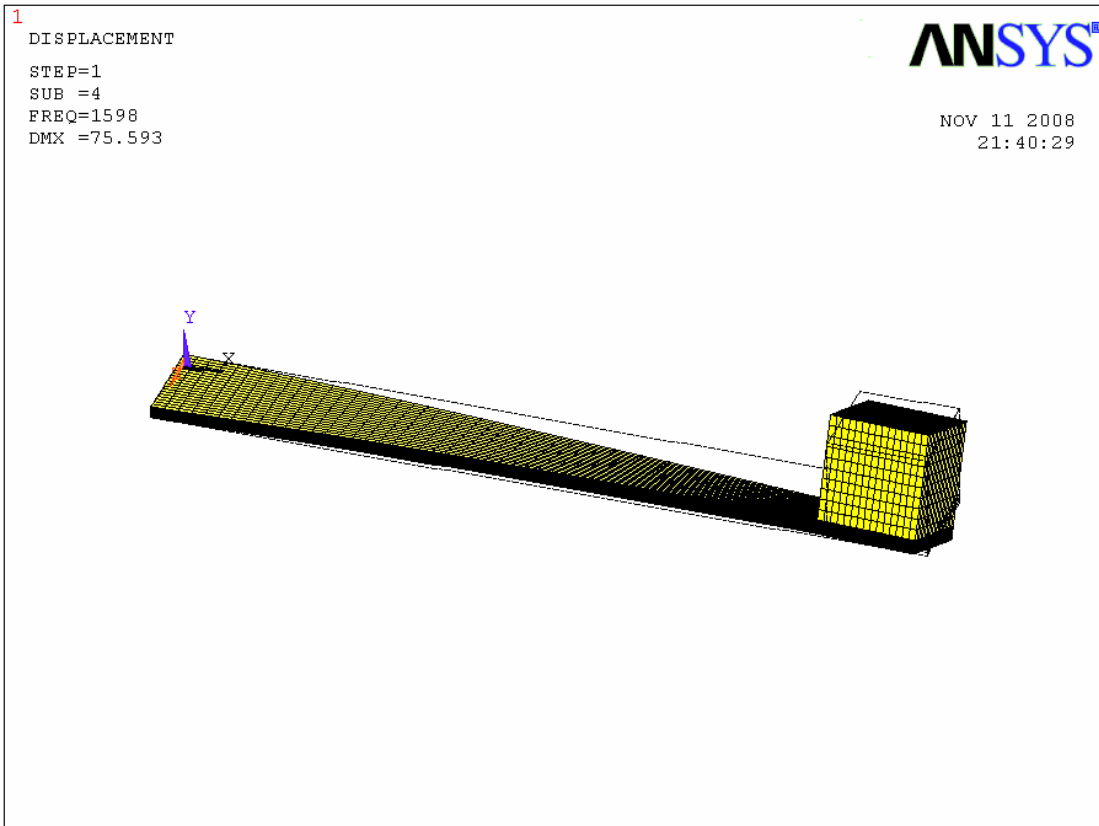


Figure 35: Fourth mode of resonance from Ansys

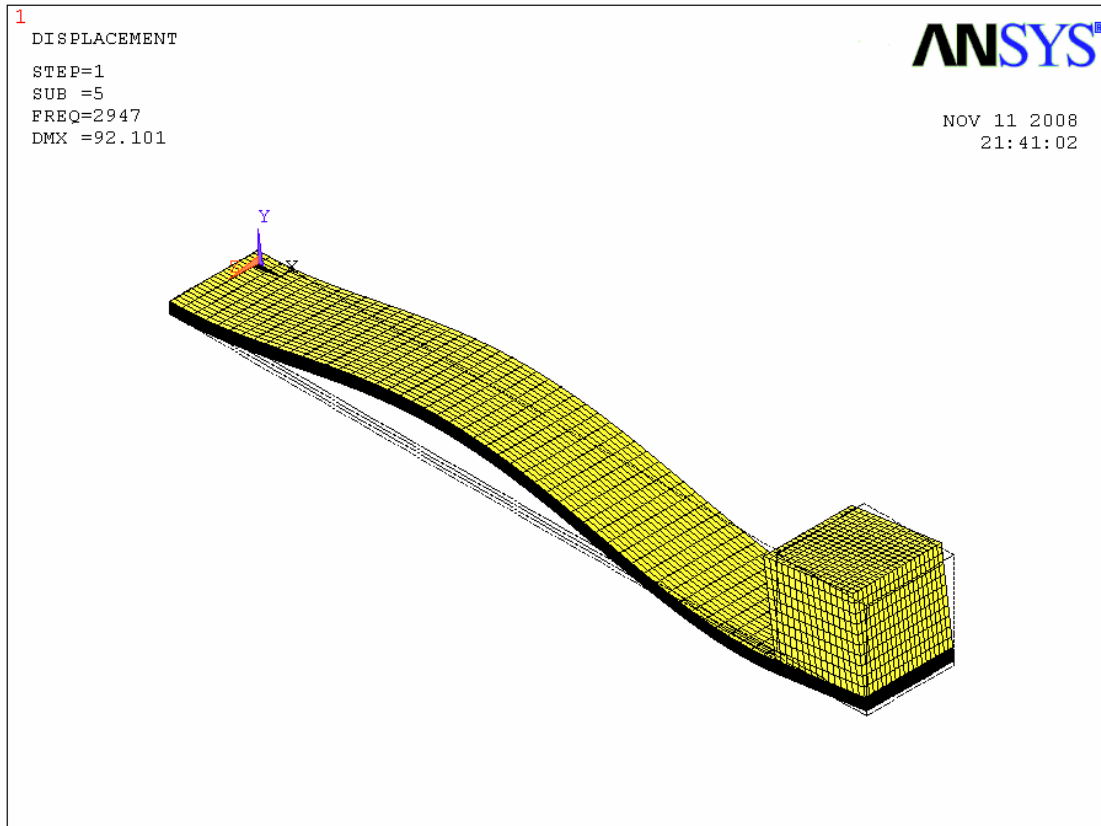


Figure 36: Fifth mode of resonance from Ansys

Figure 37 shows the first experimental result, where the beam is excited with an input sinusoidal acceleration with amplitude of 1-g and frequency of 95 Hz and the voltage at the output is measured. The peak value of the output has been reached to 11.49 volts at amplitude of the acceleration with 1-g ( $9.8 \text{ m/s}^2$ ).

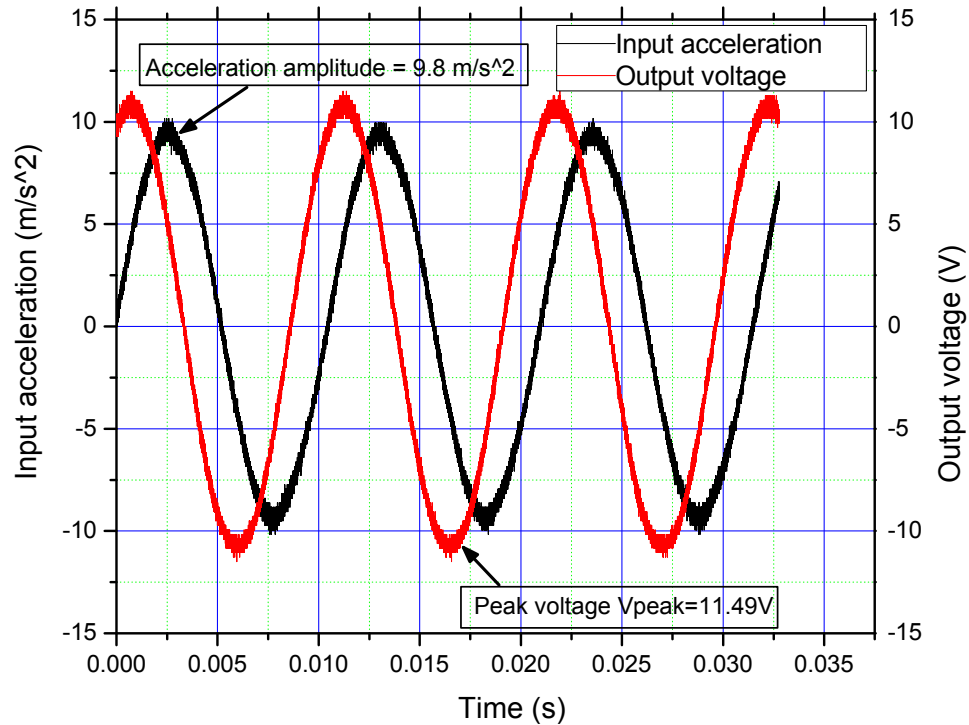


Figure 37: Experimental results for the open circuit AC voltage and input acceleration

### 6.1.2 Open Circuit Results

Figure 38 shows the waveforms of the output voltage for the experimental and the simulated. Comparisons of both results reveal two major discrepancies in the amplitude and the phase. Firstly, the peak amplitude of the AC voltages simulated for three models are different than the experiment result. The experimental results show 11.49V, while the models do 10.47V, 11.649V and 10.254V. Secondly, it has been observed that the phase displacements are different. The experimental results shows a phase shift of  $52^\circ$  between the input acceleration and the output voltage, while the first model shows the voltage and input acceleration to be in phase, the second model predicts the phase difference of  $62^\circ$



and the third model predicts the value to be around  $125^\circ$ . Among three models, the second one based on the principle of the energy conservation accomplished the best result.

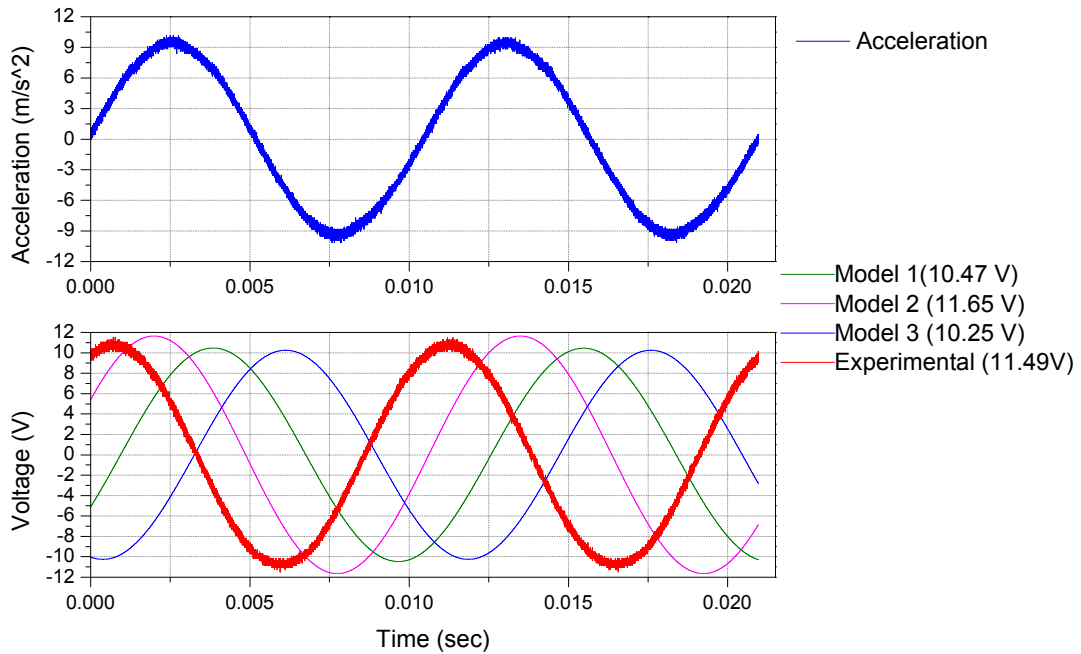


Figure 38: Comparison of amplitude of the open circuit AC voltage for three models with experimental results

### 6.1.3 Resistive Load without a rectifier

Figure 39 and Figure 40 show the output waveform of the PZT power generator measured and simulated, where a  $4k\Omega$  resistor is connected as a load. The peak voltage measured amounts to  $0.58V$ , while the simulated are  $0.521V$ ,  $0.713V$  and  $0.553V$  respectively for the three models. However, the third model accomplished the least discrepancy compared to the experimental.

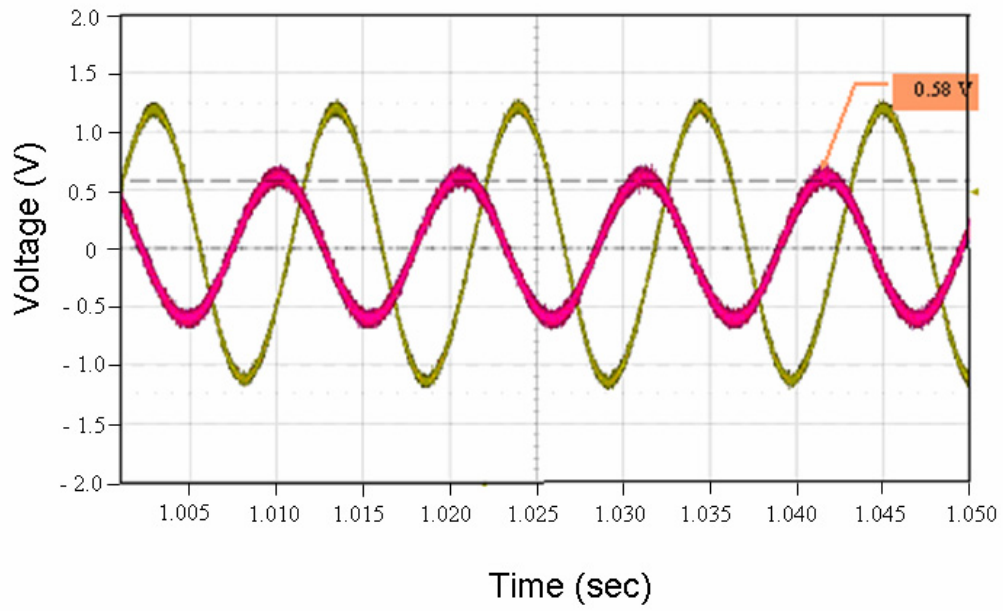


Figure 39: Experimental result for the output voltage with a 4 k $\Omega$  resistive load

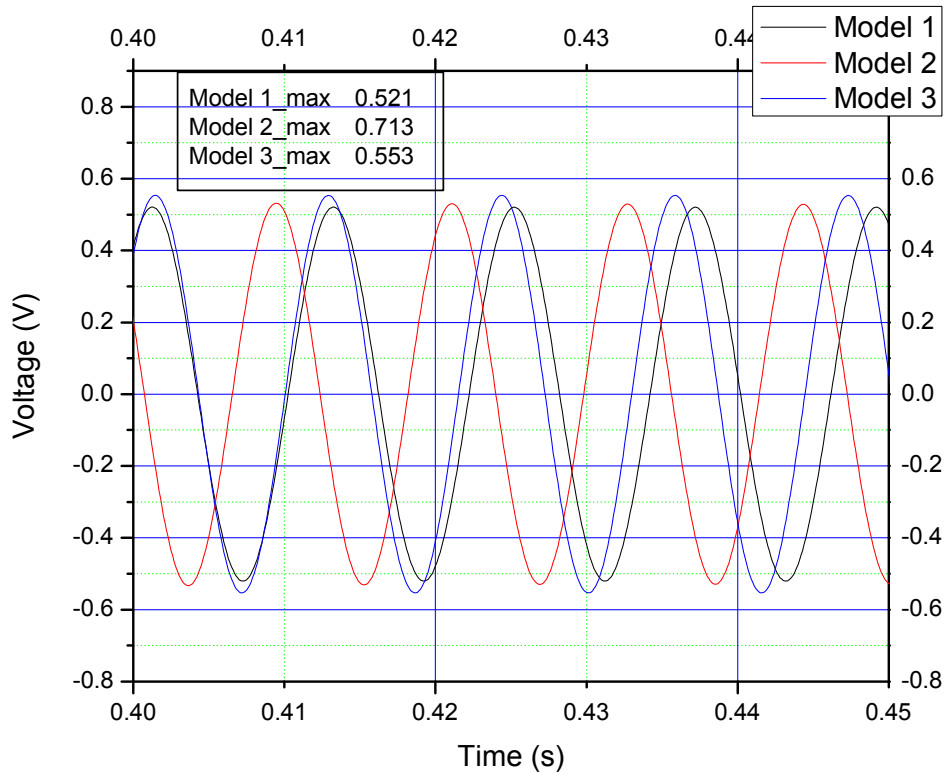


Figure 40: Simulation results for the output voltage with a 4k $\Omega$  resistive load

When the value of the resistor increases, the current drawn from the PZT beam gets decreased. As a result, the voltage supplied increases again. Figure 41 shows I-V characteristic of the bender for different resistive loads. The charge generated at a constant acceleration decreases when the current increases. This I-V curve plays a significant role in selecting topology and at the same time sizing components. The maximum power of the device produced amounts to 250( $\mu$ W) approximately at a value of the load resistance between 100k $\Omega$  and 80k $\Omega$ . The device is comparable to a voltage source with an internal resistance, which value is identical with the value of the load resistor at the maximum power.

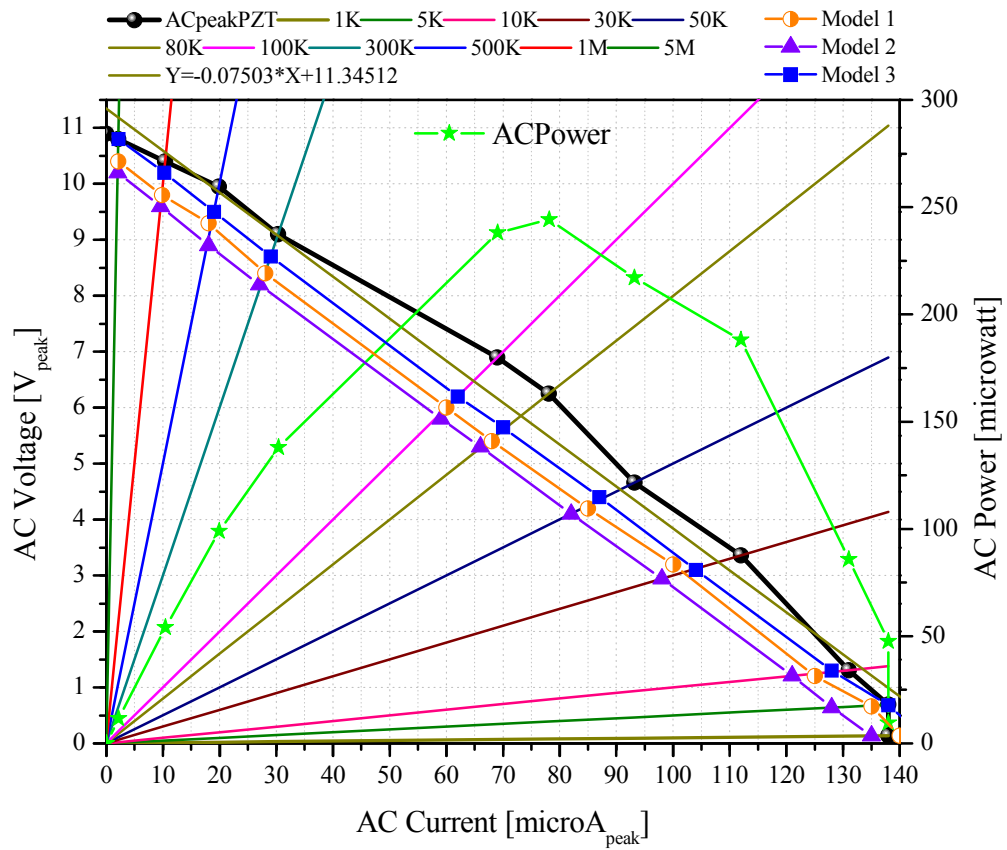


Figure 41: I-V characteristics of the PZT bender without rectifier circuit

#### 6.1.4 Resistive load with a rectifier

Figure 42 shows the waveform of the voltages before and after the rectifier for a 400 kΩ resistive load. The DC voltage amounts to 7.35 V and the AC voltage ripples are well suppressed.

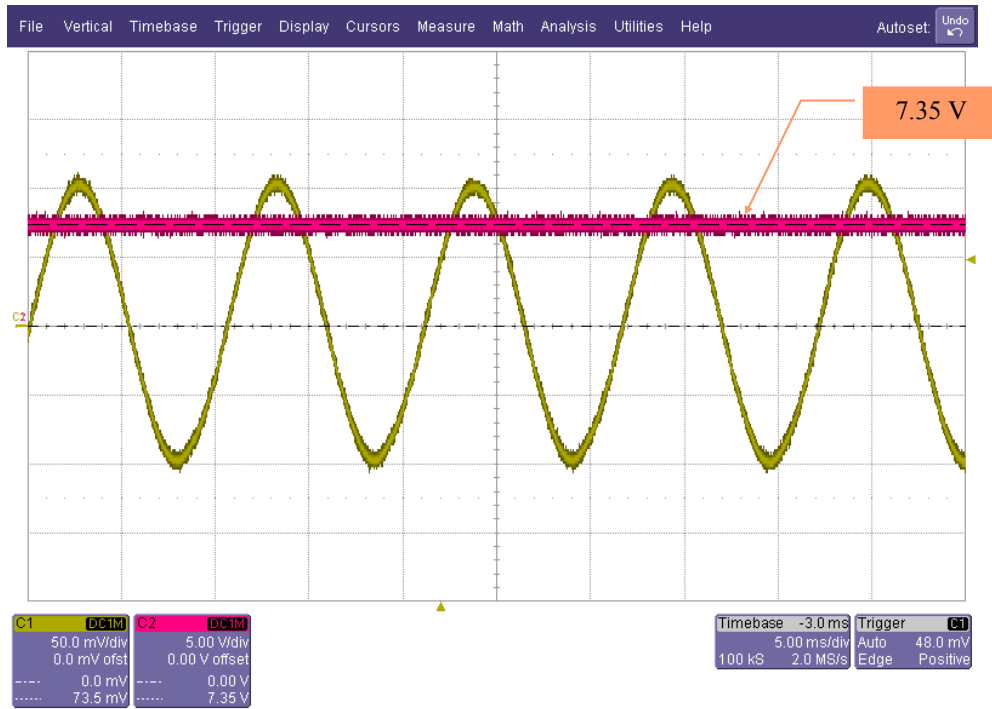


Figure 42: DC voltage at a 400 k $\Omega$  resistive load

Figure 43 shows simulated results for AC voltage and AC current, and DC voltage at an excitation of the device. It is noted that the AC voltage clamps whenever the current starts to flow. The physical reasons are not clear, but it can be interpreted that a voltage drop at the internal resistance drastically increases as soon as a current flows. It is noted that the current charging the DC capacitor is not sinusoidal and the influence of the current has been worsened at a resistive load with a rectifier compared to the previous case.

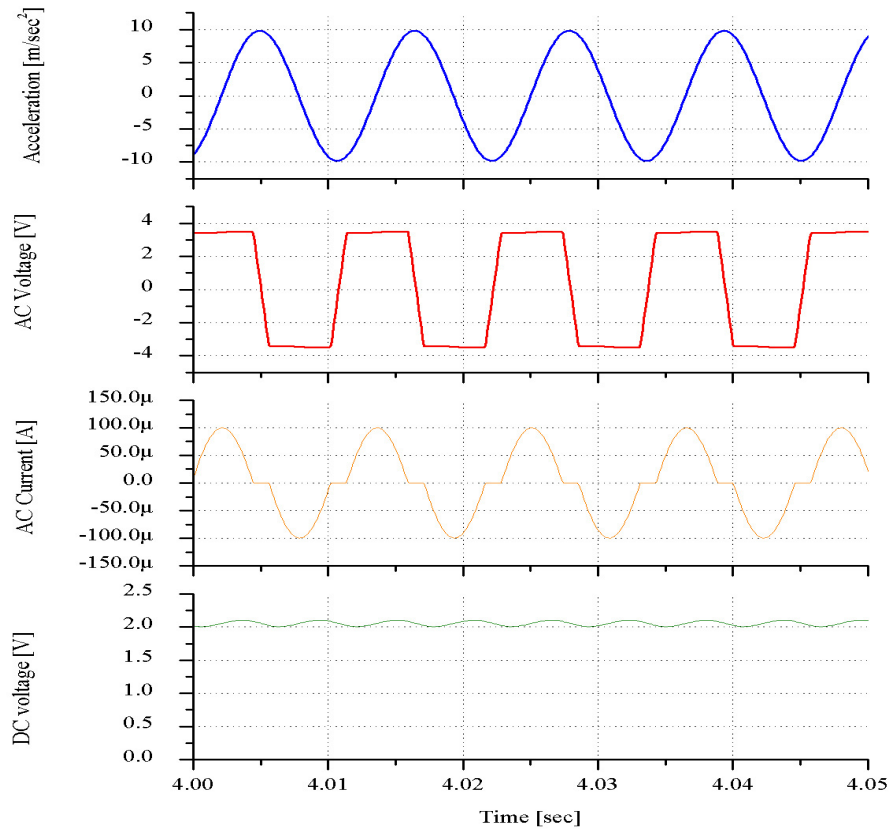


Figure 43: AC voltage and current, and DC voltage at a 40kΩ resistive load with a rectifier

Figure 44 shows the I-V characteristic measured and simulated at the DC side. The maximum power has been reached around at the 100 kΩ. The amplitude of the voltage becomes less because of the voltage drop at two diodes and the internal resistor and clamping behavior of the device.

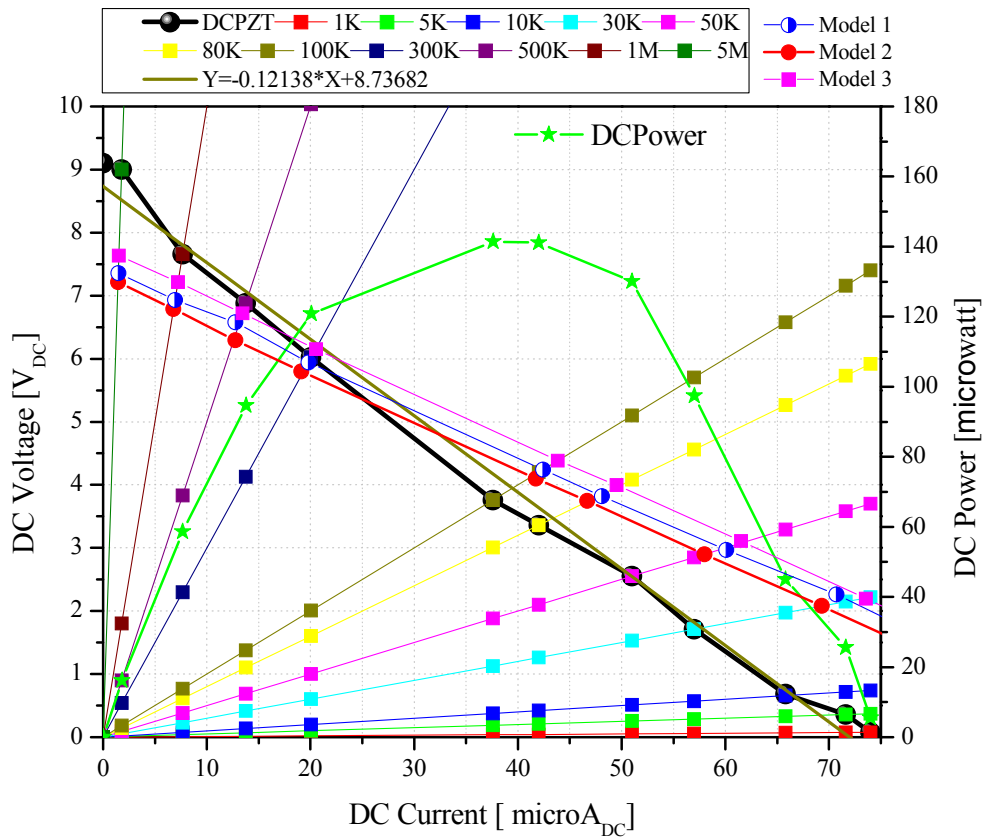


Figure 44: I-V characteristics of the PZT bender with rectifier

Figure 45 shows three lines with different slopes of I-V characteristics. The first one with the red color presents the characteristic of the AC voltage source, while the second one with the blue color does the characteristic of the DC voltage source. The third one indicates a voltage characteristic that includes a voltage drop at the diodes and fictitious internal resistor. According to the evaluation, however, it is observed that the slopes indicating the voltage drop is not identical with the characteristics of AC voltage source as the load current increases. At this moment, the physical reasons for this voltage drops is not clear. Overall mismatch between the simulated and the measured requires further investigations on the device and the circuit. It is obvious that the models describing the

mechanism are not sufficient enough to reproduce the real behavior of the device. Consequently, it is necessary to develop a high fidelity model that helps understand the physics of the PZT material in conjunction with a structure and power conversion circuit, and facilitates an optimal design of a power harvesting PZT system.

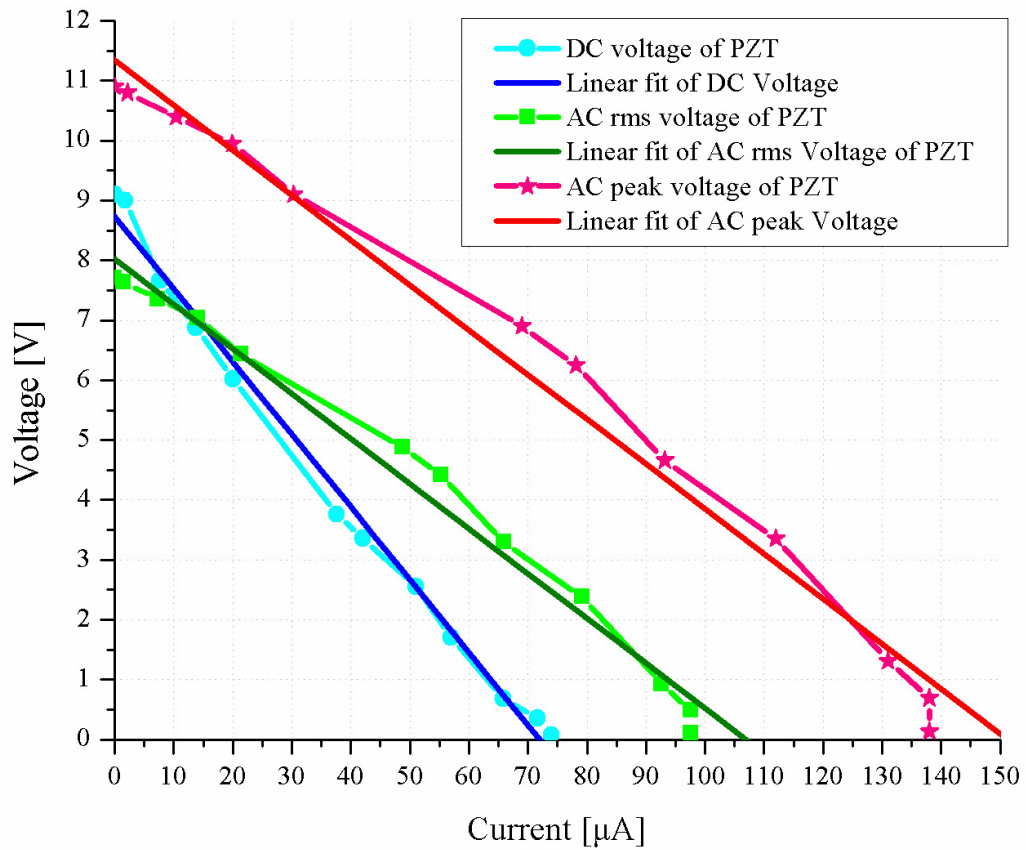


Figure 45: Comparison and evaluation of AC and DC I-V characteristics



## 6.1.5 Coupled-field model results

### 6.1.5.1 Open Circuit

The accuracy of the model was compared with respect to the time response at an acceleration of the device and the current-voltage characterization as well as the generated power at different resistive load. Experimental data was available for the device being modeled. That data included a device natural frequency of 95Hz and power and voltage data for different load resistances. The Raleigh-Ritz method used to determine the lumped parameters provided mass and spring coefficients of;  $m=0.502\text{grams}$  and  $k=289.02\text{ N/m}$  ( $f_0=94\text{ Hz}$ ). The damping coefficient was assumed to be;  $c=0.02\text{ kg/s}$  for all cases.

Figure 46 shows the comparison of experimental vs. simulation results for open circuit voltage output from the PZT micropower generator. It can be seen from the Figure 6, that the experimental open circuit output voltage coincides pretty good with the simulation results. The experimental resonant frequency for the structure is 95 Hz, while the simulation resonant frequency is 94 Hz. The maximum experimental voltage was  $\sim 22\text{V}$  (peak to peak) at  $\sim 95\text{Hz}$ , which matches the state-space model well, where the maximum voltage (open loop) was  $\sim 23\text{V}$  (peak-peak), at  $\sim 94\text{ Hz}$ .

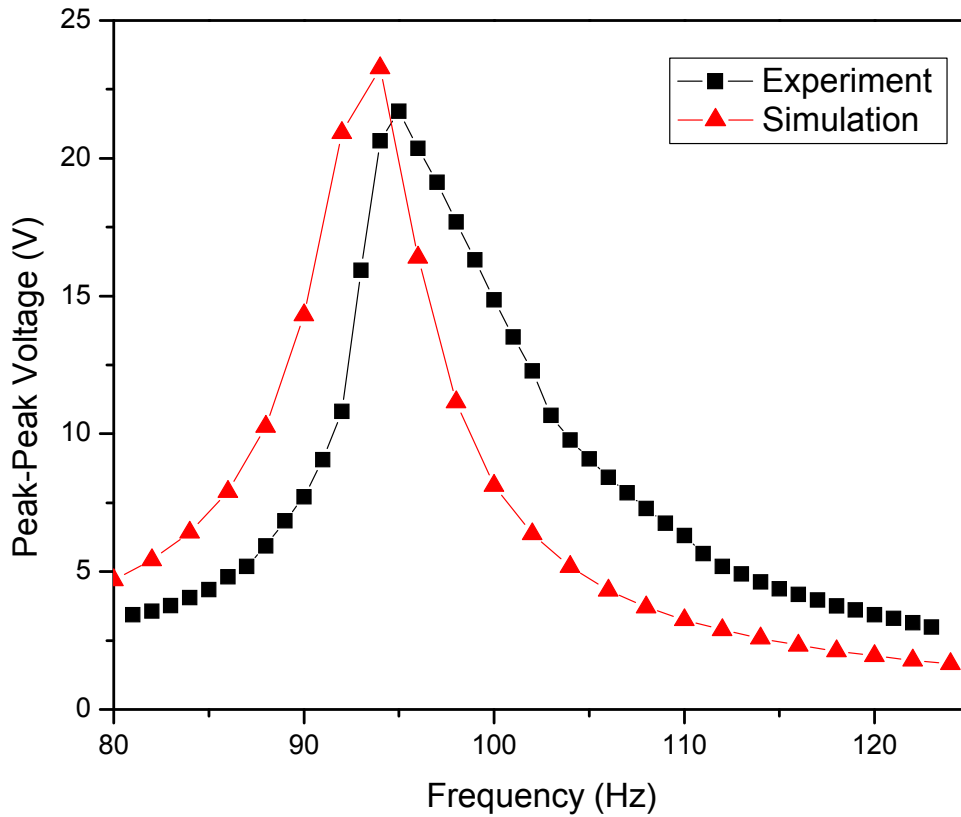


Figure 46: Comparison of experimental vs. simulation results for frequency vs. voltage output.

#### 6.1.5.2 Resistive load

Figure 47 shows the trend in output voltage and active power for the PZT micropower generator at resonant frequency with different load resistance, which also coincides with the simulation data pretty well. Although there is slight discrepancy in the optimal load resistance for the experimental and simulation results, for the model, the load and frequency at max power was  $\sim 70\text{k}\Omega$  at  $\sim 94\text{ Hz}$  while the experimental data has load and frequency at max power of  $\sim 80\text{k}\Omega$  at  $\sim 95\text{ Hz}$ .

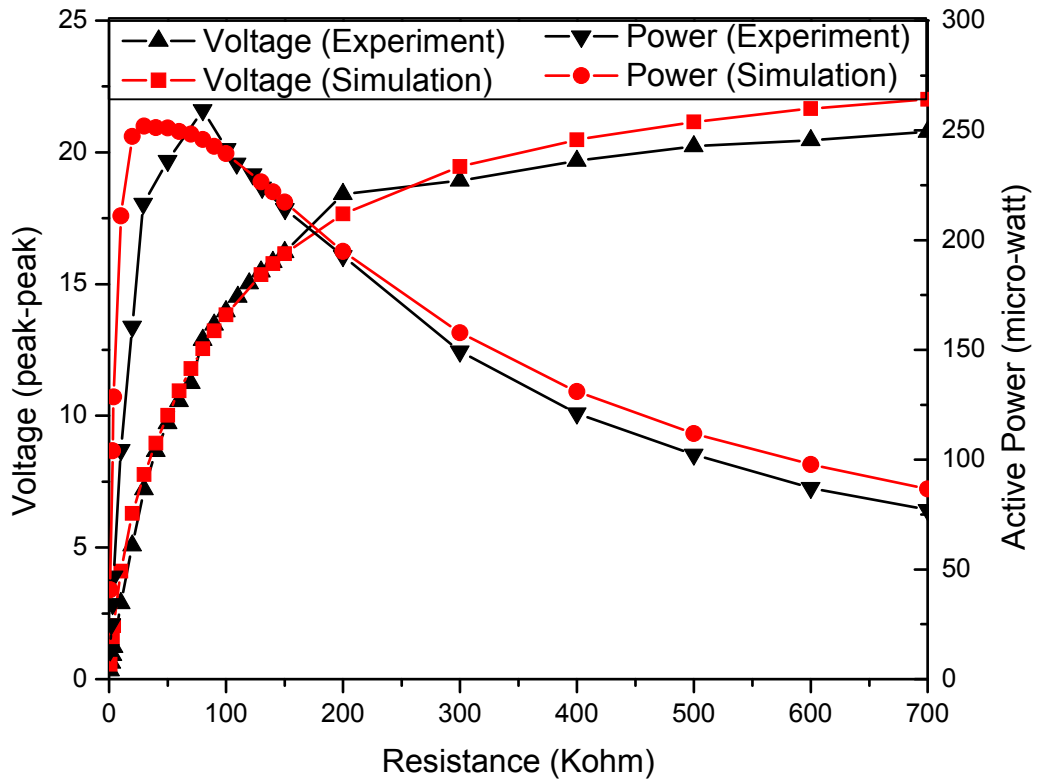


Figure 47: Comparison of experimental vs. simulation results for voltage vs. load resistance.

Figure 48 shows the I-V characteristics of the PZT micropower generator. The maximum voltage was  $\sim 22$ V (peak to peak), the maximum power was  $\sim 250\mu$ W. This matches the state-space model well, where the maximum voltage (open loop) was  $\sim 23$ V (peak), and the maximum power was  $\sim 240\mu$ W.

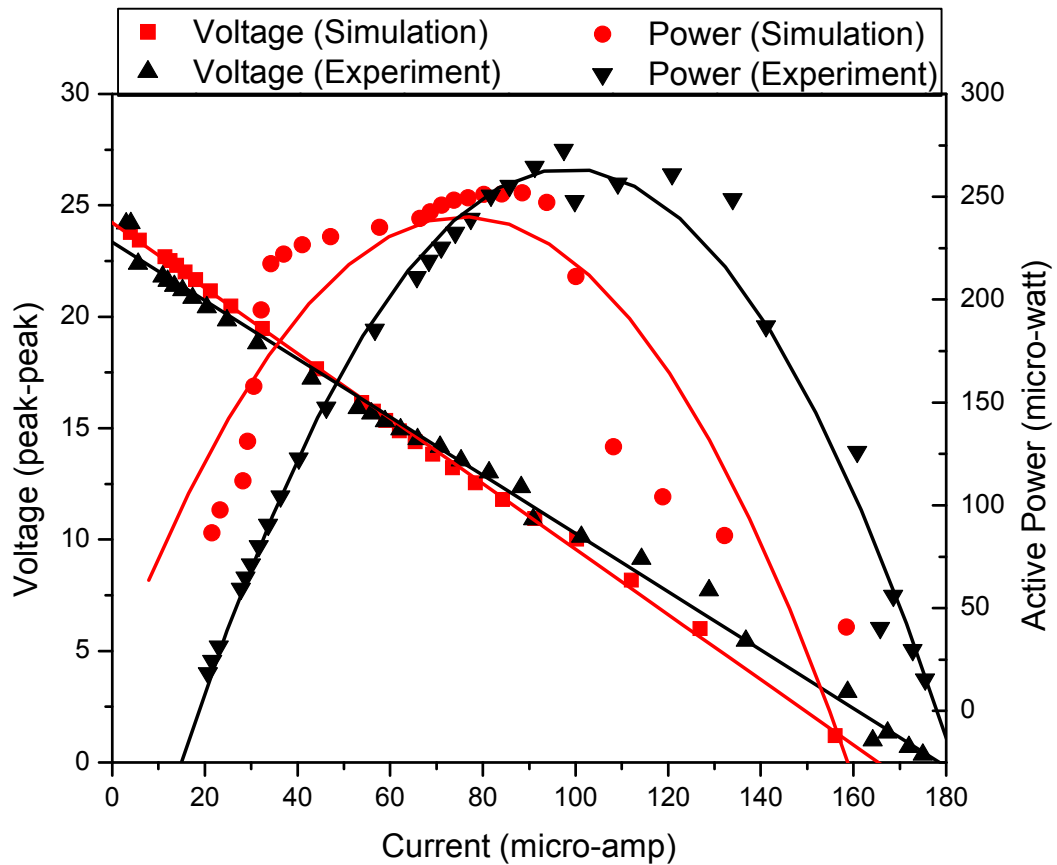


Figure 48: Comparison of experimental vs. simulation I-V characteristics

### 6.1.5.3 Rectifier with resistive load

The PZT bender produces an alternating current, whose amplitude varies according to the amplitude of the acceleration and the frequency of vibration. On the other hand, electronic loads connected at the output require a DC voltage with relatively low amplitude. The AC/DC rectifier in the first stage converts the varying AC output voltage delivered by the PZT bender into a DC output. A schematic for the AC/DC rectifier equivalent circuit diagram is illustrated in Figure 49, which is an uncontrolled

rectifier consisting of diodes in a bridge configuration. Since we need the maximum power from PZT, uncontrolled rectifier is preferred in this design.

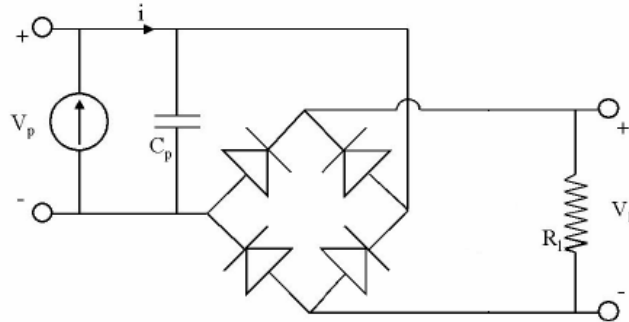


Figure 49: Equivalent circuit for system with rectifier and load resistance

Characterization of the power conversion circuits are conveyed with the PZT micropower generator device. Firstly, the power source is connected with a resistor bank that allows for setting different values of a resistor. After a resistance is set, the voltage at the resistor is measured. The voltage versus current characteristic is obtained when the measure points are connected. The power is given by a product of the voltage and current. Figure 50 shows the I-V characteristics of the PZT micropower generator with the rectifier circuit and load resistances. The experimental maximum voltage was  $\sim 7V$ , the maximum power was  $\sim 140\mu W$ . This matches the state-space model well, where the maximum voltage was  $\sim 9V$  (peak), and the maximum power was  $\sim 145\mu W$ .

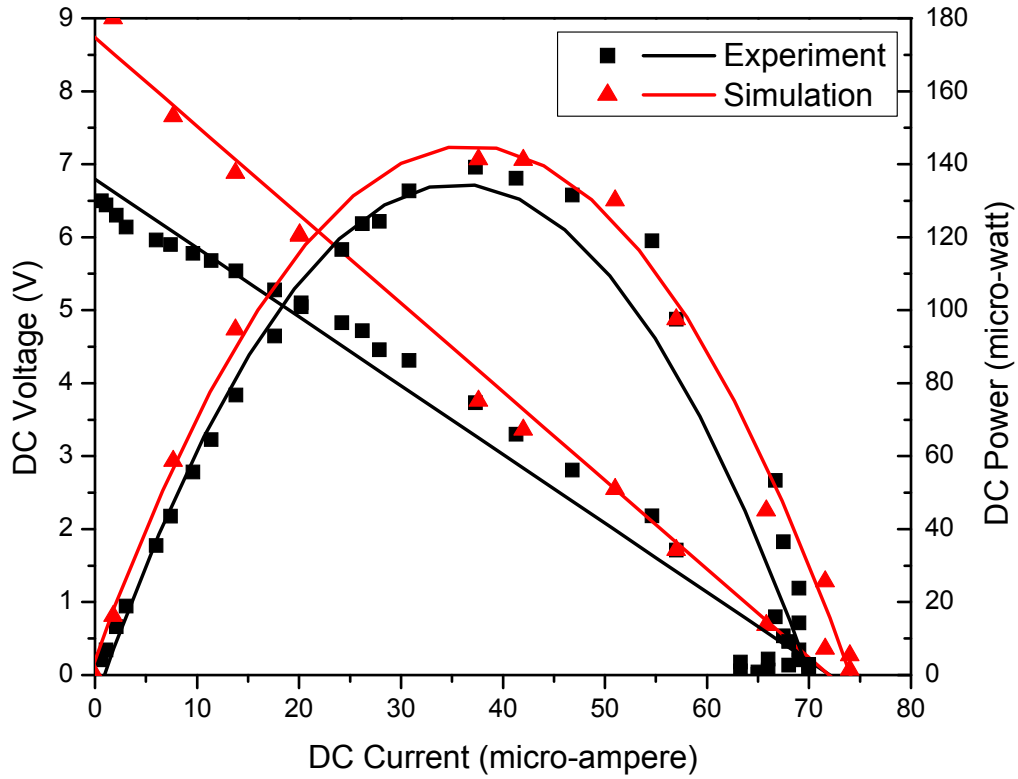


Figure 50: Comparison of experimental vs. simulation DC I-V characteristics

#### 6.1.5.4 Rectifier with resistive load and 22 $\mu$ F capacitor

The PZT bender produces an alternating current, whose amplitude varies according to the amplitude of the acceleration and the frequency of vibration. On the other hand, electronic loads connected at the output require a DC voltage with relatively low amplitude. The AC/DC rectifier in the first stage converts the varying AC output voltage delivered by the PZT bender into a DC output. A schematic for the AC/DC rectifier with a 22  $\mu$ F capacitor is illustrated in Figure 51, which is an uncontrolled

rectifier consisting of diodes in a bridge configuration. Since we need the maximum power from PZT, uncontrolled rectifier is preferred in this design.

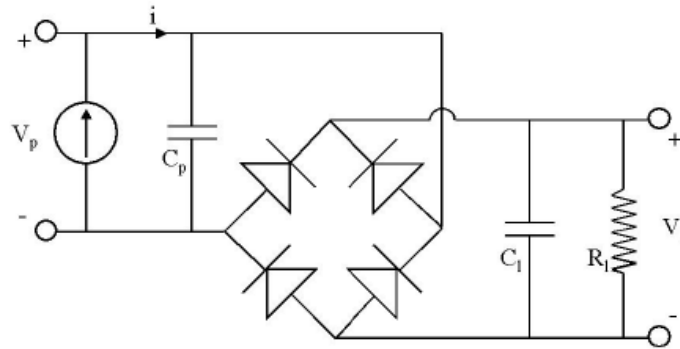


Figure 51: Equivalent circuit for system with rectifier, capacitor and load resistance

Figure 52 shows the I-V characteristics of the PZT micropower generator with the rectifier circuit, 22  $\mu\text{f}$  capacitor and load resistances. The experimental maximum voltage was  $\sim 9\text{V}$ , the maximum power was  $\sim 120\mu\text{W}$ . This however doesn't match very well with the state-space model well, where the maximum voltage was  $\sim 7\text{V}$  (peak), and the maximum power was  $\sim 120\mu\text{W}$ .

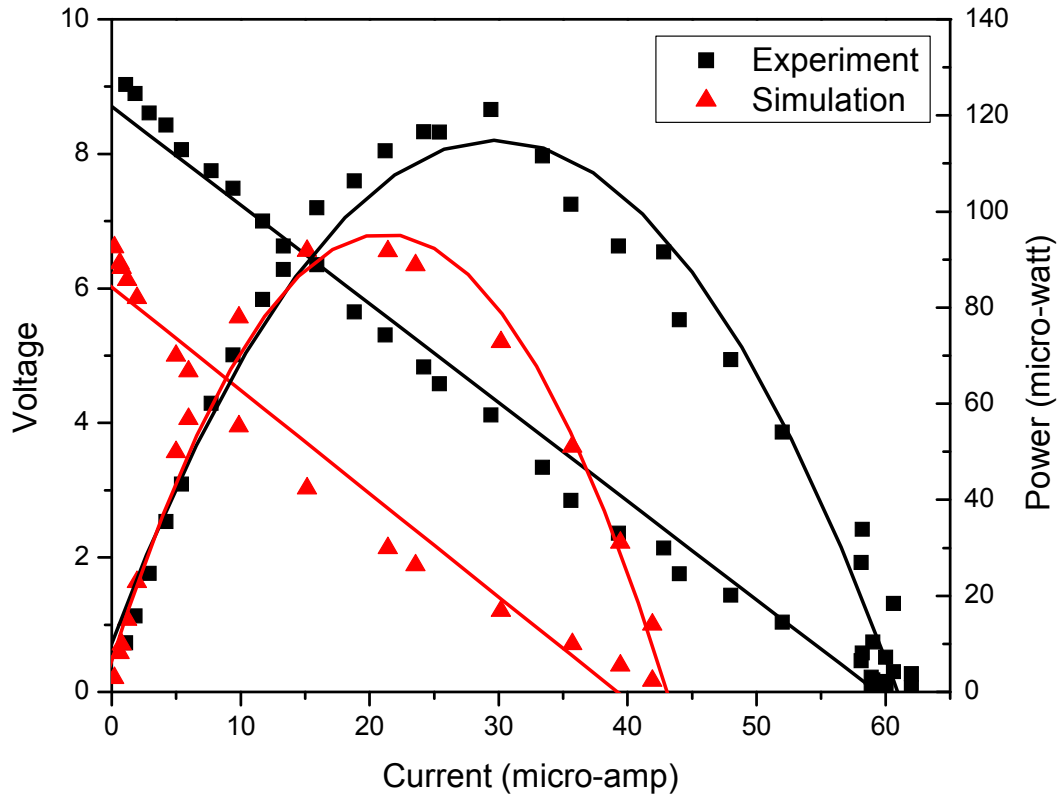
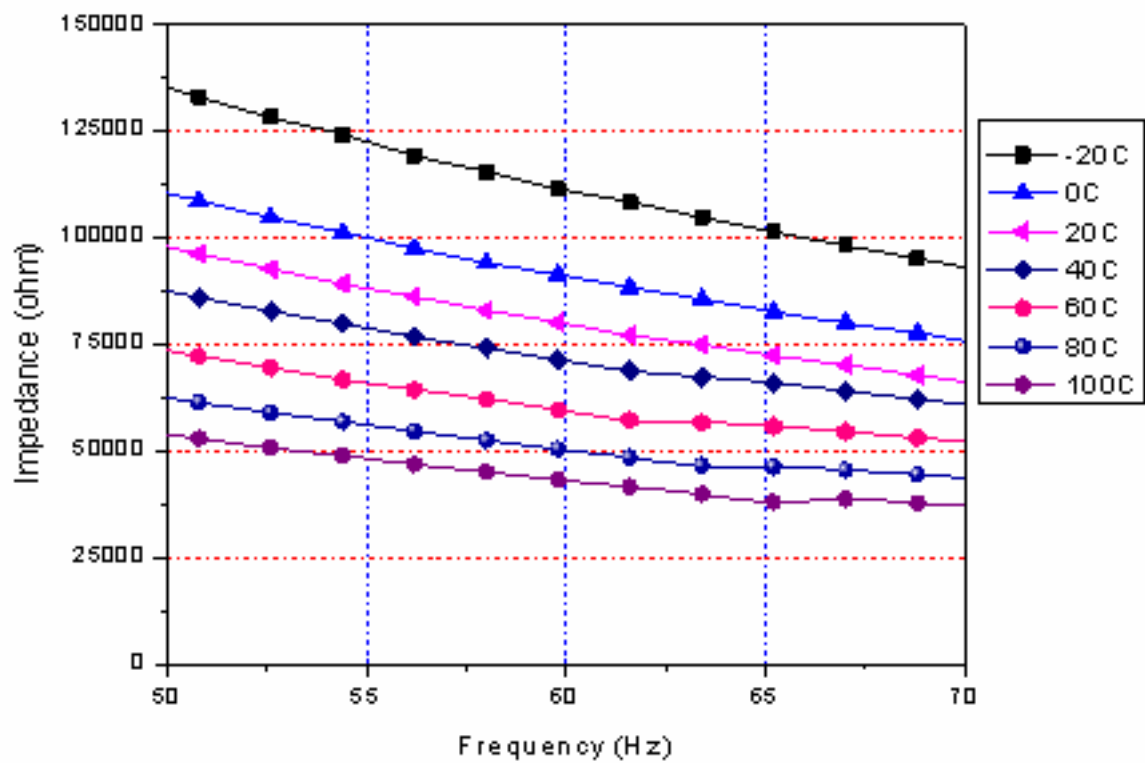


Figure 52: Comparison of experimental vs. simulation DC I-V characteristics

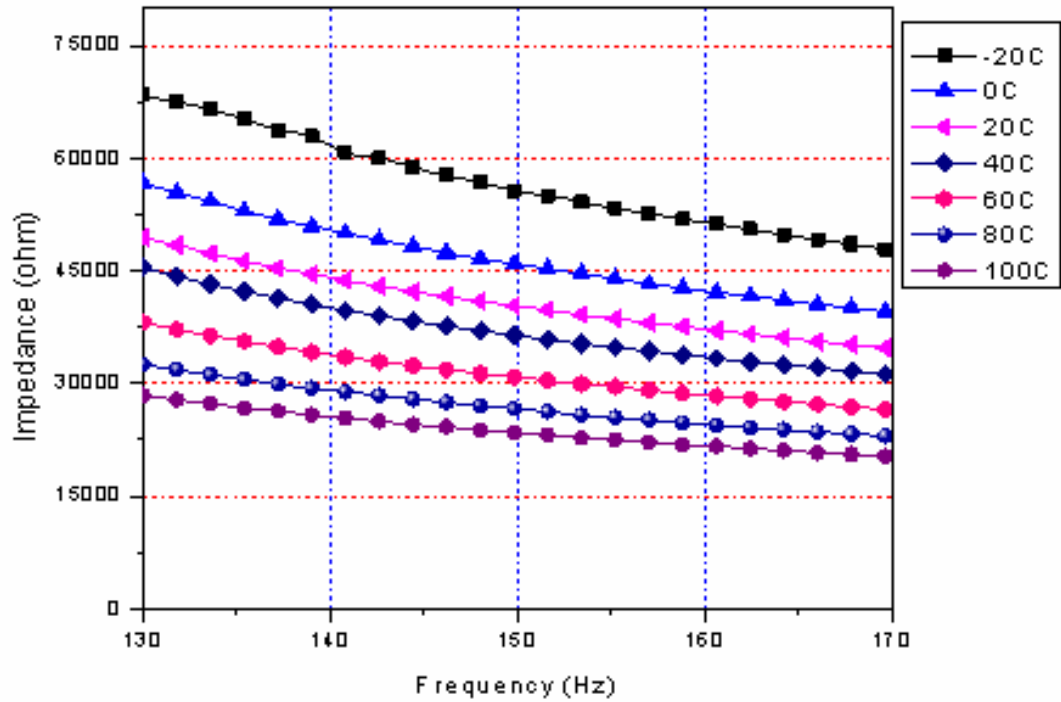
## 6.2 Temperature effect on Impedance

The experiments were performed to measure temperature effects on variation of impedance of the PZT beam to determine the effect on resonant frequency. The measured impedance is graphically presented in Figure 53 at different frequencies. When the temperature rises, the magnitude of the impedance decreases. This baseline shift is due to the temperature dependency of piezoelectric constants as mentioned before. There were no structural resonances of the free PZT existed in these frequency ranges.





a) Lower frequency range



b) Higher frequency range

Figure 53: Temperature effect on the electrical impedance of a PZT

### 6.3 Temperature effect on resonant frequency

Figure 54 shows experimental data for the shift in natural frequency of the PZT cantilever as a function of temperature. The result indicates that an increase in temperature leads to a decrease in resonant frequencies, which is due to the Young's modulus effect. On the other hand, the thermal expansion increases the resonant frequencies of beam, too, although the effect is relatively small.

It is observed that an increase in temperature leads to shifting of resonant frequencies and fluctuations in peak response magnitude. The shifting of the peak frequencies indicates a variation in the structural stiffness, caused by changes in the material and structural

dimensional properties. Likewise, variations in the peak response magnitude suggest a damping related phenomenon. Hence, it can be said that a combination of both structural stiffness and damping variations are involved in temperature change.

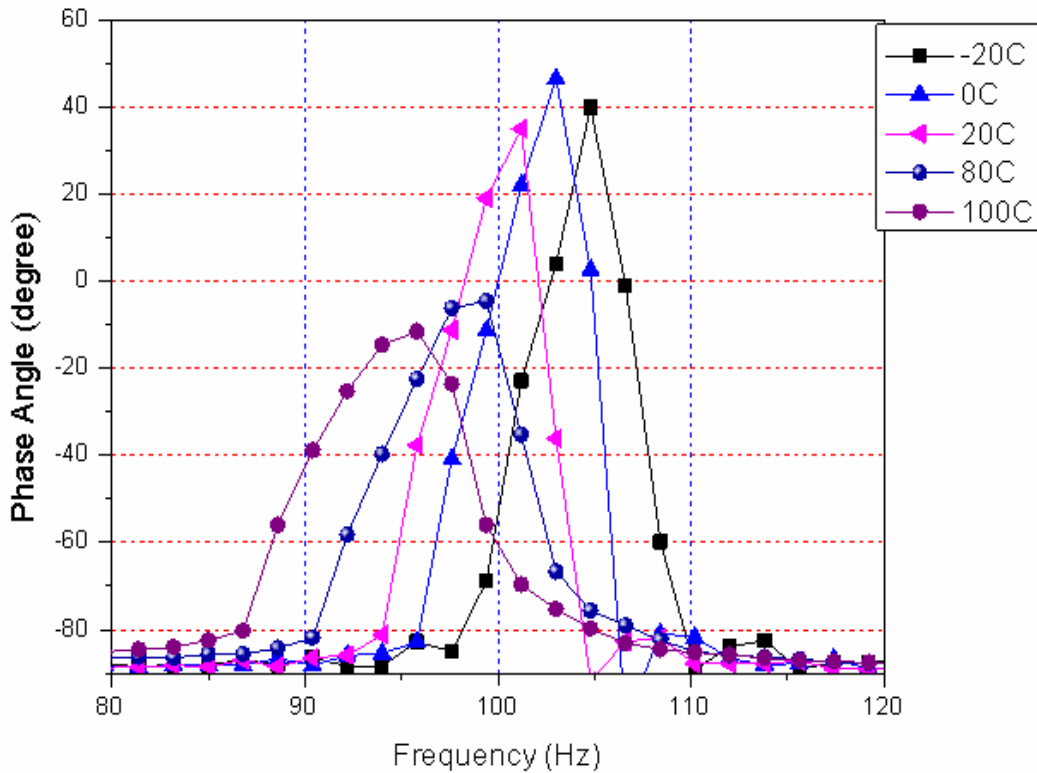


Figure 54: Shift in natural frequency of the PZT cantilever with temperature

Figure 54 shows the phase angle of the bimorph PZT cantilever beam. A real part, an imaginary part and a magnitude are demonstrated. All these plots indicate that the change in temperature leads to a horizontal shift and the peak frequencies. This verifies that the electrical impedance of PZT constitutes a unique signature of the dynamic behavior of the structure.

It is observed from Figure 55 and Figure 56 that an increase in temperature leads to shifting of resonant frequencies and fluctuations in peak response magnitude. The

shifting of the peak frequencies indicates a variation in the structural stiffness, caused by changes in the material and structural dimensional properties. Likewise, variations in the peak response magnitude suggest a damping related phenomenon. Hence, it can be said that a combination of both structural stiffness and damping variations are involved in temperature change.

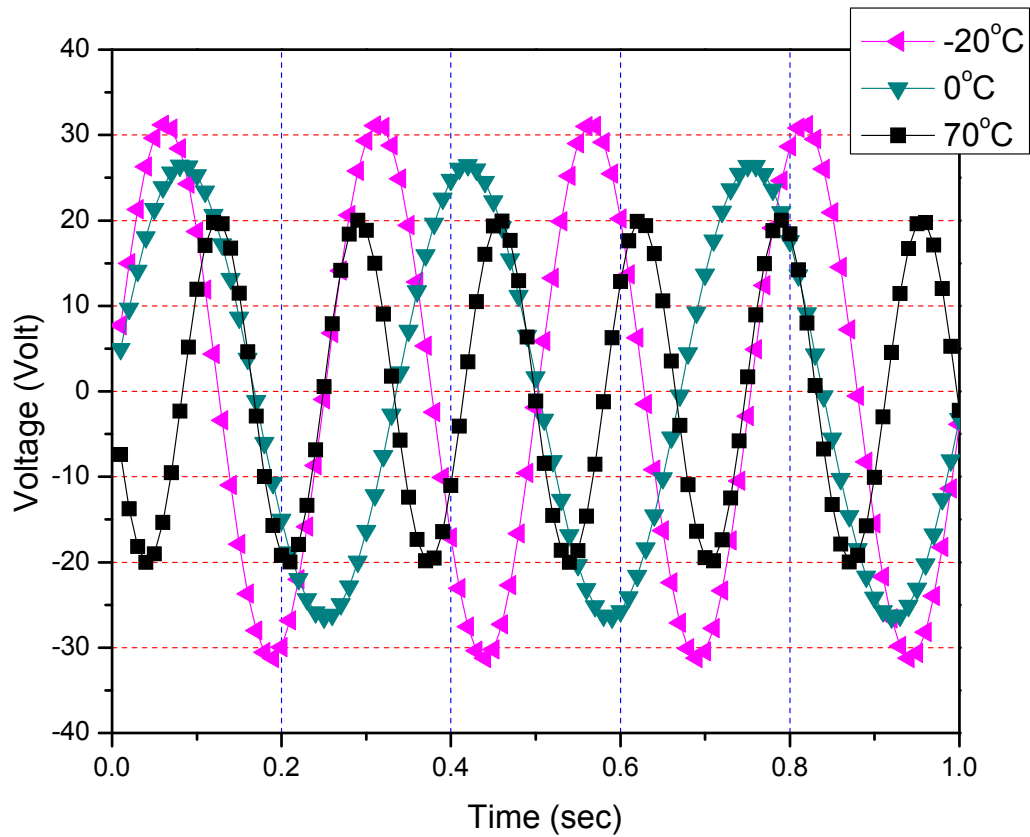


Figure 55: Time response of the PZT cantilever for different temperature

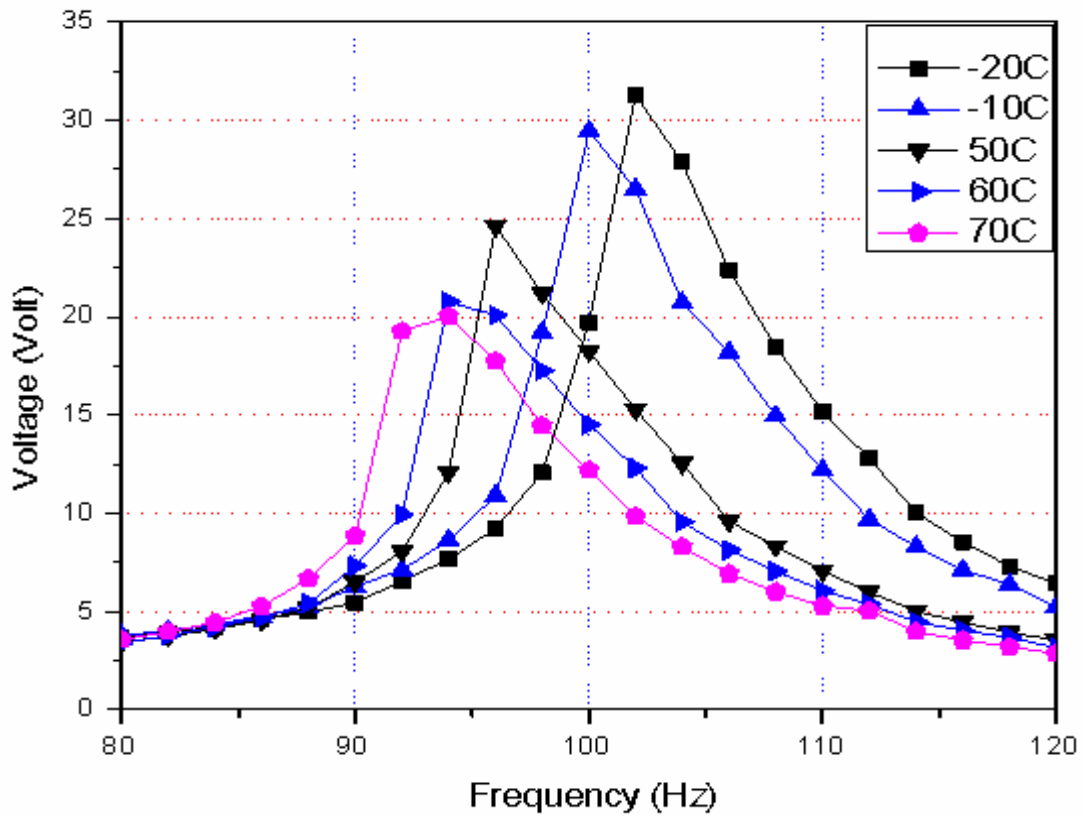


Figure 56: Shift in natural frequency of the PZT cantilever with temperature

It is also observed from Figure 56 that increase in temperature decreases the open circuit output voltage from the PZT generator. The peak-peak value of output voltage from the PZT is maximum at  $-20^{\circ}\text{C}$  (32V peak-peak) and decreases as the temperature increases and is minimum at  $70^{\circ}\text{C}$  (20V peak-peak). This can be explained from the fact that the voltage output for the PZT micropower generator is proportional to the piezoelectric charge coefficient ( $d_{31}$ ) and inversely proportional to the dielectric constant. As temperature increases, both  $d_{31}$  and dielectric constant values also increase, but the increase in dielectric constant is more prominent as compared to the piezoelectric charge coefficient ( $d_{31}$ ) and hence the net effect is a decrease in output voltage. Similar trends can also be observed in Figure 57. From Figure 57, it can be seen that the output voltage

increases with increase in load resistance and reaches a maximum value at around  $3M\Omega$  and remains almost constant after that. As the load resistance increases, the output voltage from the PZT generator approaches the open circuit value, which is expected.

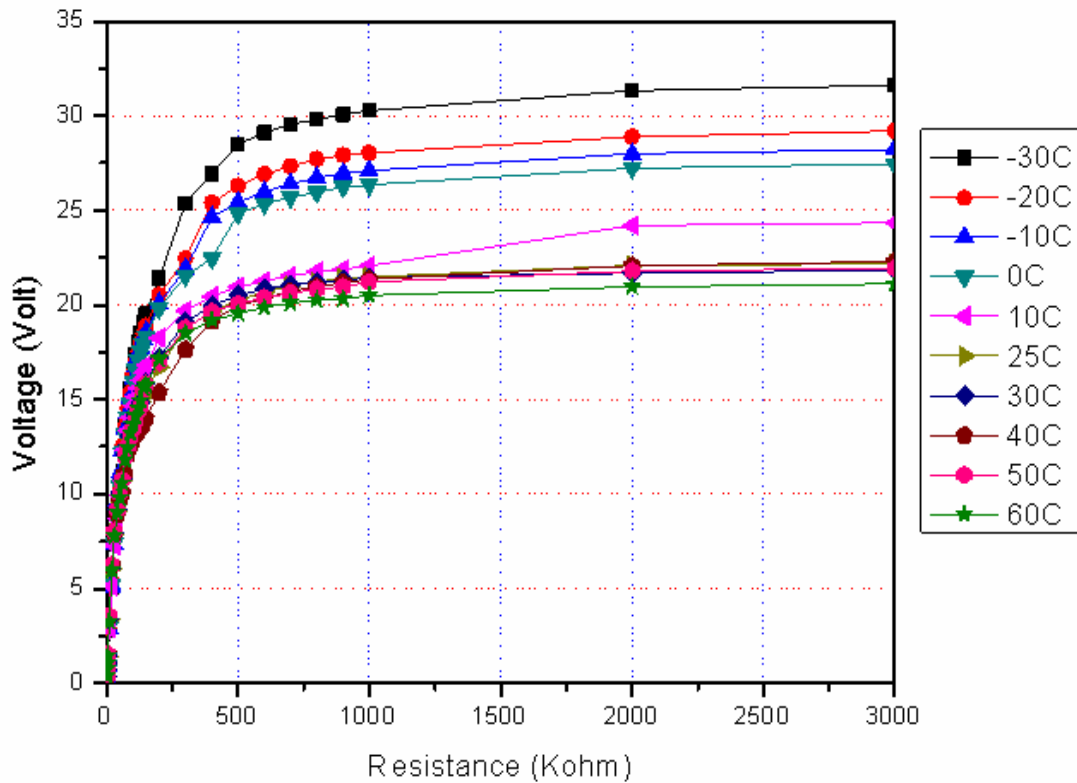


Figure 57: Output voltage vs. load resistance for PZT cantilever at different temperatures

Figure 58 and Figure 59 shows the trend in output power vs. the load resistance. It can be observed that the optimal load resistance for the PZT micropower generator decreases as the temperature increases. It can be explained in terms of the impedance of the micropower generator, as the temperature increases the impedance of the PZT micropower generator decreases as can be seen from Figure 18. The output power from the generator will maximum when the internal resistance matches with the load resistance.

As the impedance of the PZT micropower generator decreases with the temperature, so does the optimal load resistance for the system.

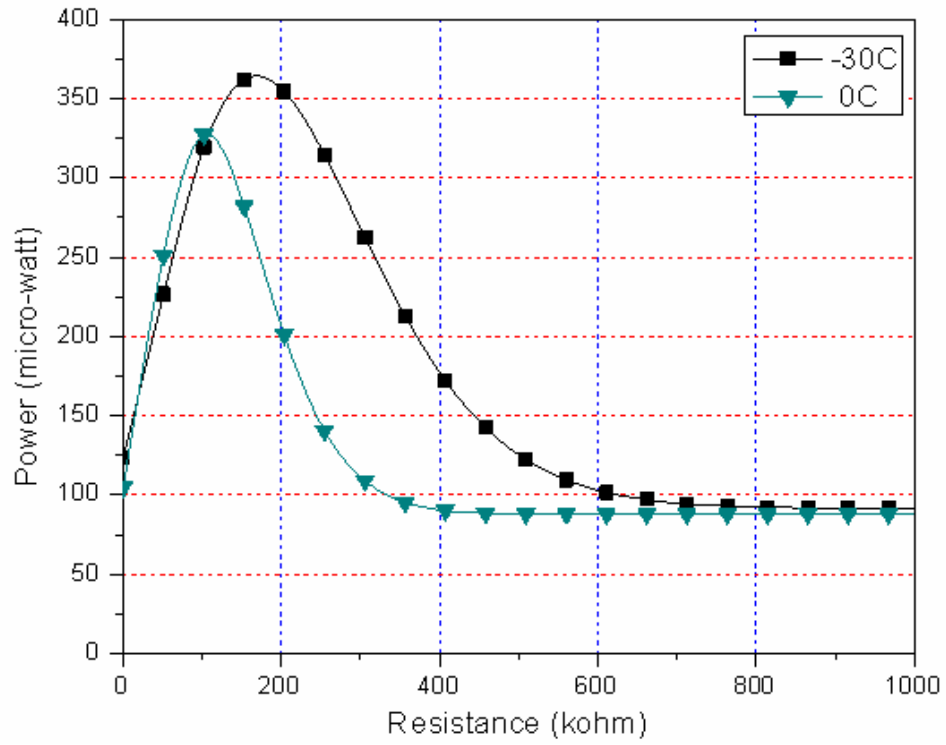


Figure 58: Output active power vs. load resistance for PZT cantilever at different temperatures

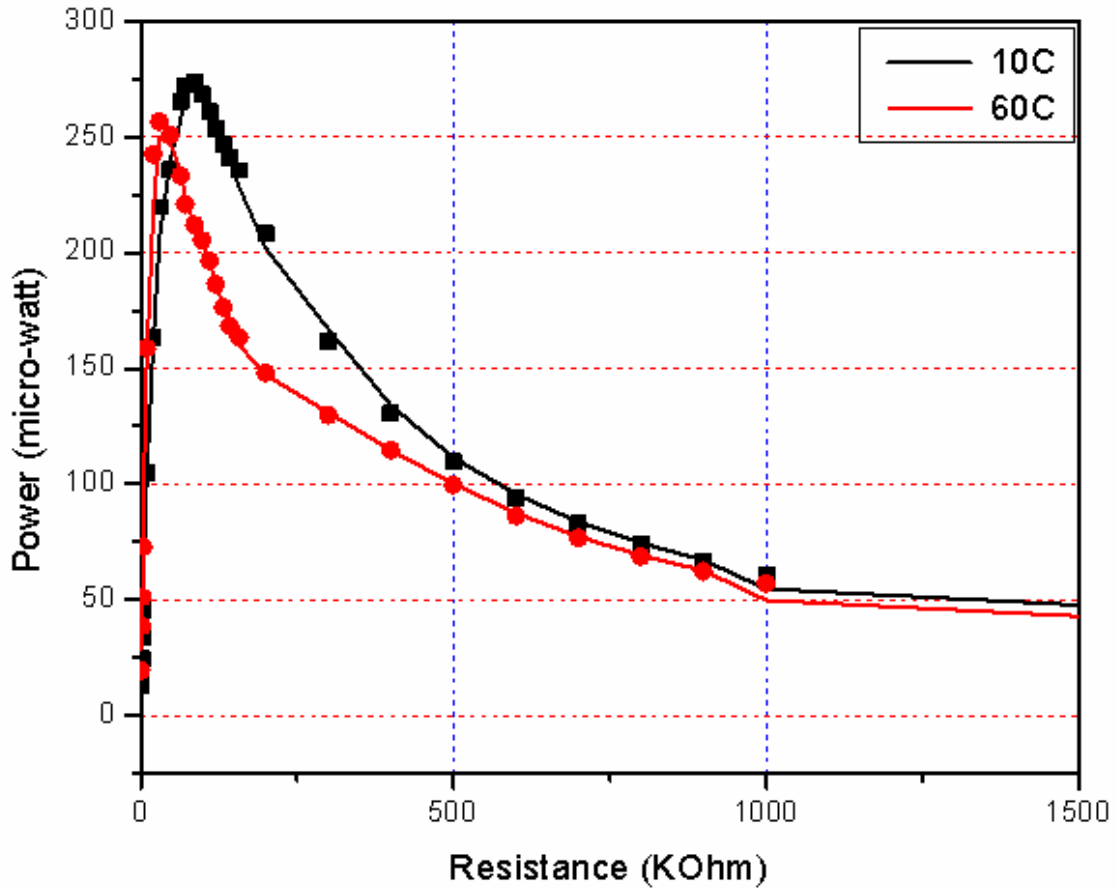
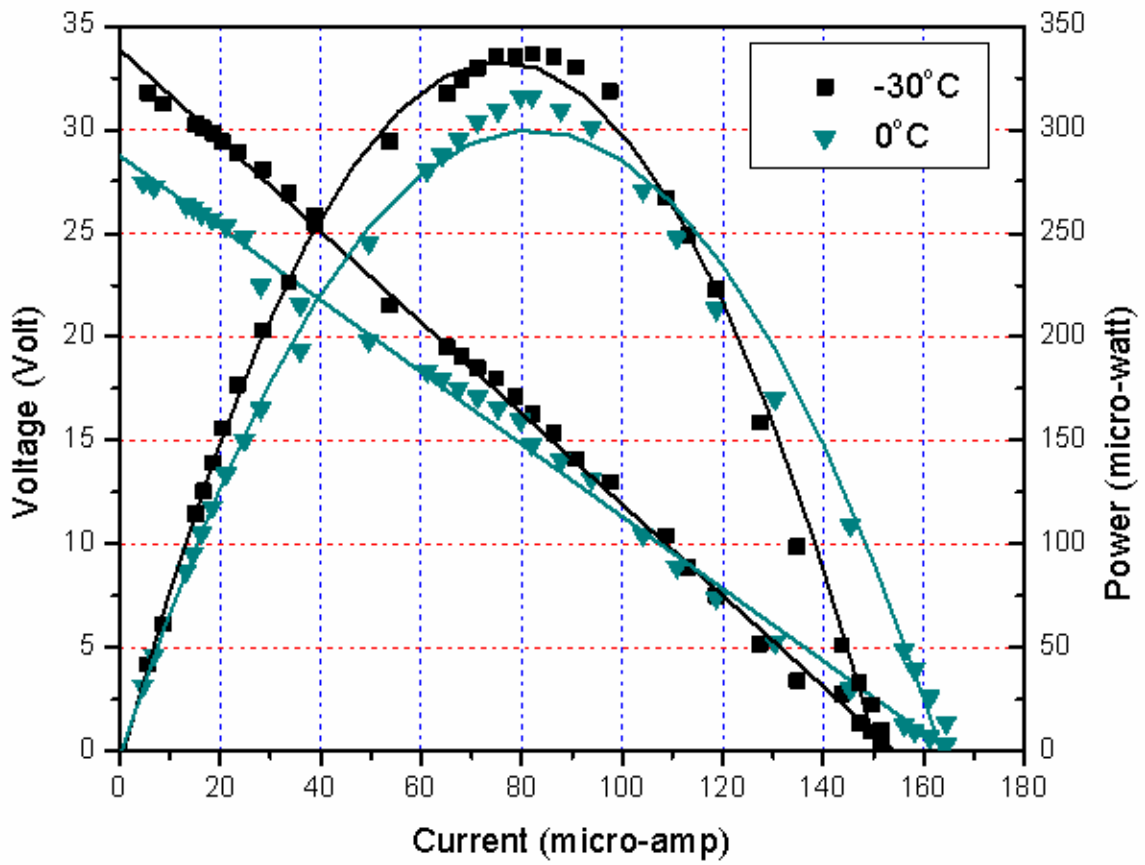


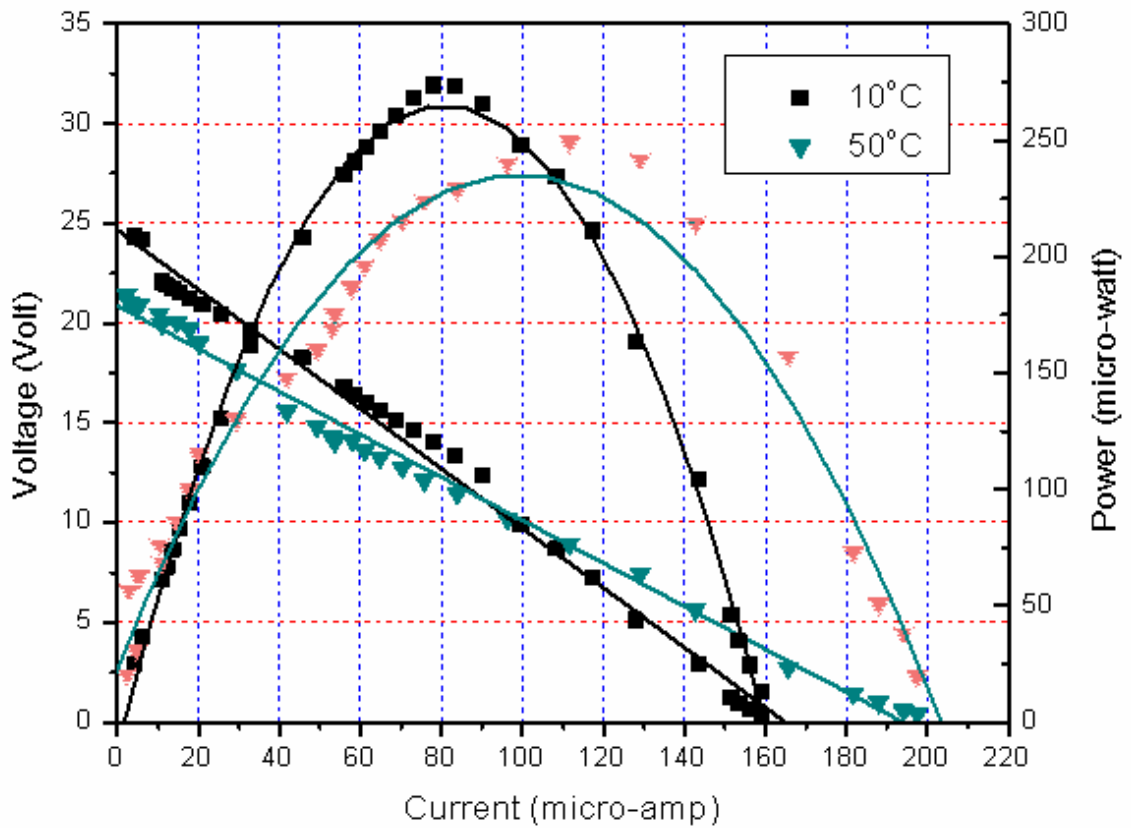
Figure 59: Output active power vs. load resistance for PZT cantilever at different temperatures

Figure 60 shows the I-V characteristics of the PZT micropower generator. It can be seen that the output power decreases with the increase in temperature; maximum at  $-30^{\circ}\text{C}$  and minimum at  $60^{\circ}\text{C}$ . The maximum output power is close to  $350\ \mu\text{W}$  at  $-30^{\circ}\text{C}$  and minimum is  $220\ \mu\text{W}$  at  $60^{\circ}\text{C}$ . Also the maximum output voltage follows the same trend. It can be explained from the fact that as the temperature increases the maximum output voltage decreases which results in the decrease of the maximum power output from the PZT micropower generator.





a) Temperature from 0 to -30°C



b) Temperature from 10 to 60°C

Figure 60: I-V curve for PZT cantilever

Figure 61 and Figure 62 shows the comparison of I-V characteristics for the micropower generator at 10°C and 0°C. The results shows reasonably close match to the experimental results.

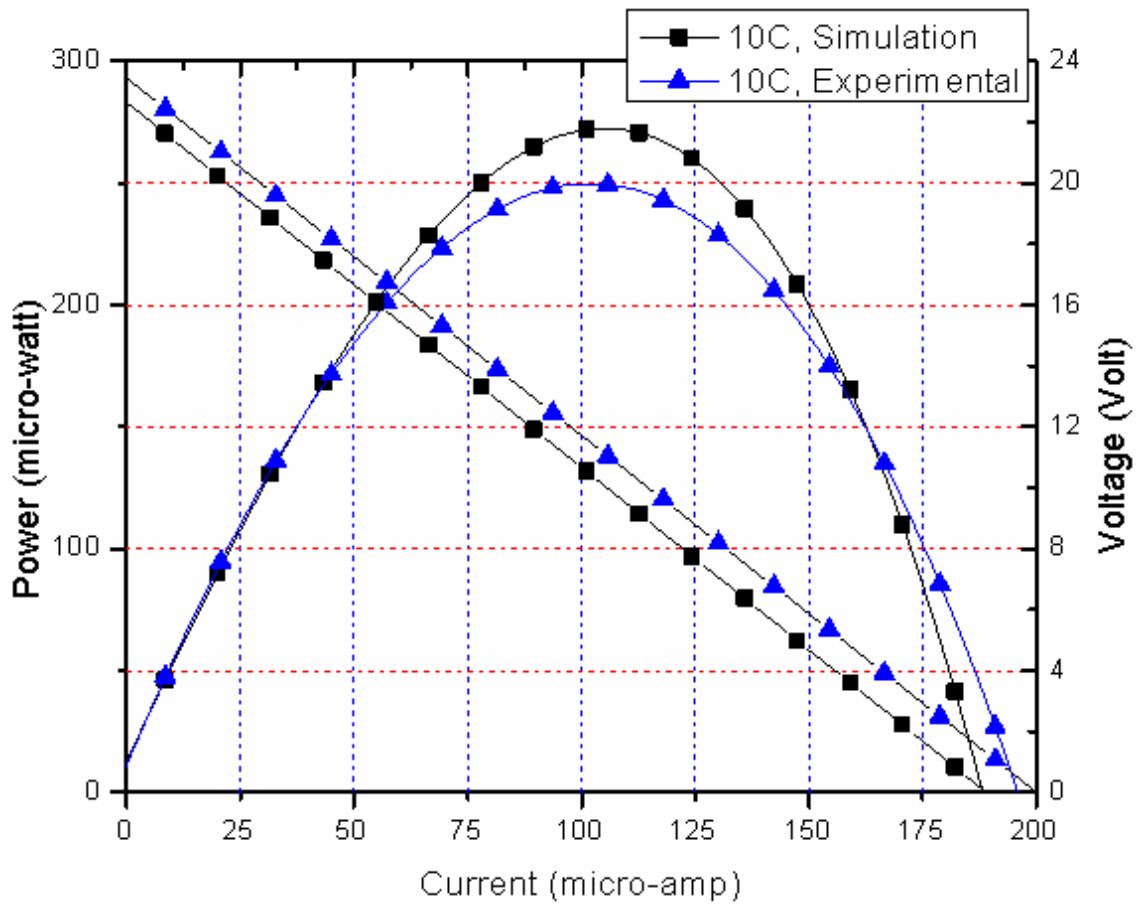


Figure 61: Comparison I-V curve for PZT cantilever at 10°C

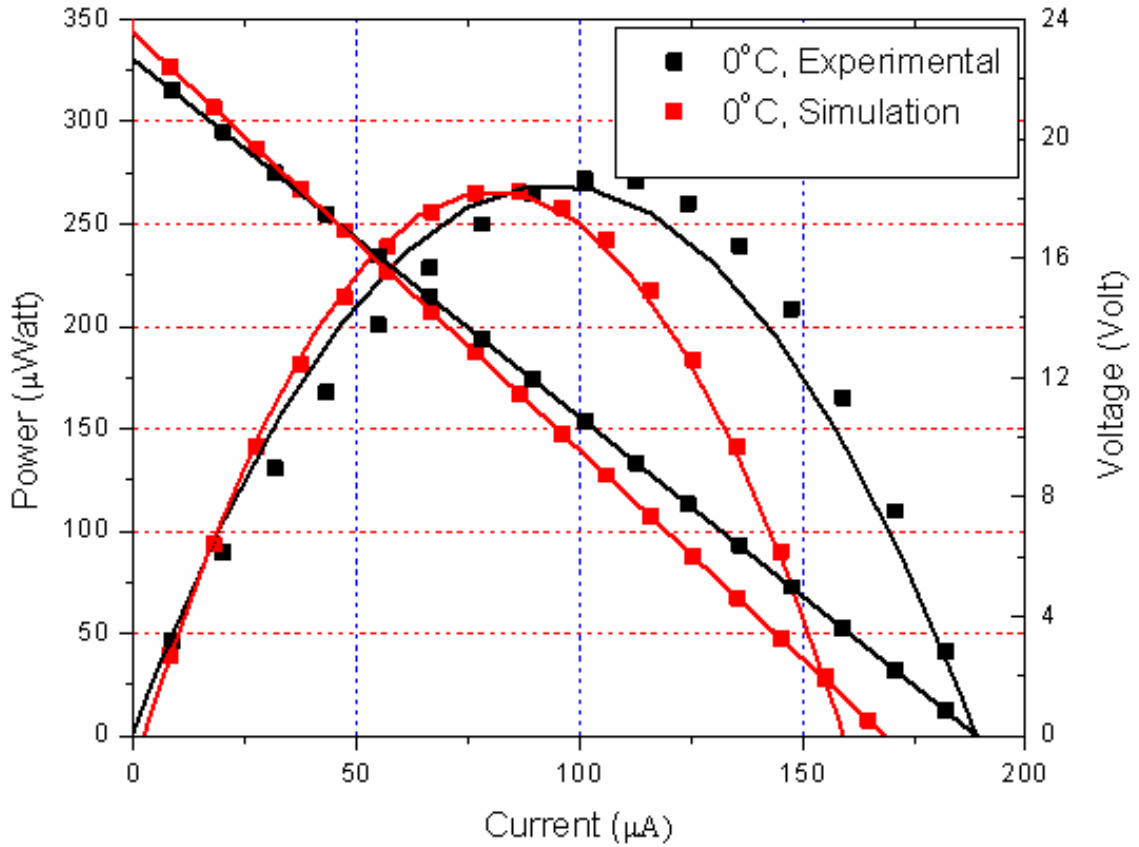


Figure 62: Comparison of I-V curve for PZT cantilever at 0°C

## 6.4 Results with Power Conversion Circuit

### 6.4.1 I-V curve at 1-g

The test is repeated with the Function Generator replaced by the PZT power source, and the result is shown in Figure 63.

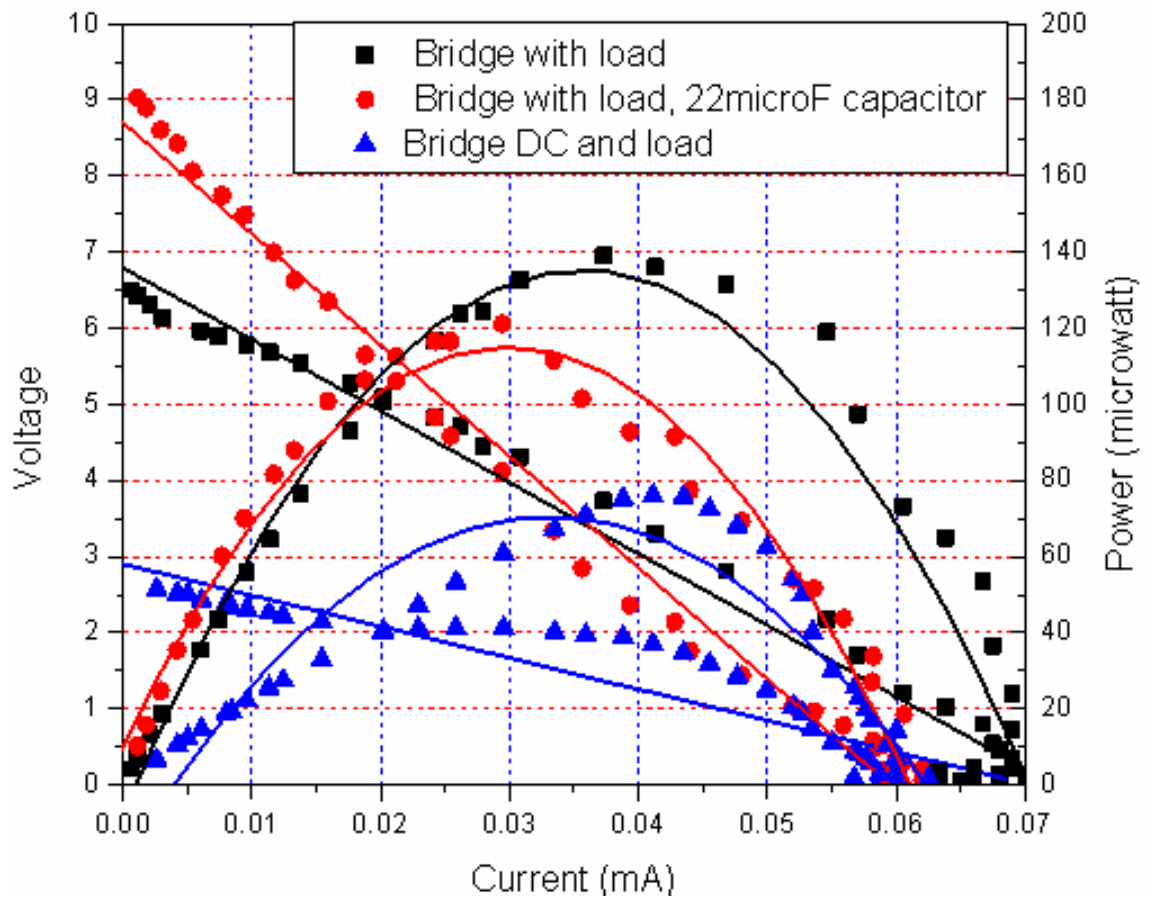


Figure 63: I-V curve with power conversion circuit at 1-g

#### 6.4.2 I-V curve at 3-g

The test is repeated with the Function Generator replaced by the PZT power source, and the result is shown in Figure 64.

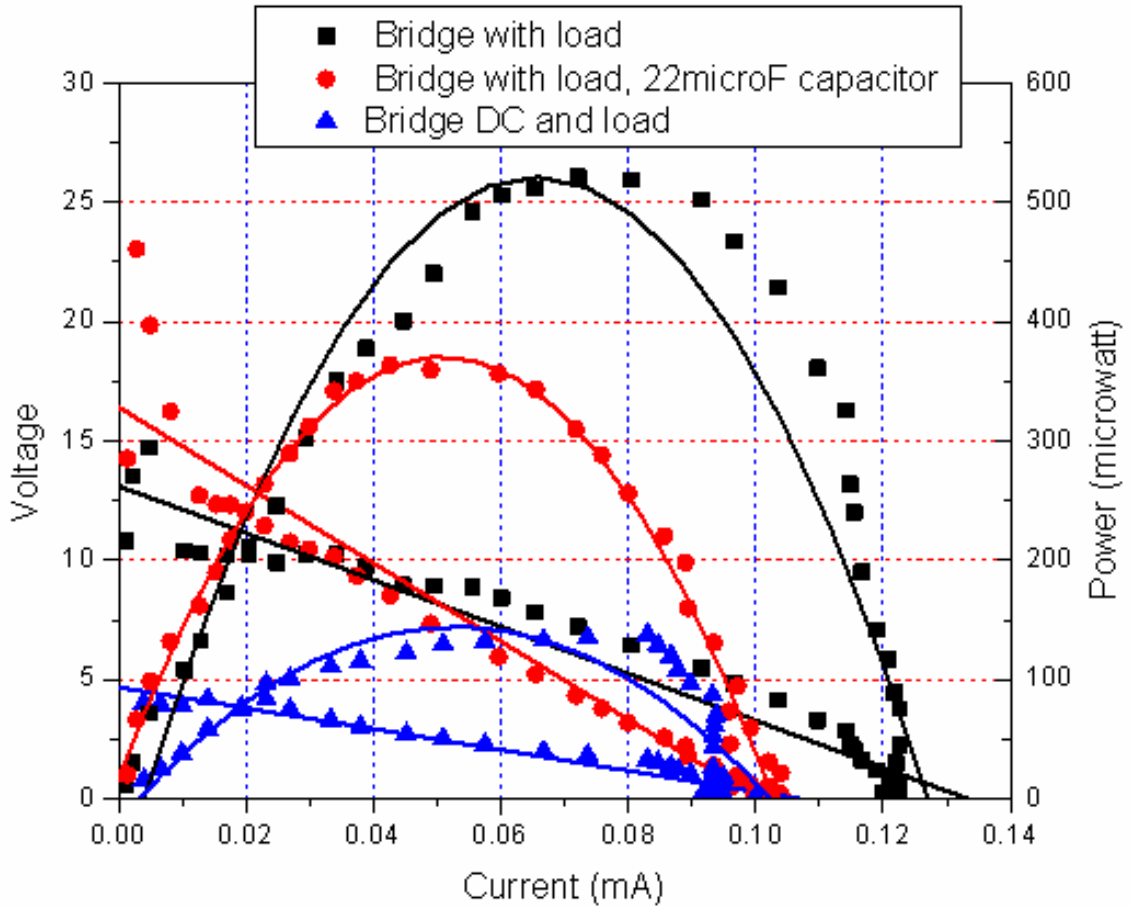


Figure 64: I-V curve with power conversion circuit at 3-g

The load tester is now connected with the power conversion circuit as a load. The output of the function generator is set to a 16V (peak-to-peak) sinusoidal wave with a frequency of 100Hz. The AC input voltage, DC/DC input voltage (Bridge output), DC/DC output voltage, and MOSFET drain to source voltage is shown in Figure 65, Figure 66, and Figure 67, respectively. Waveforms of AC input voltage, DC/DC input voltage (output voltage of the bridge rectifier), DC/DC output voltage, and drain to source voltage of the MOSFET are shown in the same figures, respectively.

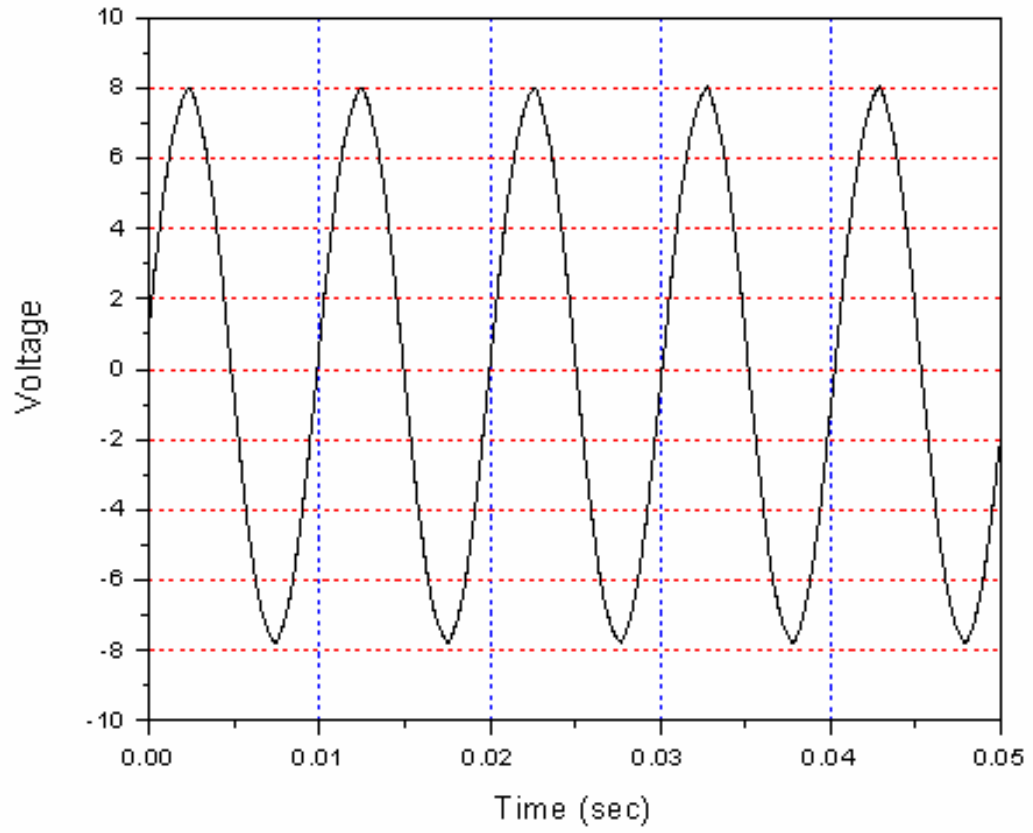


Figure 65: AC input voltage

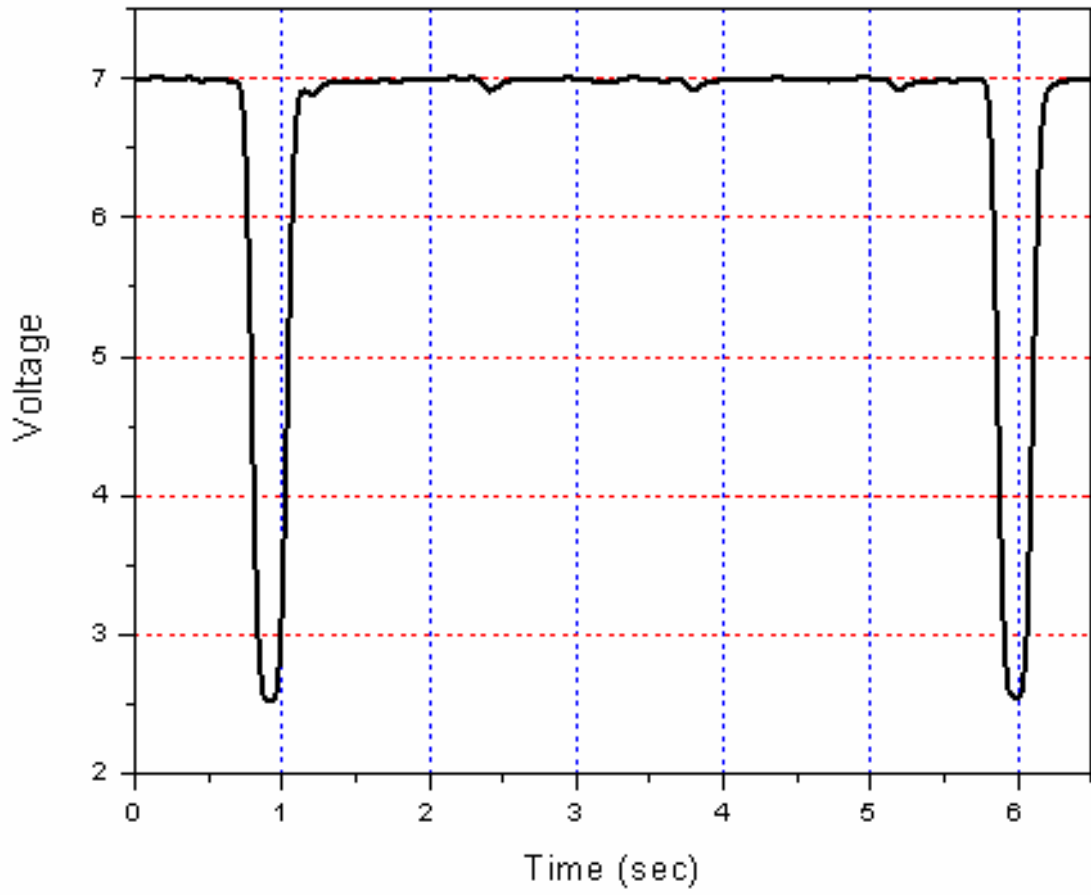


Figure 66: DC/DC input voltage (Bridge output)



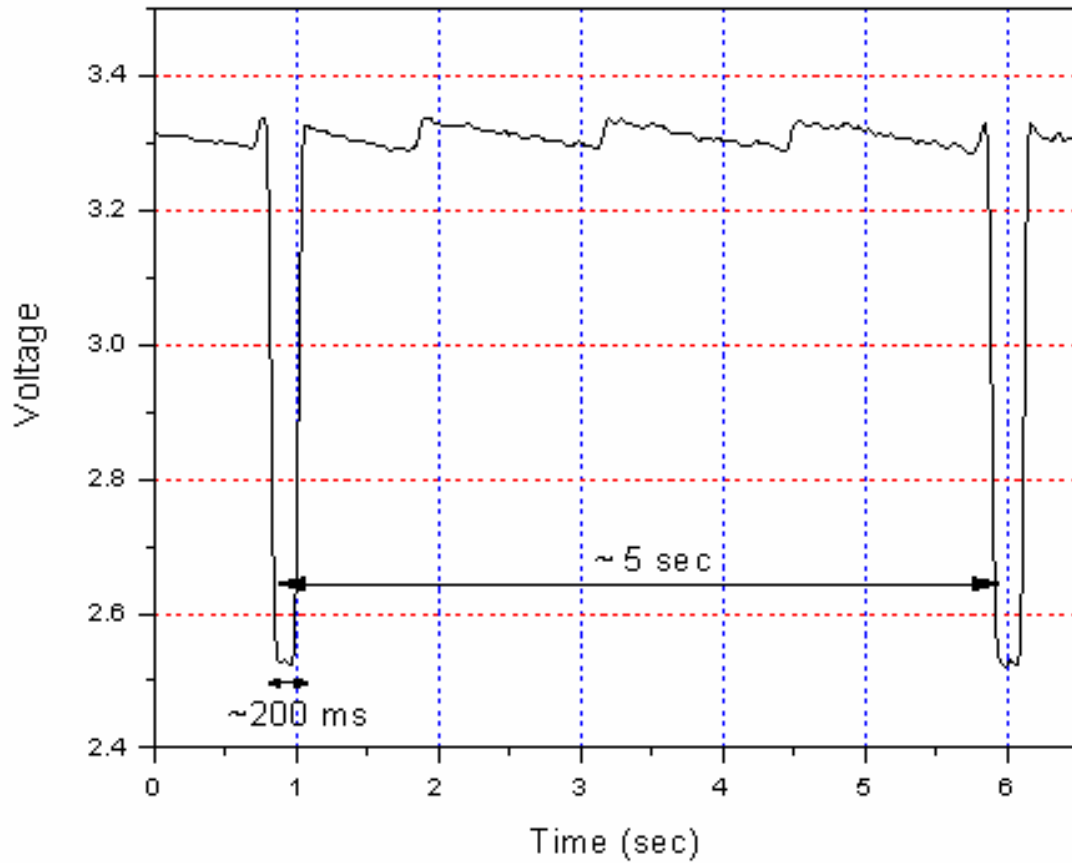


Figure 67: DC/DC output voltage

### 6.4.3 PZT with the load tester

The PZT is used as a power generator. The output capacitor of the DC/DC convert was varied to see the influences on the output voltages. The voltage at the DC/DC output is shown in Figure 68 and summarized in Table 5.

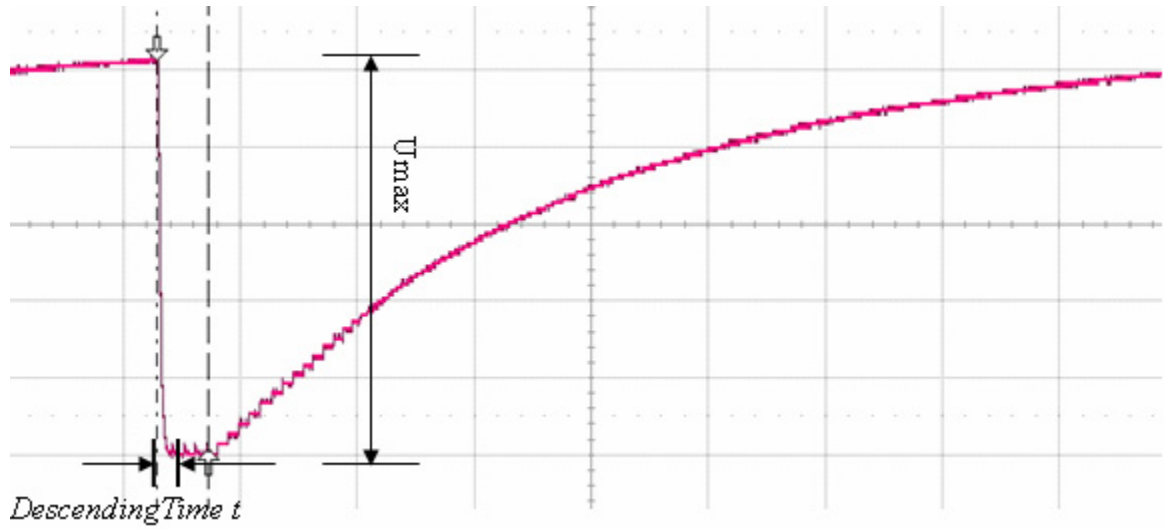


Figure 68: DC/DC output wave with PZT

Table 5: DC/DC output with PZT for different Capacitor

Output Capacitor ( $\mu\text{F}$ )	PZT@1G		PZT@3G	
	<i>Descending Time t (ms)</i>	<i>Maximum voltage <math>U_{max}</math> (V)</i>	<i>Descending Time t (ms)</i>	<i>Maximum voltage <math>U_{max}</math> (V)</i>
220	155	1.27	141	3.14
82	72	2.23	77	4.12
47	53	2.59	51	4.86
22	36	2.64	37	5.02

## 7 Conclusion and Discussion

Present research is conducted with a PZT bender to design a power generator. The materials are based on the 31 mode of operation because of the higher strain and lower resonant frequencies than those in 33 mode of operation. To understand and analyze the PZT materials in a cantilever beam structure in conjunction with a power conversion circuit, modeling techniques are employed. According to an intensive literature survey being carried out, three different models used for an actuation mode or a bimorph bender have been identified for a potential application on the bimorph bender with multiple layers as a power generator. The models implemented on the Matlab/Simulink/Simpower have been simulated and compared with experiments. The model based on the coupled field demonstrates the best among others to represent the behavior of a piezoelectric element in this specific application environment. The model based on an electrical equivalent circuit component is not able to show the dynamics involved in the vibration of the PZT, while the other model based on the energy conversion is unable to represent the effects of an electrical load on the damping behavior.

The experiments undertaken demonstrates that the system designed can supply a maximum power of 250  $\mu\text{W}$  at 100  $\text{k}\Omega$  resistive load when the PZT bender is excited with a vibration with an amplitude of 9.8  $\text{m/s}^2$  at 97.6 Hz. Once the load profile is specified, the power conversion can be optimized in conjunction with the bender

structure. However, the power becomes less and the voltage drops are observed when a rectifier is connected. Even though the voltage drops at the diodes and a fictitious internal resistor are being taken into account at the I-V curve, overall physical reasons for phenomena are not clear to understand.

Theoretical and experimental studies have been conducted for the temperature range of  $-20^{\circ}\text{C}$  to  $100^{\circ}\text{C}$ , which is typically the operating temperature range for military standards.

The experimental results were analyzed for a bimorph PZT device for the effects of temperature on resonant frequency and power generation. The analysis takes into account the empirical correlation of variations of dielectric constant, young's modulus, piezoelectric charge coefficient, and changes in dimension of PZT and shim material according to the variation of temperature. The experimental results and analysis reveals that the increase or decrease in temperature has effect both on the resonant frequency and the power output. The resonant frequency of the bimorph PZT cantilever and power output decreases with increase in temperature. The maximum output power was  $350\ \mu\text{watt}$  at  $-20^{\circ}\text{C}$  and minimum was  $220\ \mu\text{watt}$  at  $60^{\circ}\text{C}$ .

Discrepancies between the experimental results and the model are likely due to the following factors:

- 1) Uncertainties in the geometry of the device
- 2) Parasitic impedance in the actual device/sensing system
- 3) Unknown damping coefficient
- 4) Nonlinear piezoelectric properties

Using a root-sum-square uncertainty propagation method, it was found that a 5% uncertainty in the dimensions of the device causes an 11% uncertainty in the natural frequency of the device (2<sup>nd</sup> order mechanical model). This alone could account in the discrepancy between the peak power frequencies. Another source of uncertainty is the elastic modulus of the PZT layers. The elastic modulus of PZT is dependent on the electrical boundary conditions. For the model, it was assumed the elastic modulus given was under open circuit conditions. To compensate, the value was multiplied by  $(1-k^2)$  to get the approximate short circuit elastic modulus. This helped with matching the frequencies, but is still a source of uncertainty. Measuring the output might also affect the results; any parasitic impedance could affect the circuit, effecting the frequency and load at peak power. The damping coefficient is also very critical to the model, which seems to affect the voltage and power outputs more than the frequency and load at max power. Lastly, the model uses linear piezoelectric properties. Because PZT properties often exhibit nonlinear and hysteretic behavior, the assumption of linear properties should be questioned. The voltage and power results show that the model is fairly close to the experimental data when the natural frequencies match. The slight discrepancies present when natural frequency, output voltage and power are expected.

Consequently, future research work embrace investigations on this phenomenon by further development of a high fidelity computer model, which provide a tool to design a optimal structure and power conversion circuit with emphasis on the material properties used in the bender. Furthermore, efficient power conversion circuitry and management unit is also accomplished. Compared to reported micro-generators for vibration energy harvesting, our device offers the advantage of good performance as far as promising

voltage/power output and low natural frequency (to match general vibration sources) are concerned.

## References

1. Rabaey, J., Ammer, J., Karalar, T., Li, S., Otis, B., Sheets, M., Tuan, T., PicoRadios for Wireless Sensor Networks: The Next Challenge in Ultra- Low-Power Design. Proceedings of the International Solid-State Circuits Conference, San Francisco, CA, February 3-7, 2002.
2. Rabaey, J. M., Ammer, M. J., da Silva, J. L., Patel, D., Roundy S., PicoRadio Supports Ad Hoc Ultra-Low Power Wireless Networking, IEEE Computer, Vol. 33, No. 7, 2000, pp. 42-48.
3. Bohn, J., Coroama, V., Langheinrich, M., Mattern, F., Rohs, M., Disappearing Computers Everywhere – Living in a World of Smart everyday Objects, Institute of Pervasive Computing, ETH Zurich, Switzerland 2003.
4. Wang, D. E., Arens, T. Webster, and Shi, M., How the Number and Placement of Sensors Controlling Room Air Distribution Systems Affect Energy Use and Comfort, International Conference for Enhanced Building Operations, Richardson, TX, October 2002.
5. Hitachi Unveils Smallest RFID Chip. RFID Journal, March 14, 2003.
6. Roundy, S., On the effectiveness of vibration-base energy harvesting, Journal of Intelligent Material Systems and Structures, Vol. 16, October 2005.

7. Umeda, M., Nakamura, K., and Ueha, S., Analysis of the transformation of mechanical impact energy to electric energy using piezoelectric vibrator Japanese Journal of Applied Physics Vol. 35, 1996, pp. 3267-73.
8. Hausler, E. and Stein, L., Implantable Physiological Power Supply with PVDF Film, Ferroelectrics, Vol. 60, 1984, pp. 277-282.
9. Priya, S., Modeling of Electric energy Harvesting Using Piezoelectric Windmill, Applied Physics Letters, Vol. 87, 2005.
10. Kymisis, J., Kendall, C., Paradiso, J., Gershenfeld, N., Parasitic power harvesting in shoes, 2nd IEEE Int. Conf. on Wearable Computing, 1998, pp.132–137.
11. Kasyap, A., Lim, J., Johnson, D., Horowitz, S., Nishida, T., Ngo, K., Sheplak, M., Cattafesta, L., Energy reclamation from a vibrating piezoelectric composite beam, 9th Annual Conf. on Sound and Vibration (Orlando, FL), 2002, pp. 36–43.
12. Ramsay, M.J., Clark, W.W., Piezoelectric energy harvesting for bio-MEMS application Smart Structures and Materials: Industrial and Commercial Applications of Smart Structures Technologies, Vol. 4332, 2001, pp. 429-38.
13. Gonzalez, J.L., Rubio, A., Moll, F., Human powered piezoelectric batteries to supply power to wearable electronic devices, International Journal- Society of Materials Engineering for Resources, Vol. 10, Part 1, 2001, pp. 34-40.
14. Smits, J. G., Choi, W. S., The constituent equations of piezoelectric heterogeneous bimorphs, IEEE Transactions on Ultrasonics, Ferroelectrics, and Frequency Control, Vol. 38, No. 3, 1991, pp. 256-270.



15. Huang, C., Lin, Y.Y., Tang, T. A., Study on the tip-deflection of a piezoelectric bimorph cantilever in the static state, *Journal of Micromechanics and Microengineering*, Vol. 14, 2004, pp.530-34.
16. DeVoe, D. L., Pisano, A. P., Modeling and optimal design of piezoelectric cantilever microactuators, *Journal of Microelectromechanical systems*, Vol. 6, No. 3, 1996, pp. 266-270.
17. Hwang, W. S., Park, H. C., Finite element modeling of piezoelectric sensors and actuators, *AIAA Journal*, Vol. 31, No. 5, 1993, pp. 930-37.
18. Roundy, S., Wright, P.K., A piezoelectric vibration based generator for wireless electronics, *Smart Materials and Structures*, Vol. 13, 2004, pp. 1131-42.
19. Roundy, S., Leland, E. S., Baker, J., Carleton, E., Reilly, E., Lai, E., Otis, B., Rabaey, J. M., Wright, P. K., Sundararajan, V., Improving power output for vibration-based energy scavengers, *IEEE Transactions on Pervasive Computing*, Vol. 4, Issue 1, 2004, pp. 28- 36.
20. Lu, F., Lee, H.P., Lim, S.P., Modeling and analysis of micro piezoelectric power generators for micro-electromechanical-systems applications, *Smart Materials and Structures*, Vol. 13, 2004, pp. 57-63.
21. Eggborn, T., Analytical models to predict power harvesting with piezoelectric materials, Master's Thesis Virginia Polytechnic Institute and State University, 2003.
22. Kim, S., Low power energy harvesting with piezoelectric generators, PhD Thesis, University of Pittsburgh, 2002.

23. Shen, D., Ajitsaria, J., Choe, S-Y., Kim, D-J., The optimal design and analysis of piezoelectric cantilever beams for power generation devices, Materials Research Society Symposium Proceedings, Vol. 888, 2006.
24. Ottman G. K., Hofmann H. F., Lesieutre G. A., Optimized piezoelectric energy harvesting circuit using step-down converter in discontinuous conduction mode. IEEE Transactions on Power Electronics, Vol.18, No.2, 2003, pp. 696-703.
25. Ottman G. K., Hofmann H. F., Bhatt A. C., Lesieutre G. A., Adaptive piezoelectric energy harvesting circuit for wireless remote power supply. IEEE Transactions on Power Electronics, Vol.17, No.5, 2002, pp. 669-76.
26. Williams, C.B, Yates, R.B., Analysis of a micro-electric generator for Microsystems, Transducers 95/Eurosensors IX, 1995, pp. 369 – 372.
27. Shearwood, C., Yates, R.B., Development of an electromagnetic micro-generator, IEE Electronics Letters, Vol.33, No.22, 1997, pp.1883-4.
28. Williams, C.B., Shearwood, C., Harradine, M.A., Mellor, P.H., Birch, T.S., Yates, R.B., Development of an electromagnetic micro-generator, IEEE Proceedings-Circuits, Devices and Systems, Vol.148, No.6, 2001, pp. 337-42.
29. Williams, C.B., Woods, R.C., Yates, R.B., Feasibility study of a vibration powered micro-electric generator, Proceedings of IEE colloq. Compact power sources (digest No. 96/107), May 1996, pp. 7/1-7/3.
30. Amirtharajah, R., Design of Low Power VLSI Systems Powered by Ambient Mechanical Vibration, Ph.D Thesis, Department of Electrical Engineering, Massachusetts Institute of Technology, June 1999.

31. Amirtharajah, R., Chandrakasan, A.P., Self-Powered Signal Processing Using Vibration-Based Power Generation, IEEE Journal of Solid State Circuits, Vol. 33, No. 5, 1998, pp. 687-695.
32. Meninger, S., Mur-Miranda, J. O., Amirtharajah R., Chandrakasan, A. P., Lang, J., Vibration-to-Electric Conversion, ISPLED99 San Diego, CA, USA, 1999, pp. 48-53.
33. Amirtharajah, R., Meninger, S., Mur-Miranda, J. O., Chandrakasan, A. P., Lang, J., A Micropower Programmable DSP Powered using a MEMS-based Vibration-to-Electric Energy Converter, IEEE International Solid State Circuits Conference, 2000, pp. 362-363.
34. Meninger, S., Mur-Miranda, J.O., Amirtharajah, R., Chandrakasan, A.P., Lang, J.H., Vibration-to-Electric Energy Conversion, IEEE Trans. VLSI Syst., Vol. 9, 2001, pp. 64-76.
35. Priya, S., Modeling of Electric energy Harvesting Using Piezoelectric Windmill, Applied Physics Letters, Vol. 87, 2005.
36. White, N. M., Glynne-Jones, P., Beeby, S., A novel thick-film piezoelectric micro-generator, Smart Materials and Structures, Vol. 10, 2001, pp. 850-852.
37. Jones, P.G., Beeby, S.P., White N.M., Towards a Piezoelectric Vibration-Powered micropower generator, IEE Proc.- Sci. Meas. Technol., Vol 148, No. 2, March 2001, pp. 68-72.
38. Glynne-Jones, P., Beeby, S., James, E. P., White, N. M., The modeling of a piezoelectric vibration powered generator for microsystems, Proc. 11th Int.

- Conf. Solid-State Sensors and Actuators, Transducers '01 and Eurosensors XV, Munich, Germany, June 2001, pp. 46–49.
39. Tanaka, H., Ono, G., Nagano, T., Ohubo N., Electric Power Generation Using Piezoelectric Resonator for Power-Free Sensor Node, Proceedings of IEEE Custom Integrated Circuits Conference, 2005, pp. 97-100.
40. Mohammadi, F., Khan, A., Cass, R.B., Power Generation from Piezoelectric Lead Zirconate Titanate Fiber Composites, Material Research Society Symposium Proceeding, Vol. 736, 2003, pp. D5.5.1-D5.5.6
41. Ayers, J., Greve, D.W., Oppenheim, I.J., Energy Scavenging for Sensor Application using Structural Strains, Smart structures and Materials: Smart Systems and Nondestructive Evaluation for Civil Infrastructures, Proceedings of SPIE, Vol. 5057, 2003, pp. 364-375.
42. Platt, S.R., Farritor, S., Haider, H., On Low-Frequency Electric Power Generation with PZT Ceramics, IEEE/ASME transactions on Mechatronics, Vol. 10, No. 2, 2005, pp. 240-252.
43. Li, W. J., Chan, G. M. H., Ching, N. N. H., Leong, P. H. W., Wong, H. Y., Dynamical modeling and simulation of a laser-micromachined vibration-based micro power generator, Int. J. Nonlinear Sci. Simulation, Vol. 1, 2000, pp. 345–353.
44. Li, W. J., Ho, T. C. H., Chan, Leong, P. H. W., Wong, H. Y., Infrared signal transmission by a laser-micromachined vibration-induced power generator, Proc. 43rd IEEE Midwest Symp. Circuits and Syst., Vol. 1, 2000, pp. 236–239.

45. Ferrari, M., Ferrari, V., Marioli, D., Taroni, A., Modeling, Fabrication and Performance Measurements of a Piezoelectric energy Converter for Power Harvesting in Autonomous Microsystems, IMTC- Instrumentation and Measurement technology Conference, Canada, May 2005, pp. 1862-1866.
46. Shu, Y.C., Lien, I.C., Analysis of Power Output for Piezoelectric Energy Harvesting Systems, Smart Materials and Structures, Vol. 15, 2006, pp. 1499-1512.
47. Shu, Y.C., Lien, I.C., Efficiency of energy Conversion for a Piezoelectric Power Harvesting System, Smart Materials and Structures, Vol. 16, 2006, pp. 2429-2438.
48. Smith, R.C., Smart material systems: model development, Society for Industrial and Applied Mechanics, 2005.
49. Weinberg, M., Working equations for piezoelectric actuators and sensors, Journal of Microelectromechanical Systems, Vol. 8, No. 4, 1991, pp. 529-33.
50. Lee, H-J., Saravanos, D.A., The effect of temperature dependent material nonlinearities on the response of piezoelectric composite plates, Lewis Research Center, NASA, NASA/TM—97-206216, 1997.
51. Rabaey, J., Ammer, J., Karalar, T., Li, S., Otis, B., Sheets, M., Tuan, T., PicoRadios for Wireless Sensor Networks: The Next Challenge in Ultra- Low-Power Design. Proceedings of the International

## Nomenclature

$I$  = Moment of inertia

$\sigma$  = Stress in the beam.

$x$  = Distance from the base of the beam.

$M(x)$  = Moment in the beam as a function of the distance ( $x$ ) from its base.

$l_m$  = Length of the proof mass.

$\ddot{y}$  = Input vibration in terms of acceleration.

$z$  = Vertical displacement

$V$  = Voltage

$D$  = Electrical displacement

$\{\varepsilon\}$  = Strain vector

$\{\sigma\}$  = Stress vector

$\{D\}$  = Three dimensional electric displacement vector

$\{H\}$  = Electric field vector

$[s^E]$  = Six by six compliance matrix evaluated at constant electric field

$[d]$  = Three by six matrix of piezoelectric strain coefficients

$[v^T]$  = Three by three dielectric constant matrix evaluated at constant stress.

$t_{sh}$  = Thickness of metal layer

$t_p$  = Thickness of PZT layer

$E_{sh}$  = Young's modulus of metal layer

$E_p$  = Young's modulus of PZT layer

$l$  = length of the cantilever beam

$w$  = width of the cantilever beam

$H$  = Electric fields

$T$  = Temperature

$T_c$  = Curie temperature

$P$  = Polarization

$S$  = Entropy

$d_{31}$  = Piezoelectric strain constant

$C$  = Capacitance

$R$  = Resistance

$A$  = Cross-sectional area

$\epsilon_r$  = Relative dielectric constant

$\epsilon_0$  = Dielectric constant of air

$t$  = Thickness or plate separation

$Q$  = Charge

## Appendix

List of parameters of the PZT cantilever:

Parameters	Values	Comments
$E_p$	6.2E+10 N/m <sup>2</sup>	Elastic modulus of PZT
$E_{sh}$	6.6E+10 N/m <sup>2</sup>	Elastic modulus of center shim (brass)
W	3.2 mm	Width of the beam
E	1800	Dielectric constant of PZT
$t_p$	0.134 mm	Thickness of single PZT layer
$t_{sh}$	0.132 mm	Thickness of center shim
$l_b$	25.60 mm	Length of PZT
M	0.5894 grams	Proof mass
$\Xi$	0.02	Damping ratio
Y	9.8 m/s <sup>2</sup>	Input acceleration
$D_{31}$	-1.9E-10 m/V	Piezoelectric voltage constant
$K_{31}$	0.32	Piezoelectric coupling coefficient

Matlab/Simulink programs:

```
%Uncertainly Propagation for Bulk PZT-5H Bimorph Prototype
```

```
clear all
format compact
```

```
%average variable uncertainty
u_ave=5      %%
```



```

L=25.35e-3;      %m
L_u=L*u_ave/100;
lm=3.26e-3;     %m
lm_u=lm*u_ave/100;
wm=3.05e-3;     %m
wm_u=wm*u_ave/100;
hm=3.07e-3;     %m
hm_u=hm*u_ave/100;
tp=0.134e-3;   %m
tp_u=tp*u_ave/100;
tsh=0.129e-3;  %m
tsh_u=tsh*u_ave/100;
wp=3.2e-3;     %m
wp_u=wp*u_ave/100;
Esh=1.1e11;    %N/m^2
Esh_u=Esh*u_ave/100^0;
kpeiz=0.44;
Ep=6.2e10*(1-kpeiz^2);    %N/m^2
Ep_u=Ep*u_ave/100^0;
rhosh=8800;    %kg/m^3
rhosh_u=rhosh*u_ave/100^0;
rhop=7800;    %kg/m^3
rhop_u=rhop*u_ave/100^0;
rhom=1.93e4;  %kg/m^3
rhom_u=rhom*u_ave/100^0;
l=L-lm/2;
l_u=sqrt(L_u^2+lm_u^2/4);

d31=3.20e-10; %m/V
e=3.36e-8;    %F/m

tand=0.05;    %loss tan
c=0.02;      %kg/s

%Tip Mass Uncertainty
M=rhom*lm*wm*hm
Mrhom=lm*wm*hm;
Mlm=rhom*wm*hm;
Mwm=rhom*lm*hm;
Mhm=rhom*lm*wm;
M_u=sqrt((Mrhom*rhom_u)^2+(Mlm*lm_u)^2+(Mwm*wm_u)^2+(Mhm*hm_u)^2)
M_per=M_u/M*100

%Sectional Stiffness Uncertainty
l=1/12*wp*tsh^3+1/6*Ep/Esh*wp*tp^3+1/2*tp*Ep/Esh*wp*(tp+tsh)^2
lwp=1/12*tsh^3+1/6*Ep/Esh*tp^3+1/2*tp*Ep/Esh*(tp+tsh)^2;
ltsh=1/4*wp*tsh^2+Ep/Esh*(tp+tsh)*tp*wp;
IEp=1/6*wp*tp^3/Esh+1/2*tp*wp*(tp+tsh)^2/Esh;
IEsh=-1/6*Ep/Esh^2*wp*tp^3-1/2*tp*Ep/Esh^2*wp*(tp+tsh)^2;
ltp=1/2*Ep/Esh*wp*tp^2+1/2*Ep/Esh*wp*(3*tp^2+4*tsh*tp+tsh^2);
l_u=sqrt((lwp*wp_u)^2+(ltsh*tsh_u)^2+(IEp*Ep_u)^2+(IEsh*Esh_u)^2+(ltp*tp_u)^2)
l_per=l_u/l*100

EI=Esh*I

```

```

EI_u=sqrt((Esh*I_u)^2+(I*Esh_u)^2)
EI_per=EI_u/EI*100

%Beam Mass Uncertainty
Mb=L*wp*(2*tp*rhop+tsh*rhosh)
MbL=wp*(2*tp*rhop+tsh*rhosh);
Mbtp=L*wp*2*rhop;
Mbw=L*(2*tp*rhop+tsh*rhosh);
Mbrhop=L*wp*(2*tp);
Mbtsh=L*wp*rhosh;
Mbrhosh=L*wp*tsh;
Mb_u=sqrt((MbL*L_u)^2+(Mbtp*tp_u)^2+(Mbw*wp_u)^2+(Mbrhop*rhop_u)^2+(Mbtsh*tsh_u)^2+
(Mbrhosh*rhosh_u)^2)
Mb_per=Mb_u/Mb*100

%Total Mass Uncertainty
Mt=33/140*Mb+M
Mt_u=sqrt((33/140*Mb_u)^2+(M_u)^2)
Mt_per=Mt_u/Mt*100

%Stiffness Uncertainty
k=3*EI/I^3
%k=wp*Esh*tsh^3/4/I^3+wp*Ep/I^3*(3/2*tsh^2*tp+3*tsh*tp^2+2*tp^3)
kl=-9*EI/I^4;
kEI=3/I^3;
k_u=sqrt((kl*I_u)^2+(kEI*EI_u)^2)
k_per=k_u/k*100

%Natural Frequency Uncertainty
f=sqrt(k/Mt)/2/pi
fk=1/4/pi/sqrt(k*Mt);
fMt=-1/4/pi/sqrt(Mt)^3*sqrt(k);
f_u=sqrt((fk*k_u)^2+(fMt*Mt_u)^2)
f_per=f_u/f*100

%alpha (coupling coef)
alphas=3*wp*Ep*d31/4/I*(tsh+tp)
Cps=e*wp*L/tp/2*(1-tand*1i)

alphap=3*wp*Ep*d31/2/I*(tsh+tp)
Cpp=2*e*wp*L/tp*(1-tand*1i)*1.1

%system coef
A1s=-1/Mt
A2s=-k/Mt
A3s=alphas/Mt
A4s=-alphas/Cps
A5s=-1/Cps

A1p=-1/Mt
A2p=-k/Mt
A3p=alphap/Mt
A4p=-alphas/Cpp
A5p=-1/Cpp

```

```

% Constants supplied to the Electrical Equivalent circuit model in simulink
clc;
clear all;
E_metal= 11e10; %Pa Young's modulus
E_pzt=66e9; %Pa Young's modulus
ns=E_pzt/E_metal; % Ration of elastic constants
np=2; % Number of PZT layer
m=0.0005894;% in Kg
lb=25.60e-3; %m beam length
le=25.60e-3; %m length of electrode
lm=3.26e-3; %m length of proof mass
width=3.22e-3; %m beam width
thick_pzt=0.134e-3;%m thickness
thick_metal=0.132e-3;%m thickness
b=(thick_pzt+thick_metal)/2;
%I =
(2*width*(thick_pzt)^3/12)+(2*width*thick_pzt*((thick_metal+thick_pzt)/2)^2)+(E_pzt*width*(thick_
metal)^3/(E_metal*12)); %m^4 M. A. of inertia
I= (((width*np*thick_pzt^3)/12)+width*np*thick_pzt*b^2)+(ns*width*thick_metal^3)/12;
zeta=0.02; %Damping ratio
wn=540; % Resonant frequency of beam
Epiezo=1800*8.85e-12; % Dielectric constant
d31=-1.90e-10; % m/volt piezoelectric voltage constant
K1=(b*(2*lb+lm-le))/(2*1);
K2=((lb^2)*(2*lb+1.5*lm))/(3*b*(2*lb+lm-le));
bm=2*zeta*wn*m*K1;
Rb=K1*K2*bm
C1=(E_pzt)/(K1*K2*m);
C2=bm/(K1*m);
C3=(E_pzt*d31)/(K1*K2*m*thick_pzt);
C4=1/K2;
C5=(thick_pzt*d31*E_pzt)/(Epiezo);

% Cantilever Beam Analysis Using Constant Acceleration Shape Functions
% Cross Section Properties, Assume Bi-Morph Beam With Equal Thickness Piezo
% Layers

t1=0.134e-3; %m, piezo thickness
t2=0.129e-3; %m, structural thickness
w=3.2e-3; %m, width of beam
lm=3.26e-3; %m, length of proof mass

% Material Properties

E1=11e10; %N/m^2, Youngs mod for structural layer
E2=62e9; %N/m^2, Youngs mod for piezo layers
rho_p=7800; %kg/m^3, piezo density
rho_s=8800; %kg/m^3, structural density
M=0.0005894; %kg, proof mass at free end

% Beam Geometry, Concentrated Load At Free End

```

```

lp=25.35e-3-3.26e-3;      %m, length with piezo (section 1)
lt=25.35e-3;             %m, total length

lb=lt-lp;                %m, length with out piezo (section 2)

%Average Sectional Properties, EI_ave=K
K_1=E1*(1/12*w*t2^3+1/6*E2/E1*w*t1^3+2*t1*E2/E1*w*(t2/2+t1/2)^2);
      %N-m^2, section 1 sectional stiffness
K_2=E1*(1/12*w*t2^3);
      %N-m^2, section 2 sectional stiffness
rho_1=rho_p*t1*w+rho_s*t2*w;
      %kg/m, section 1 linear density
rho_2=rho_s*t2*w;
      %kg/m, section 2 linear density

%Loading Cases Given Constant Acceleration
a=9.81*1;                %m/s^2, constant acceleration
w_p=rho_p*t1*w*a;        %N/m, distributed piezo mass load (case 1)
w_b=rho_s*t2*w*a;        %N/m, distributed struct mass load (case 2)
F=M*a;                   %N, concentrated load at free end

syms x

%Case 1, y1 domain 0<x<lp, y2 domain lp<x<lt
y11=-w_p/2/K_1*(1/2*lp^2*x^2+1/12*x^4-1/3*lp*x^3);
y21=-w_p*lp^4/K_1/8-w_p*lp^3/6/K_1*(x-lp);

%Case 2, y1 domain 0<x<lp, y2 domain lp<x<lt
C12=w_b/2*(lt^2*lp+1/3*lp^3-lt*lp^2)*(1-K_2/K_1);
C22=w_b/2*(1/2*lt^2*lp^2+1/12*lp^4-1/3*lp^3*lt)*(1-K_2/K_1)-C12*lp;
y12=-w_b/2/K_1*(1/2*lt^2*x^2+1/12*x^4-1/3*lt*x^3);
y22=-w_b/2/K_2*(1/2*lt^2*x^2+1/12*x^4-1/3*lt*x^3)+C12/K_2*x+C22/K_2;

%Case 3, y1 domain 0<x<lp, y2 domain lp<x<lt
C13=F*(-1/2*lp^2+(lt-lb/2)*lp)*(1-K_2/K_1);
C23=F*(-1/6*lp^3+1/2*(lt-lb/2)*lp^2)*(1-K_2/K_1)-C13*lp;
y13=-F/K_1*(-1/6*x^3+1/2*(lt-lb/2)*x^2);
y23=-F/K_2*(-1/6*x^3+1/2*(lt-lb/2)*x^2)+C13/K_2*x+C23/K_2;

%Apply Superposition To Get Total Displacement Function
y1=vpa(y11+y12+y13,5)
y2=vpa(y21+y22+y23,5)
y1d=vpa(y11+y12+y13,5)+a/(1.5*2*pi)^2*0
y2d=vpa(y21+y22+y23,5)+a/(1.5*2*pi)^2*0

subplot(2,1,1);
ezplot(y1d,[0,lp]);
subplot(2,1,2);
ezplot(y2d,[lp,lt]);

%Moment Functions For Strain (Potential) Energy Calculation

```

```

M1=1/2*w_p*lp^2+1/2*w_p*x^2-lp*w_p*x+1/2*w_b*(lt^2+x^2-2*lt*x)+F*(lt-x);
M2=1/2*w_b*(lt^2+x^2-2*lt*x)+F*(lt-x);
%subplot(2,1,1);
%ezplot(M1,[0,lp]);
%subplot(2,1,2);
%ezplot(M2,[lp,lt]);

%Maximum Potential Energy
U_p=int(M1^2/2/K_1,x,0,lp)+int(M2^2/2/K_2,x,lp,lt);

%Maximum Kinetic Energy/omega^2
U_k=int(rho_1*y1d^2/2,x,0,lp)+int(rho_2*y2d^2/2,x,lp,lt)+int(M/lm*y2d^2/2,x,lt-lm,lt);

%Lumped Spring Constant
K=vpa(abs(U_p^2/(int(y2,x,lt-lm,lt)/lm)^2),5) %N/m

%Natural Frequency
omega=(U_p/U_k)^.5; %rad/s
f=vpa(omega/2/pi,5) %Hz

%Lumped Mass
Mass=vpa(K/omega^2,5) %kg

% PZT Bimorph (parallel config) State Space Model

clear all
format compact

% Inputs
Temp=40; %C
L=25.35e-3; %m
lm=3.26e-3; %m
wm=3.05e-3; %m
hm=3.07e-3; %m
tp=0.134e-3; %m
tsh=0.129e-3; %m
wp=3.2e-3; %m
kpeiz=0.44;
rhosh=8800; %kg/m^3
rhop=7800; %kg/m^3
rhom=1.93e4; %kg/m^3
l=L-lm/2;
tand=0.05; %loss tan

% Given constants
%d31=3.20e-10; %m/V
%e=3.36e-8; %F/m
Ep=6.2e10*(1-kpeiz^2); %N/m^2
Esh=1.1e11; %N/m^2

% Temp Dependent
d31=2.39e-10+8.24e-13*Temp-2.67e-15*Temp^2+3.59e-17*Temp^3+3.48e-19*Temp^4;
e=(2292.1+16.775*Temp+0.065556*Temp^2+7.41E-5*Temp^3+8.47e-20*Temp^4)*8.854e-12;
Ep=Ep-(20-Temp)/160*Ep/4

```

```

Esh=Esh-(20-Temp)/160*Ep*104/110

%Tip Mass
M=rhom*Im*wm*hm;

%Sectional Stiffness
I=1/12*wp*tsh^3+1/6*Ep/Esh*wp*tp^3+1/2*tp*Ep/Esh*wp*(tp+tsh)^2;
EI=Esh*I;

%Beam Mass
Mb=L*wp*(2*tp*rhop+tsh*rhosh);

%Total Mass
Mt=33/140*Mb+M;

%Stiffness
k=3*EI/l^3;

%Natural Frequency
f=sqrt(k/Mt)/2/pi

%alpha (coupling coef)
alphap=3*wp*Ep*d31/2/l*(tsh+tp);
Cpp=2*e*wp*L/tp*(1-tand*1i);

%system coef
A1p=-1/Mt;
A2p=-k/Mt;
A3p=alphap/Mt;
A4p=-alphap/Cpp;
A5p=-1/Cpp;

c=.01;
A1=c*A1p;
A2=A2p;
A3=A3p;
A4=A4p;
A5=A5p;

R_par=10e6;

R1=10e3;
R2=20e3;
R3=30e3;
R4=40e3;
R5=50e3;
R6=60e3;
R7=70e3;
R8=80e3;
R9=90e3;
R10=100e3;

```

```
R=[R1 R2 R3 R4 R5 R6 R7 R8 R9 R10];
```

```
Aa=[0 1 0;A2 A1 A3; 0 A4 A5/R1/R_par*(R1+R_par)];  
Ab=[0 1 0;A2 A1 A3; 0 A4 A5/R2/R_par*(R2+R_par)];  
Ac=[0 1 0;A2 A1 A3; 0 A4 A5/R3/R_par*(R3+R_par)];  
Ad=[0 1 0;A2 A1 A3; 0 A4 A5/R4/R_par*(R4+R_par)];  
Ae=[0 1 0;A2 A1 A3; 0 A4 A5/R5/R_par*(R5+R_par)];  
Af=[0 1 0;A2 A1 A3; 0 A4 A5/R6/R_par*(R6+R_par)];  
Ag=[0 1 0;A2 A1 A3; 0 A4 A5/R7/R_par*(R7+R_par)];  
Ah=[0 1 0;A2 A1 A3; 0 A4 A5/R8/R_par*(R8+R_par)];  
Ai=[0 1 0;A2 A1 A3; 0 A4 A5/R9/R_par*(R9+R_par)];  
Aj=[0 1 0;A2 A1 A3; 0 A4 A5/R10/R_par*(R10+R_par)];
```

```
B=[0 -9.81 0];
```

```
C=[0 0 1];
```

```
D=0;
```

```
sys1=ss(Aa,B,C,D);
```

```
sys2=ss(Ab,B,C,D);
```

```
sys3=ss(Ac,B,C,D);
```

```
sys4=ss(Ad,B,C,D);
```

```
sys5=ss(Ae,B,C,D);
```

```
sys6=ss(Af,B,C,D);
```

```
sys7=ss(Ag,B,C,D);
```

```
sys8=ss(Ah,B,C,D);
```

```
sys9=ss(Ai,B,C,D);
```

```
sys10=ss(Aj,B,C,D);
```

```
w=60*2*pi:.5:120*2*pi;
```

```
[mag1 phase1 w1]=bode(sys1,w);
```

```
mag1=mag1(:);
```

```
[mag2 phase2 w2]=bode(sys2,w);
```

```
mag2=mag2(:);
```

```
[mag3 phase3 w3]=bode(sys3,w);
```

```
mag3=mag3(:);
```

```
[mag4 phase4 w4]=bode(sys4,w);
```

```
mag4=mag4(:);
```

```
[mag5 phase5 w5]=bode(sys5,w);
```

```
mag5=mag5(:);
```

```
[mag6 phase6 w6]=bode(sys6,w);
```

```
mag6=mag6(:);
```

```
[mag7 phase7 w7]=bode(sys7,w);
```

```
mag7=mag7(:);
```

```
[mag8 phase8 w8]=bode(sys8,w);
```

```
mag8=mag8(:);
```

```
[mag9 phase9 w9]=bode(sys9,w);
```

```
mag9=mag9(:);
```

```
[mag10 phase10 w10]=bode(sys10,w);
```

```
mag10=mag10(:);
```

```
mag=[mag1 mag2 mag3 mag4 mag5 mag6 mag7 mag8 mag9 mag10];
```

```
figure(1)
```

```

plot(w1/2/pi,mag1,w2/2/pi,mag2,w3/2/pi,mag3,w4/2/pi,mag4,w5/2/pi,mag5,w6/2/pi,mag6,w7/2/pi,
mag7,w8/2/pi,mag8,w9/2/pi,mag9,w10/2/pi,mag10)
xlabel('Hz')
ylabel('Voltage')
title('Voltage vs Frequency')
legend('20 kOhm','40 kOhm','60 kOhm','80 kOhm','100 kOhm','120 kOhm','140 kOhm','160
kOhm','180 kOhm','2 GOhm')

```

```

figure(2)
plot(w1/2/pi,mag1.^2/2/R1*1000000,w2/2/pi,mag2.^2/2/R2*1000000,w3/2/pi,mag3.^2/2/R3*10000
00,w4/2/pi,mag4.^2/2/R4*1000000,w5/2/pi,mag5.^2/2/R5*1000000,w6/2/pi,mag6.^2/2/R6*100000
0,w7/2/pi,mag7.^2/2/R7*1000000,w8/2/pi,mag8.^2/2/R8*1000000,w9/2/pi,mag9.^2/2/R9*1000000
,w10/2/pi,mag10.^2/2/R10*1000000)
xlabel('Hz')
ylabel('Power (uW)')
title('Power vs Frequency')
legend('20 kOhm','40 kOhm','60 kOhm','80 kOhm','100 kOhm','120 kOhm','140 kOhm','160
kOhm','180 kOhm','2 GOhm')

```

```

figure(3)
pzmap(sys1,sys2,sys3,sys4,sys5,sys6,sys7,sys8,sys9,sys10)
%legend('10 kOhm','10 kOhm','20 kOhm','20 kOhm','30 kOhm','30 kOhm','40 kOhm','40
kOhm','50 kOhm','50 kOhm','60 kOhm','60 kOhm','70 kOhm','70 kOhm','80 kOhm','80 kOhm','90
kOhm','90 kOhm','100 kOhm','100 kOhm')

```

```

num=300:10:400
mag_r=[mag1.^2/2/R1*1000000 mag2.^2/2/R2*1000000 mag3.^2/2/R3*1000000
mag4.^2/2/R4*1000000 mag5.^2/2/R5*1000000 mag6.^2/2/R6*1000000 mag7.^2/2/R7*1000000
mag8.^2/2/R8*1000000 mag9.^2/2/R9*1000000 mag10.^2/2/R10*1000000];
w(num)/2/pi

```

```

figure(4)
plot(R,mag_r(num,:))
xlabel('Resistance (Ohm)')
ylabel('Power (uW)')
title('Power vs Resistance')
legend('83.7937 Hz','84.5894 Hz','85.3852 Hz','86.1810 Hz','86.9768 Hz','87.7725 Hz','88.5683
Hz','89.3641 Hz','90.1599 Hz','90.9556 Hz','91.7514 Hz')

```

```
%Curve Fitting for PZT-5H
```

```
clear all
format long
```

```
%d31 data
T=[-150 -100 -50 0 50 100]'; %C
d31=[110 133.25 180.75 247.5 276.25 366.5]*10^-12; %m/V
e=[1000 1200 1600 2300 3300 4700]';
rho=[10 9 7.5 5 3 3]*10^8;
dT=T-25; %C
```

```
%Approximate linear fit for -150<T<100 C
Alin=[ones(length(dT),1) dT];
```



```

xd31=(Alin*Alin)^-1*Alin*d31
d311=xd31(1)+xd31(2)*dT;

xe=(Alin*Alin)^-1*Alin*e
e1=xe(1)+xe(2)*dT;

xrho=(Alin*Alin)^-1*Alin*rho
rho1=xrho(1)+xrho(2)*dT;

%Approximate quad fit for -150<T<100 C
Aquad=[ones(length(dT),1) dT dT.^2];

xd31q=(Aquad*Aquad)^-1*Aquad*d31
d312=xd31q(1)+xd31q(2)*dT+xd31q(3)*dT.^2;

xeq=(Aquad*Aquad)^-1*Aquad*e
e2=xeq(1)+xeq(2)*dT+xeq(3)*dT.^2;

xrhoq=(Aquad*Aquad)^-1*Aquad*rho
rho2=xrhoq(1)+xrhoq(2)*dT+xrhoq(3)*dT.^2;

%Approximate cubic fit for -150<T<100 C
Acube=[ones(length(dT),1) dT dT.^2 dT.^3];

xd31c=(Acube*Acube)^-1*Acube*d31
d313=xd31c(1)+xd31c(2)*dT+xd31c(3)*dT.^2+xd31c(4)*dT.^3;

xec=(Acube*Acube)^-1*Acube*e
e3=xec(1)+xec(2)*dT+xec(3)*dT.^2+xec(4)*dT.^3;

xrhoc=(Acube*Acube)^-1*Acube*rho
rho3=xrhoc(1)+xrhoc(2)*dT+xrhoc(3)*dT.^2+xrhoc(4)*dT.^3;

%Approximate 4th order fit for -150<T<100 C
A4=[ones(length(dT),1) dT dT.^2 dT.^3 dT.^4];

xd314=(A4*A4)^-1*A4*d31
d314=xd314(1)+xd314(2)*dT+xd314(3)*dT.^2+xd314(4)*dT.^3+xd314(5)*dT.^4;
figure(1)
plot(dT,d31,'x',dT,d311,dT,d312,dT,d313,dT,d314)
legend('data','1st','2nd','3rd','4th','location','Best')
title('d31 vs Temperature Variation')
xlabel('Temp Change (C)')
ylabel('d31 (m/V)')

xe4=(A4*A4)^-1*A4*e
e4=xe4(1)+xe4(2)*dT+xe4(3)*dT.^2+xe4(4)*dT.^3+xe4(5)*dT.^4;
figure(2)
plot(dT,e,'x',dT,e1,dT,e2,dT,e3,dT,e4)
legend('data','1st','2nd','3rd','4th','location','Best')
title('Dielectric Constant vs Temperature Variation')
xlabel('Temp Change (C)')
ylabel('Dielectric Constant')

```

```

rho4=(A4*A4)^-1*A4*rho
rho4=xrho4(1)+xrho4(2)*dT+xrho4(3)*dT.^2+xrho4(4)*dT.^3+xrho4(5)*dT.^4;
figure(3)
plot(dT,rho,'x',dT,rho1,dT,rho2,dT,rho3,dT,rho4)
legend('data','1st','2nd','3rd','4th','location','Best')
title('Resistivity vs Temperature Variation')
xlabel('Temp Change (C)')
ylabel('Resistivity (ohm-cm)')

% Electrical Equivalent circuit model
clc;
clear all;
Y=3*9.81;
E_metal= 11e10; %Pa Young's modulus
E_pzt=62e9; %Pa Young's modulus
ns=E_pzt/E_metal; % Ration of elastic constants
np=2; % Number of PZT layer
m=0.0005894;% in Kg
lb=21.97e-3; %m beam length
le=21.97e-3; %m length of electrode
lm=3.03e-3; %m length of proof mass
width=3.22e-3; %m beam width
thick_pzt=0.134e-3;%m thickness
thick_metal=0.129e-3;%m thickness
b=(thick_pzt+thick_metal)/2;
%I =
(2*width*(thick_pzt)^3/12)+(2*width*thick_pzt*((thick_metal+thick_pzt)/
2)^2)+(E_pzt*width*(thick_metal)^3/(E_metal*12)); %m^4 M. A. of inertia
I=
(((width*np*thick_pzt^3)/12)+width*np*thick_pzt*b^2)+(ns*width*thick_metal^3)/12;
zeta=0.02; %Damping ratio
wn=596; % Resonant frequency of beam
K31=0.44;
Epiezo=3800*8.85e-12; % Dielectric constant
d31=-3.20e-10; % m/volt piezoelectric voltage constant
K1=(b*(2*lb+lm-le))/(2*I);
K2=((lb^2)*(2*lb+1.5*lm))/(3*b*(2*lb+lm-le));
bm=2*zeta*wn*m*K1;
Rb=K1*K2*bm;
bb=(3*b*(2*lb+lm-le))/((lb^2)*(2*lb+1.5*lm)); %b*
Cp=(np*Epiezo*width*le)/(thick_pzt);
C1=(E_pzt)/(K1*K2*m);
C2=bm/(K1*m);
C3=(E_pzt*d31)/(K1*K2*m*thick_pzt);
C4=1/K2;
C5=(thick_pzt*d31*E_pzt)/(Epiezo);
Cb=(Epiezo*width*le)/(2*thick_pzt);
% R=0:100:1000000;
% for i=1:10001
%
Pgen(i,:)=(1/(2*wn*wn))*(R(i)*Cb*Cb*((2*E_pzt*d31*thick_pzt)/(K2*Epiezo

```

```

)) ^2*Y^2)/((4*zeta^2+K31^4)*(R(i)*Cb*wn)^2+4*zeta*K31^2*R(i)*Cb*wn+4*ze
ta^2);
% end
Ropt=(1/(wn*Cp))*(2*zeta/(sqrt(4*zeta^2+K31^4)));
R=75000
w=0:1:1000;
for i=1:1001
Power(i,:)=100000*((w(i)*E_pzt*d31*thick_pzt*bb*Y/Epiezo)^2)/(((1/R*Cp
)*wn^2 - ((1/R*Cp)+2*zeta*wn)*(w(i))^2)^2 +
(w(i))^2*(wn^2*(1+K31^2)+((2*zeta*wn)/(R*Cp))-(w(i))^2)^2)*R);
Voltage(i,:)=sqrt(R*Power(i,)/1000000);
end

% Energy model
clc;
clear all;
%function Voltage=Volt(t)
%function Voltage=Volt(w)
Y=9.81; % input acceleration
rho_metal = 8600; %kg/m^3 density
rho_pzt= 7750;%kg/m^3 density
E_metal= 11e10; %Pa Young's modulus
E_pzt=62e9; %Pa Young's modulus
Lbeam = 25.60e-3; %m length
width=3.22e-3; %m beam width
thick_pzt=0.134e-3;%m thickness
thick_metal=0.132e-3;%m thickness
thickbeam = 0.4e-3; %m thickness
Lm = 22.34e-3; % defelection point
K31=0.32;
d31 = 1.9e-10; %m/volt dielectric constant
Mass_on_end=0.0005894;% in Kg
Mass_beam=rho_metal*width*Lbeam*thick_metal +
2*rho_pzt*width*Lbeam*thick_pzt;
A=(2*(3*thick_metal^2*thick_pzt + 6*thick_metal*thick_pzt^2
+4*thick_pzt^3)/E_metal)+(thick_metal^3)/E_pzt;
Epiezo=1800*8.85e-12; % Dielectric constant
X11=12*E_metal*thick_pzt^2*thick_metal+8*E_metal*thick_pzt^3+6*E_metal*
thick_pzt*thick_metal^2+E_pzt*thick_metal^3;
% piezo properties
zeta = .07;
Mtotal=(33/140)*Mass_beam + Mass_on_end;
K=(A*width*E_metal*E_pzt)/(4*Lbeam^3);
wn=sqrt(K/Mtotal);
fn = wn/(2*pi);
w=wn;
Vgen=(6*d31*E_metal*thick_pzt*(thick_pzt+thick_metal)*Lm)/(Epiezo*width
*X11*(1+((6*E_metal*thick_pzt*(thick_pzt+thick_metal)^2)/(X11)-
1)*K31^2));
qgen=(-3*(d31*E_metal*(thick_metal+thick_pzt)*Lm^2)/X11);
R=0;
%
Pconstant=(w^2*width^2*thick_metal^2*d31^2*R)/(4*(1+width*Lm*Epiezo*(w*
R/thick_pzt))^2);
%Cb=((Lm*width)/(2*thick_pzt))*(Epiezo)*(1-(A-
6*thick_pzt*(thick_metal+thick_pzt)^2*K31^2)/(A));
% R=10;

```

```

% pgen=1/(2*R*(1+(1/(wn*Cb*R))^2));
Cfree=(Epiezo*width*Lm/(2*thick_pzt))*(1+((6*E_metal*thick_pzt*(thick_p
zt+thick_metal)^2-X11)*K31^2)/(X11));
Ropt2=1/(w*Cfree);
pgen=1/(2*R*(1+(1/(wn*Cfree*R))^2));

```

